Diffraction and Localization in Quantum Billiards

A thesis presented
by

Natasha Lepore

to
The Department of Physics
in partial fulfillment of the requirements
for the degree of
Doctor of Philosophy
in the subject of

Physics

Harvard University
Cambridge, Massachusetts
May 2003

Thesis advisor Author

Professor Eric J. Heller **Natasha Lepore**

Diffraction and Localization in Quantum Billiards

Abstract

This thesis is about quantum chaos in two-dimensional billiards. In the first part, we devise new methods for finding the eigenstates of these systems. We unify the two currently known boundary methods, the plane wave decomposition method (PWDM) and the boundary integral method (BIM) into a single framework. A third boundary method, the gauge freedom method (GFM) is derived from the gauge freedom of the free-space Green function. Non-convex, multiply-connected shapes are studied using improved bases for the PWDM. Zeroth-order Neumann functions are placed on a line around the boundary. These dramatically increases the number of eigenstates as compared those found using bases composed solely of plane waves. Finally, we compare the standard PWDM for two triangular shapes, one with concave walls, and the other with convex ones. The PWDM is much more successful in the former case. The second part of this thesis is about localization effects in quantum billiards. Boundary effects are investigated. It is found that for rational wedges, as well as for semi-infinite corridors, the two-point correlation functions are given by sums of zeroth-order Bessel functions. The theoretical correlation functions are verified numerically for both of these cases. Finally, we investigate localization effects on the pseudosphere, a strongly chaotic system. Several localization effects are found to be present. We investigate the focusing effects of the boundaries. Furthermore, the longstanding problem of scarring on the pseudosphere is investigated. Contrary to what was previously believed [3], we find scarring to be present in our billiards. Our numerics were done with triangles with geodesic sides, as well as with generic non-geodesic triangles.

Contents

Citations to Previously Published Work

Chapter 3 has appeared in the following paper:

> "Consolidating Boundary Methods for Finding the Eigenstates of Billiards", D. Cohen, N. Lepore and E. J. Heller, `nlin.CD/0108014`;

Chapter 5 has appeared in the following paper:

> "Quantum Billiards and Constrained Random Wave Correlations", W.E. Bies, N. Lepore and E. J. Heller, J. Phys A **36**, 1605 (2003);

Electronic preprints (shown in `typewriter font`) are available on the Internet at the following URL:

> `http://arXiv.org`

Acknowledgments

My thesis years were the most intense learning years of my life, and many people generously contributed to this process. First and foremost, I would like to thank my advisor, Professor Eric Heller, for sharing his wealth of ideas and his enthusiasm for physics, and for the wonderful work environment that he created in our group. I am also grateful to the members of my thesis committee, Professor Kaxiras, and Professor Westervelt for all their help and advice.

Our group is special among theory groups for the amount of collaboration among graduate students and postdocs. I have had the chance to work closely with several postdoctoral students through the last few years. When I first joined the group, Lev Kaplan spent countless hours getting me up to date on the basics of quantum chaos. After Lev‘s departure, I had the great fortune to work with Michael Haggerty. I can never thank him enough for (literally) forcing me to ask him for help at a time when I most needed it, and for being an incredibly generous, patient and perceptive mentor thereafter. Once Michael left, I started a project with Doron Cohen. I would like to thank him for patiently guiding me through my first graduate school paper. Alex Barnett taught me the ins and outs of boundary methods. In the last year, I wrote two papers in collaboration with Bill Bies. I wish we had started to work together much earlier... collaborating with him has made it fun to do all this work! Several graduate students in the group have also been of tremendous help. I will be sad to leave the office I have shared with my wonderful officemates Areez Mody and Jiri Vanicek. Areez has been a great friend, in addition to being able to find the answer to every physics question I had (though he always initially claimed not to know). And Jiri has been my conference travel buddy throughout my time in the group. I have also had many discussions with Diego Vaz Bevilaqua, Jay Vaishnav, Robert Ellis, Troy Van Voorhis, Jessie Herch, Sheng Li and Allison Kalben. Finally, this group would not be what it is without Carol Davis and and Judy Morrison (without whom we would never be able to find Rick!).

Of course, none of this would have been possible without the help of the people whose support got me into Harvard in the first place, Dave London, Maryse Lassonde, Lucie Lamontagne and Helene Nadeau. Thanks to all of you for believing that I could do this!

Now that I have thanked the people who have helped with my thesis, I would like to acknowledge those who have allowed me to relax and enjoy the time spent working on it and away from it... First among these are my parents, Elizabeth Wentser and Franco Lepore for their constant support and sense of humor, which I sometimes demanded of them at 4:00AM! Maui, my baby cat, who gave me lots of unconditional love, cute stares, and scars throughout the last two years of my thesis. The rest of my family also contributed to making this possible. Especially my brother Alexandre Lepore, Isabelle Gagnon, Suzanne Lapointe, Georges Wentser, Rita and Fernand Lemoine and my gradparents Sonia Koniaiev as well as Carmela DiFrancesco and Alfredo Lepore, both of whom unfortunately did not live to see the completion of this work.

I strongly recommend martial arts as a relief against computer crashes, programming bugs, and stalled calculations. I am most grateful to Kanai sensei and all the instructors and students at New England Aikikai for providing with a place where I could forget about my thesis, and come back to it very bruised, but much happier!

I would especially like to acknowledge my great friend Lesley Budell (my diplomacy advisor) and Keith Roberts, who helped me escape economic doom. Also, my other aikido buddies: Octavian Bocca, Holly Bocca, Sarah Miley, Andres Bermudez, Sioux Hall, Zaf Haneef, Dolita Cathart, John Black and Mary Fuller, and Sayuri Ishigame. But most of all, Andre Brown, my beautiful coach. Thank you for being so genuinely kind and sweet.

It might come as a surprise, but there was a life before Harvard, too. Luckily, some friends from days past came along for the ride. My childhood friends Julie St-Hilaire, Hue Chau Nguyen, Geraldine Leong Son, Jean Fallon, Annette Renaud and Annie St-Amour. Most especially, Brian Thorndyke, one of the most influential people in my life. Thank you for truly understanding me.

Back at Harvard, two important players for my (support system) team deserve extra points: Frank Mcnamara and Bob Collins. You kept me in the game.

Finally, special thanks to my teammates, who rode the Harvard roller coaster with me. They were there. They understood. And they helped. Rosalba Perna (my companion in arms), Ue-Li Pen (my first mentor at Harvard), Luca Marinelli and Carter Hall (my department buddies), Jenny Liu, Katherine Chen, Manda Jost (in particular for pushing me to finish this!), Alexandra Vega (my great friend who made 380 Washington Street such a fun -and organized- place to live), Marthe Moldes, Ofer Shapira and Pedzi Makumbe.

I am sure you‘ll be relieved to know that I am not planning to do another Ph.D! (At least anytime soon...) :)

To my parents

Chapter 1

Introduction

This thesis concerns itself with the study of the quantum mechanics of classically chaotic systems. Classical chaos is characterized by the sensitivity of the system under observation to initial conditions. Quantum mechanically, due to Heisenberg's uncertainty principle, initial conditions in phase space are known only up to an area of order $\hbar$. Thus, chaos manifests itself very differently in quantum systems, as compared to their classical equivalents.

There exist two main agendas to this field. Firstly, as the energy increases, the quantum-mechanical solutions should be consistent with the classical ones. Thus, one would like to be able to relate the wavefunctions of a system to the associated classical trajectories. Semi-classically, the wavefunction is given by a sum over classical orbits [23]

$$\Psi = \sum_n \sqrt{P_n(\vec{x})} \exp(i\phi_n(\vec{x})) \tag{1.1}$$

where the sum is taken over all the paths n from a fixed initial position to $\vec{x}$, P_n is the classical probability of reaching $\vec{x}$ along the nth path, and ϕ_n is the classical action at $\vec{x}$ along that path. For instance, for a free particle surrounded by an infinite wall– a billiard system – the classical action is locally given by $\phi_n = \vec{p_n} \cdot \vec{x} - \phi_0$. The momentum $\vec{p_n}$ is constant along each trajectory, and its norm fixed and independent of the path. The phase ϕ_0 is made out of two components. The first one is a continuously increasing phase from the starting point of the trajectory up to its last intersection with the boundary. To this number should be added a discrete phase, $\pi\nu/2$, where ν is the Maslov index, which is determined by counting the number of conjugate points and twice the number of bounces. Thus,

$$\Psi = \sum_n \sqrt{P_n(\vec{x})} \exp(i\vec{p_n} \cdot \vec{x} - \phi_0) \tag{1.2}$$

For a chaotic system, the classical paths arrive at $\vec{x}$ from every direction and with every phase. As a result, Berry [6] conjectured that the wavefunction should resemble a random superposition of plane waves for these systems.

The second part of the quantum chaotic agenda consists of finding the purely quantum-mechanical manifestations of chaos. In many respects, Berry's conjecture is a successful description of chaotic wavefunctions in billiards. However, this description is not yet complete, since it does not contain any specific information about the particular system under study.

Several departures from Berry's picture have been found to date. One particularly striking example of such deviations is exhibited by the scarring phenomenon, which was discovered by Heller [21]. Scars consist of statistical enhancements of the amplitude of wavefunctions around unstable periodic orbits.

The first half of this thesis is concerned with improving current methods of finding the eigenstates of billiards, especially at higher energies where current methods fail, as I will explain later in this section. In the second half, deviations from the random plane wave background on these eigenstates are investigated.

1.1 The billiard problem

The free particle in a two-dimensional box is one of the most studied systems in quantum chaos. Varying the shape of the box will change the dynamics of the particle, making them anywhere from fully integrable for example for circular boundaries, to completely chaotic as in the case of the stadium billiard (see Figure 6.5). The calculation amounts to solving the Helmholtz equation,

$$(\nabla^2 + k_n^2)\Psi_n(\vec{x}) = 0 \tag{1.3}$$

with a wavefunction $\Psi_n(\vec{x})$ that vanishes on a prescribed boundary, i.e. the wall.

There are several good reasons to study billiards. Primarily, they are ideal systems in which to study quantum chaos, since they are the simplest systems in which it is possible to do so, but yet they still exhibit many of the essential features of more complex chaotic systems [46]. Furthermore, most quantum chaos experiments have been done on systems that emulate the properties of quantum billiards. The preponderance of billiard experiments is only partially due to the interest that theorists have shown in these systems. Most of the currently realizable quantum chaotic systems are designed as walls between which particles are allowed to move freely. Examples of these are quantum corrals, waveguides and 2-dimensional electron gases confined by electrodes. The most common experimental tool in this field is the microwave billiard. These systems make use of the analogy between quantum wavefunctions and the electric field of transverse magnetic modes in the cavity, both of which satisfy the Helmholtz equation with Dirichlet boundary conditions (for low enough frequencies of the photons). See e.g. [46] for a review of these and other billiard experiments.

Another reason to study these systems is that as energies rise, the classical trajectories take on meaning, thus allowing a study the correspondence between the classical and quantum behaviors.

Billiard shapes whose dynamics are integrable classically have analytic solutions, for instance plane waves for the square, and Bessel functions for the circle. On the other hand, it is empirically known that shapes that have chaotic or mixed phase space need to be solved numerically, although no rigorous proof of this has been found.

In spite of the apparent simplicity of the problem, it is a non-trivial task to compute of the eigenstates of billiards of chaotic and mixed phase spaces, for all but a few shapes. For low enough energies, there exists a straightforward strategy to solve for non-integrable shapes. A basis is selected such that the functions it contains satisfy the Dirichlet boundary conditions, though not necessarily the Helmholtz equation. For instance, one may choose narrow Gaussians placed on a grid inside of the billiard. The Laplacian operator can then be diagonalized in in this basis. However, it is clear that this method requires at least as many basis functions as the quantum number n of the state that is being solved for. According to Weyl‘s law,

$$N = Ak^2/4\pi \tag{1.4}$$

the number of states up to a given k scales as k^2 in two dimensions. Here A is the area of the billiard. Thus, this method can only find eigenstates up to some wavenumber

k_{max}.

At higher energies, these methods are computationally prohibitive due to the size of the basis required. The strategies that we will describe in length in chapters 3, 4 circumvent this difficulty by reducing the problem of finding the wavefunction everywhere inside the billiard to that of finding its value on the boundary, thereby changing the dimensionality of the problem from two to one. These boundary methods increase the number of computationally accessible eigenstates. The main results of chapter 3 will be to unify all such methods into a single framework. In the process, a new method of finding eigenstates will be derived which follows the same general philosophy. In chapter 4, we study a non-convex shape which is not easily solved using standard techniques, and compute its eigenstates using an extension of the boundary methods described in chapter 3.

1.2 Localization in Billiards

Beyond Berry‘s conjecture, the structure of chaotic eigenstates takes on various forms. Firstly, it is clear that the wavefunction must satisfy the constraints of the system. Thus, if for instance, a billiard wall is present, the wavefunction can not look random in its vicinity. Berry [8] studied the effect of a straight impermeable wall on superposition of plane waves whose coefficients were random up to satisfying the boundary conditions. The statistics of the nodal lines and points were computed near the wall, and a long-range correction of order $\log k$ was found in the length of the nodal lines as compared to the wall-free case, while the density of nodal points was changed by a long-range term of order $k \log k$. The symmetries of particular billiards further contribute to the non-random characteristics of their eigenfunctions. Such constraints are inherent to the system under study, and remain present as $\hbar \to 0$.

Furthermore, for classical chaotic systems, all of the energy shell is explored, up to the constraints of the system. Thus, on scales large compared to $\hbar$, the wavefunctions of the equivalent quantum system should be spread evenly over all of the accessible phase space. It was shown by Schnirelman [39], Zelditch [51] and Colin de Verdiere [16] (SZCdV) that indeed, in the semiclassical limit, almost all the quantum eigenstates of classically chaotic systems are ergodic when smoothed over macroscopic patches in phase space.

On the other hand, the ergodicity theorem of SZCdV does not apply to areas which are large compared to $\hbar$, but still vanishing as $\hbar \to 0$ [27]. Thus, localization may be present on those scales.

In fact, it was found by O'connor *et al.* [36] that random superpositions of plane waves themselves exhibit a network of overdense linear structures, as well as quasi-circular underdense regions. The overdense lines were explained by considering the overlap of a small Gaussian wavepacket with the wavefunction. The later remains constant as the wavepacket evolves. Thus, if the initial overlap is large, it should remain so after a short time interval. As a consequence, the intensity of the eigenstate should exceed that of the background along the direction of propagation of such a wavepacket. A similar argument was used to understand the low density areas. A narrow wavepacket of momentum $\vec{k}$ may be placed at the center of the underdense region. All such wavepackets have low overlap with the eigenstate. As the wavepacket travels along $\vec{k}$, the overlap should remain small. As a result, the nodal lines of the eigenstate are required to be almost perpendicular to those of all such wavepackets, that is, radially outward.

An more striking departure from microscopic ergodicity is seen in the appearance of scars, which are defined as statistically significant enhancement of the wavefunction density along unstable periodic orbits as compared to the value expected from that expected from Berry‘s conjecture. Scars were first observed in the stadium billiard by Heller [21], who also provided the first explanation for their existence. Scars are particularly interesting in that they are a purely quantum mechanical consequence of the dynamics, and thus have no classical equivalent. Furthermore, in the semi-classical limit, scarring is statistically the largest deviation from microscopic ergodicity for chaotic eigenstates [25]. Scars were first observed experimentally in Sinai shaped microwave cavities by Sridhar and his coworkers (see [43], [44] [38]), and in stadium shaped ones by Stein and Stockmann [45].

The second part of this thesis consists of investigating these various localization effects in chaotic billiards. Firstly, we study the effect of the boundary on the wavefunction, and show that, within that constraint, the wavefunction is as chaotic as can be. For a random superposition of plane waves, the two-point correlation function is a Bessel function. On the other hand, for the wedge and the infinite corridor which we studied, the two-point correlation function is given by a sum of Bessel functions, which includes all the contributions from mirror images of the point under investigation at the various boundaries.

Secondly, we study boundary-induced localization and scarring on the pseudosphere, a system exhibiting hard chaos. Firstly, we look at the focusing effects of adding a boundary. It is shown that the boundary curvature may be chosen to counteract the defocusing effect of the background curvature. We also demonstrate the presence of scarring for billiards with chaotic dynamics on the pseudosphere.

Chapter 2

Numerical methods for billiard eigenstates

In chapters 3 and 4, I describe various ways of improving traditional numerical methods of finding the eigenstates of billiards. Here I review the two main current techniques and describe their strengths and limitations. A short overview of the following two chapters is given at the end of this section.

The two most widely used numerical methods to solve the billiard problem are the boundary integral method (BIM) and the (PWDM). Both of them follow the same general philosophy. That is, both involve using special basis sets which are solutions of Helmholtz equation inside the billiard, for instance, plane waves, or Bessel functions. Each of these functions is a solution of the differential equation everywhere for a fixed k, so that any linear superposition of them remains a solution to the differential equation everywhere. Once a basis is selected that satisfies the right equation, the only remaining issue is that of satisfying the boundary conditions. Thus, the solution is found by fitting the equations on the boundary. The two-dimensional problem has then effectively been reduced to a one dimensional one. The first of these so-called boundary methods, the BIM, flows out of Green's theorem. Secondly, the PWDM uses plane waves as a basis, which are free solutions of of Helmholtz equation inside the billiard. Eigenstates are found by searching for a linear combination of the basis functions which vanishes on the boundary. In the next two sections, I briefly describe the already known numerical techniques, the BIM and the PWDM. A more rigorous derivation will be given in Chapter 3.

2.1 The boundary integral method

The gist of the Boundary Integral Method is that, from the knowledge of the gradient of the wavefunction on the boundary and from Green's theorem, it is possible to find the value of the wavefunction everywhere inside the billiard. The boundary integral equation, which will be derived in Chapter 2, is given by

$$\Psi(\vec{r}) \;=\; \int ds'\hat{n}.G(\vec{r};\vec{r}'(s'))\nabla'\Psi(\vec{r}'(s')) \tag{2.1}$$

For r on the boundary, the left hand side vanishes. This integral equation can then be discretized and solved numerically as a matrix equation, yielding the gradient of the wavefunction on the boundary. Once the charge density is found, the answer is inserted back into Equation 2.1 in order to obtain the solution at any point inside of the billiard.

Intuitively, this equation is easily understood through its electrostatics equivalent. In this analogy, the wavefunction on the boundary is seen as a sum of Green's function sources, with source strength given by the normal derivative of the wavefunction (henceforth called the boundary charge and denoted by $\Phi(s)$). In electrostatics, it is known that forcing the scalar potential to be zero on the boundary induces a boundary charge. From Green's theorem, the induced charge is proportional to the normal component of the electric field. Here the wavefunction acts as the equivalent of the scalar potential. Similarly to the electrostatic case, there exists an induced 'boundary charge', that is in this case proportional to the normal derivative of the wavefunction. The free space Green function is given by

$$G(\vec{r},\vec{r'}) = Y_0(k|\vec{r}-\vec{r'}|) + C(\vec{r},\vec{r'}) \tag{2.2}$$

where C is any solution of the homogeneous equation. This term will be discussed in detail in Chapter 3. This Green function diverges logarithmically at small $|\vec{r}-\vec{r'}|$ and thus for the diagonal elements of the BIM equation. As a result, the BIM equation is hard to solve in its simplest form.

2.2 The plane wave decomposition method

The PWDM is based on the idea that the wavefunction can be written as a linear combination of basis functions that satisfy the Helmholtz equation in free space. Thus, the problem reduces to finding a linear combination that satisfies the boundary conditions. In the original work by Heller [21], and in most applications of the PWDM since, the chosen basis is composed of plane waves. However, it is quite possible that some choices of bases give better approximations to the eigenstates. This consideration is the starting point for the improved numerical methods of Chapter 4.

In order to find the eigenstates, the energy of the basis functions is fixed, while the direction of their wavenumber k, as well as the phases are allowed to vary. In the general case, the phases are chosen to be random, and the directions of k are uniformly distributed. Of course, whenever possible, it is useful to select these parameters in a way that they satisfy the symmetries of the problem. Once a set of plane waves has been selected, basis coefficients are found using singular value decomposition, such that the boundary conditions are satisfied. Since the basis is finite, the boundary conditions will not be satisfied exactly, and the selected coefficients will be the ones which minimize the wavefunction at the wall. Eigenstates are found when the sum of wavefunction intensities at the wall is minimum.

2.3 Strengths and limitations of the methods

The methods described in the preceding sections are the most efficient methods to date to find the eigenstates of billiards. However, as is described below, they are applicable only in certain geometries.

The BIM equations are exact. Thus, as the number of points is increased, the states found through this method should approach the true eigenfunctions of the system at the energy eigenvalues. Li *et al.* [30] showed that the convergence follows a power law in the number b of discretization points per half-wavelengths. For coarse enough grids, the PWDM is much more accurate (see figure 6 of chapter 3) than the BIM. Furthermore, the computation of the singular Neumann basis functions is more computationally taxing than the plane waves of the PWDM, so that the BIM is significantly slower numerically. A problem with exterior chords [30] exists in the case of non-convex shapes, that is, shapes for which the boundary curves inward. These exterior chords occur between points on the boundary which can not be connected with trajectories of less than one bounce inside the billiard. For finite grids, contributions to the Green function from the shortest external trajectories between such points are included in the calculation.

Since the BIM is slow and b large is required, the PWDM is the only computationally accessible method of finding states at large quantum numbers n for general geometries, though other methods have been found in some particular cases (see[5] for a good review of alternative methods).

The eigenstates of shapes with integrable dynamics can easily be resolved with the PWDM although in such cases, an analytical solution may be found instead. Shapes with chaotic and mixed phase space are more complicated. Li and coworkers [30] plotted the PWDM tension versus shape for several billiards with a shape parameters that varied the dynamics from integrable to chaotic. They confirmed that the PWDM tensions indeed depend the amount of chaos in the system.

Furthermore, Vega *et al.* computed the number of states generated by the PWDM in polygonal billiards, and found that a significant fraction of these were missing when the results were compared to expected numbers given by Weyl's law. The fraction of missed states diminished as the number of sides of the polygon increased.

For convex billiards, Gutzkin [20] showed that the eigenstates could be approximated to arbitrary accuracy by superpositions of plane waves $\exp(i\vec{k} \cdot \vec{x})$ where $\vec{k}$ has constant norm and real components. For real $\vec{k}$, it was found (see [5] and figure 3.6) that the convergence plateaus at discretizations of the order of half the wavelength.

After this length, the number of plane waves to be added to improve the accuracy grows exponentially. This problem is easily understood if one takes into account Nyquist theorem, which implies that plane waves that differ by much less than half a wavelength on the boundary give indistinguishable contributions to the wavefunction. Berry [7] showed that plane waves with complex components or evanescent waves can be written as linear combinations of the real plane waves. For numbers of plane waves above those dictated by Nyquist's theorem, part of the superposition will form evanescent waves, although it will do so exponentially slowly. The failure of the PWDM in this case is readily explained by considering the case of a sinusoidal wall. The wavefunction obtained with real plane waves is constrained by $|k_x|, |k_y| < k$. Now let us assume that a fraction of the wall of our billiard is given by $y = \sin(\eta x)$, where $\eta > k$. In order to reproduce the nodal line at the wall, it is necessary to build a wave which oscillates at $k_x = \eta$. In order for k to remain constant, k_y^2 must be negative and k_y imaginary. Thus, for a general billiard, solutions of the form $\exp(ik_r \cdot \vec{r}) \exp(-k_i \cdot \vec{r})$, where $k^2 = k_r^2 - k_i^2$, and k_r and k_i are real are needed in the basis. One remedy to the convergence problem is to include the evanescent solutions directly. Vergini [49] did so as a means to to solve for the eigenstates of the stadium billiard.

For non-convex billiards, the problem is more complicated. Gutzkin [20] demonstrated that the plane wave approximation is bounded below. Thus, in this case, bases consisting only of combinations of plane waves and evanescent waves will fail, and new functions need to be added to the basis.

2.4 Introduction to Chapter 3 and 4

To date, the quantum chaos community has viewed the PWDM and the BIM as being completely independent ways to solve the billiard problem. However, in chapter 3, we show that both of these methods can be viewed under a unified umbrella. In the process of doing this, one is lead to yet a third numerical technique, which we called the Gauge Freedom method. We will show how this new method emerges from the structure of the BIM equations.

In Chapter 4, we use a generalized version of the PWDM to solve for non-convex shapes. We study a smooth boundary with a circular hole at its center. This shape is also problematic, due to the convexity of the inner boundary. The eigenstates are found by adding a row of Neumann functions around the inner boundary. We also compare the PWDM for concave and convex shapes, using triangle-like shapes of these geometries. As expected, the PWDM does a significantly poorer job in the case of the convex shape.

Chapter 3

Consolidating boundary methods for finding eigenstates of billiards

3.1 Abstract

The powerful plane-wave decomposition method (PWDM) for finding eigenstates of Helmholtz equation can be regarded as a variant of the mathematically well-established boundary integral method (BIM). The capabilities of the BIM and the PWDM are discussed using a unified framework. This opens the way to further improvements.

3.2 Introduction

Solving the Helmholtz equation within a domain, given Dirichlet boundary conditions, is of great interest in Physics [46] , and has important engineering applications.

Helmholtz‘s equation is the simplest example of a *wave equation*. This equation can describe acoustics waves, microwave systems, and in particular the wavefunction of a quantal particle inside a cavity. It has become a prototype problem in studies of quantum chaos, and has applications in studies of nanoscale mesoscopic devices [15], such as quantum-dots, where the motion of the electrons can be regarded as a free motion within a ‘box’. Of particular interest are the wavefunctions of a stationary particle in a two-dimensional box (so called ‘billiard system’). Solutions of Helmholtz equation have been shown to exhibit the scarring phenomena [21]. Some related properties of the solutions are important for studies of quantum transport.

The wavefunction $\Psi(x)$ of a stationary particle in a two-dimensional (2D) box is a solution of the homogeneous Helmholtz equation $\mathcal{H}\Psi(x) = 0$. The differential operator $\mathcal{H}$ is defined as

$$\mathcal{H} = -\nabla^2 - k^2. \tag{3.1}$$

Note that for the special case $k = 0$, the Helmholtz equation reduces to Laplace's equation. Given a closed boundary we can ask whether this equation has a non-trivial solution that satisfies Dirichlet boundary conditions $\Psi(x) = 0$. The values $k = k_n$ for which there are non-trivial solutions are the eigenvalues, and the corresponding $\Psi(x)$ are the eigenfunctions.

Two main numerical strategies have been suggested to date in the literature in order to find the eigenstates of Helmholtz equation. The first strategy can be described as a ‘Laplacian diagonalization’. A basis is selected such that the functions it contains satisfy the Dirichlet boundary conditions. For example, in some cases one can use conformal mapping to determine a basis [37] (and see also [31]). After a basis is selected, the Laplacian operator is written in this basis and then diagonalized. In practice, some truncation is required. Consequently the diagonalization determines all the eigenstates up to some maximum wavenumber k_{max}. Thus, the Laplacian diagonalization strategy is inherently limited, and can not be used for the purpose of finding high-lying eigenstates.

The second numerical strategy, which is the object of this chapter, can be described as a 'boundary approach'. This strategy is based on the observation that the eigenfunctions are completely determined by their behavior at the boundary. For 2D billiards the 'Laplacian diagonalization' requires 2D grid calculations. This is a heavy numerical task. The 'boundary approach' on the other hand reduces the calculations to a 1D boundary grid. As we are going to explain, the search of eigenstates can be restricted to a small k window that contains the energy range of interest. Therefore the method is naturally suitable for the purpose of finding high-lying eigenstates.

In the 'quantum chaos' community, two boundary methods are commonly employed. The first one is referred to as the boundary integral method (BIM) [10], while the other is the decomposition method (DEM). The plane-wave decomposition method (PWDM) [22] can be viewed as a special case of the DEM. Related versions of PWDM have been used in [49, 48] and in [5].

Usually, the BIM and the PWDM are considered to be two independent and self-contained procedures, and several studies have been done in order to compare them [30]. In the present chapter, we adopt a different point of view. We regard the BIM and the DEM as a sequence of four independent steps. By doing so, we are going to make the observation that the DEM and the BIM are strongly related. In order to bridge between them, we will highlight an intermediate strategy which we call the gauge-freedom method (GFM). Finally, the general framework that we set opens the way for further improvements [28].

The numerical procedure for finding the eigenvalues and the eigenfunctions can be summarized by a set of four steps that is common to the BIM and the DEM, and as we will show later, to the GFM:

- Choice of a set of basis functions $F_j(x;k)$.
- Definition of the Fredholm matrix $\mathbf{A}_{js}(k)$.
- Procedure for construction of the wavefunction Ψ_r.
- Definition of the quantization measure $S(k)$.

The first step consists of selecting a set of basis functions $F_j(x;k)$ labeled $j=1..N$. All boundary methods rely on basis functions that satisfy the Helmholtz equation *inside* the billiard. Thus, a superposition of such basis functions is an eigenfunction if it vanishes along the boundary. The choices of bases that correspond to the PWDM, to the primitive version of the BIM and to the simplest variation of the GFM are as follows:

$$F_j(x;k) = \cos(\phi_j + kn_j \cdot x) \qquad \text{PWDM} \tag{3.2}$$

$$F_j(x;k) = Y_0(k|x-x_j|) \qquad \text{Y0-BIM} \tag{3.3}$$

$$F_j(x;k) = J_0(k|x-x_j|) \qquad \text{J0-GFM} \tag{3.4}$$

For the purpose of the numerical treatment we represent the boundary by a set of points x_s with $s = 1\cdots M$. In practice, we choose a set of M equally spaced points, so that the spacing is $\Delta s = L/M$ where L is the perimeter of the billiard. Depending on details of the numerical strategy, the number of points along the boundary is either taken to be equal to the number of basis functions ($M = N$), or it may be larger ($M > N$). The Fredholm matrix is defined as

$$\mathbf{A}_{js}(k) \equiv F_j(x_s; k) \tag{3.5}$$

Given k, one may perform the singular value decomposition (SVD) of the matrix $\mathbf{A}$. The normalized right-vector that correspond to the smallest singular value will be denoted by Φ_s, while the corresponding left-vector will be denoted by C_j. The smallest singular value is $||\mathbf{A}\Phi|| = ||\mathsf{C}\mathbf{A}||$.

In the third step, the eigenvectors Φ_s and C_j are used to construct a wavefunction Ψ_r through a linear transformation. We select a grid of points X_r on which the wavefunction $\Psi_r \equiv \Psi(X_r)$ is calculated. In the traditional DEM, the left eigenvector C is used for the purpose of this construction, and the linear transformation which is applied is:

$$\Psi_r = \sum_j \mathsf{C}_j \mathbf{F}_{jr} \tag{3.6}$$

where $\mathbf{F}_{jr} \equiv F_j(X_r; k)$. Note that C contains the expansion coefficients of $\Psi(x)$ in the chosen basis $F_j(x; k)$. For the BIM, the right eigenvector Φ is traditionally used in order to build the wavefunction, and the linear transformation in this case is

$$\Psi_r = \sum_s \mathbf{G}_{rs} \Phi_s, \tag{3.7}$$

where $\mathbf{G}_{rs}$ is the discretized version of the Green function. Thus, the vector Φ_s represents a 'charge' that is distributed along the boundary. For completeness, we explain this point in the next section.

In the final step, a measure $S(k)$ is defined such that $S(k) = 0$ if k is an eigenvalue and $S(k) > 0$ otherwise. In practice, the eigenvalues are determined by searching for the local minima of $S(k)$. By construction, the wavefunction which was built in step three satisfies the Helmholtz equation inside the boundary. Therefore, the most natural choice of $S(k)$ is the 'tension', which is a measure for the roughness of the constructed $\Psi(x)$ along the boundary. This definition of $S(k)$ is traditionally used with the PWDM. Other known possibilities for the measure include the smallest singular value, and the Fredholm determinant of $\mathbf{A}$. These two latter choices of $S(k)$ are the ones that are usually associated with the BIM. In Section 3.6 we discuss the mathematical equivalence of the three possible measures, and compare their respective numerical effectiveness.

The structure of this chapter is as follows: In Section 3.3, we give a concise presentation of the BIM and the related GFM. Strategies for the construction of the wavefunction are discussed in Section 3.4. Section IV explains how the GFM bridges between the BIM and the DEM. Section 3.6 contains a description of the possible choices for the quantization measure, as well as a comparison between the numerical accuracies of the BIM and the PWDM.

The shape that we have studied numerically is presented in Figure 3.1. We have used the cornerless, generic 'Pond' shape in order to avoid a range of problems that arise with more complicated geometries. These problems are the subject of a follow-up study [28], where we suggest effective (mixed BIM/DEM) methods for finding eigenfunctions. This is done using the above theoretical framework, while regarding the 'Pond' shape as a reference against which to judge the effectiveness of our efforts.

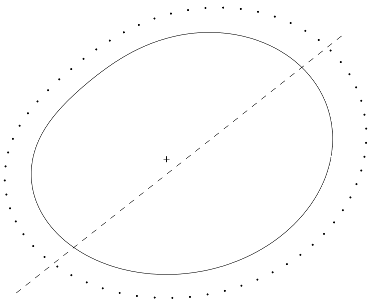

Figure 3.1: Full line: The 'Pond' shape. The polar equation of the Pond shape is $r = 1{+}0.2{*}\cos(\theta{+}0.9{*}\cos(\theta))$. Its radius is roughly 1, and its perimeter is $L = 6.364$. Dashed line: The cross section line that is used e.g. in Figure 3.3c. Dots: The 'outer boundary' which is used for the BIM tension calculation (see Section III-A). The transverse distance between the actual boundary and the outer boundary was chosen in most cases to be $\Delta L \sim 10\Delta s$. Cross: The selected point which is used in Heller's implementation of the PWDM method.

For the convenience of the reader, our numerical notations are concentrated in Table 3.1. Further information about Figure 3.1, Table 3.1, and the numerical analysis is integrated within the main text.

3.3 The BIM and the GFM

The free space Green function $G(x, x')$ is defined by the equation $\mathcal{H}G(x, x') = \delta(x - x')$. The most general solution can be written as

$$G(x, x') \quad = \quad -\frac{1}{4}Y_0(k|x - x'|) \quad + \quad \mathcal{C}(x, x') \tag{3.8}$$

where $\mathcal{C}(x, x')$ is any solution of the homogeneous equation $\mathcal{H}\mathcal{C}(x, x') = 0$. Note that in the electrostatic limit $k \to 0$ we have $G(x, x') = -(1/(2\pi))\ln(r) + \mathcal{C}$, where $\mathcal{C}$ is a constant. We shall refer to the choice of $\mathcal{C}(x, x')$ as gauge freedom.

By the definition of the Green function, it follows that a solution of the generalized

x_s = vector of boundary points
x_{s} = vector of outer-boundary points
X_r = vector of interior grid points
X_0 = a selected interior point

Ψ_r = wavefunction on the grid points
Ψ_s = wavefunction on the boundary points
Φ_s = ‘charge’ along the boundary

$||\Psi_r||$ = norm of the wavefunction (see Section III)
$||\Psi_s||$ = tension of the wavefunction (see Section III)

$n(s)$ = unit normal at the boundary point x_s

$\mathbf{w}_s = (1/(2k^2))\ n(s) \cdot x_s$

$\mathbf{G}_{rs} = G(X_r, x_s)$

$\mathbf{A}_{j0} = F_j(X_0; k)$

$\mathbf{A}_{js} = F_j(x_s; k)$

$\mathbf{D}_{js} = \partial F_j(x_s; k)$

$\mathbf{B}_{ij} = \Delta s\ \sum_s \mathbf{w}_s \mathbf{D}_{is} \mathbf{D}_{js} = \Delta s\ (\mathbf{D}\mathbf{w}\mathbf{D}^\dagger)_{ij}$

$\mathbf{T}_{ij} = \Delta s\ \sum_s \mathbf{A}_{is} \mathbf{A}_{js} = \Delta s\ (\mathbf{A}\mathbf{A}^\dagger)_{ij}$

Table 3.1: Notations

Poisson-Laplace (GPL) equation $\mathcal{H}\Psi(x) = \rho(x)$ is

$$\Psi(x) = \int G(x, x')\rho(x')dx' \tag{3.9}$$

We refer to $\rho(x)$ as the 'charge density', by analogy to its electrostatic equivalent. We shall use the notation $\Phi(s)$ in order to refer to (surface) charge density upon the boundary. In the latter case, the equation above reduces to

$$\Psi(x) = \oint G(x, x(s))\Phi(s)ds \tag{3.10}$$

where s parameterizes the boundary. For numerical purposes, it is convenient to use the discretized version Equation (3.7) of the above formula: the Green function matrix is $\mathbf{G}_{rs} = G(X_r, x_s)$, and the boundary charge vector is $\Phi_s = \Phi(s)\Delta s$, where Δs is the spacing between the boundary points.

3.3.1 The BIM

Let us assume that k is an eigenvalue of the Helmholtz equation with Dirichlet boundary conditions. In such a case, we have a non-vanishing $\Psi(x)$ inside the boundary that satisfies $\Psi(x) = 0$ on the boundary. It follows from Green's theorem that the interior wavefunction satisfies Equation (3.10) with

$$\Phi(s) = \partial_- \Psi(x(s)) \equiv \lim_{x \uparrow x(s)} n(s) \cdot \nabla\Psi(x) \tag{3.11}$$

The unit vector $n(s)$ at the boundary point s is a normal to the boundary and points outward. The notation ∂_- is used for the normal derivative evaluated inside of the billiard walls.

The BIM is based on the above observation, which we would like to paraphrase as follows: If an eigenstate $\Psi(x)$ exists, then there also exists (by Equation (3.11)) a charge density $\Phi(s)$ such that Equation (3.10) is satisfied. In particular, on the boundary we have

$$\int G(x(j), x(s))\Phi(s)ds \;=\; 0 \quad \text{[BIM equation]} \tag{3.12}$$

In other words, having an eigenstate $\Psi(x)$ implies that the kernel $G(x(j), x(s))$ has an eigenvector that corresponds to a zero eigenvalue. The converse is also true: If we can find a non-trivial $\Phi(s)$ that satisfies Equation (3.12), then, using Equation (3.10), we can construct a solution for Helmholtz equation that satisfies Dirichlet boundary conditions. We discuss this construction issue in more details in the next section. Figure 3.2 shows an example of a boundary charge density $\Phi(s)$ that was found via the BIM equation (for more details, see next section).

For numerical purposes, the BIM equation can be written as the matrix equation $\mathbf{A}\Phi = 0$, where $\mathbf{A}_{js} = G(x(j), x(s))$. Using the Neumann Bessel function $Y_0(k|x-x'|)$ for the Green function, one obtains the matrix $\mathbf{A}_{js}$ as defined by Equation (3.5) with (3.3). Another possibility is to use the Hankel Bessel function $H_0(k|x-x'|)$. Accordingly, we will distinguish between the Y0-BIM version and the H0-BIM version. We shall later discuss the numerical implication of using the complex $H(k|x-x'|)$ rather than the real $Y(k|x-x'|)$.

The primitive BIM uses Equation (3.12) literally. It can be easily generalized to handle scattering problems (Appendix A). However, the primitive BIM version is not the one that is generally favored because $G(x(j), x(s))$ is singular for $x(j) \rightarrow x(s)$, leading to some difficulty in determining the diagonal matrix elements of $\mathbf{A}_{js}$. Therefore, another version of the BIM has become popular (see Appendix B). This latter version involves either the $Y_1(k|x-x'|)$ or the $H_1(k|x-x'|)$ Bessel function.

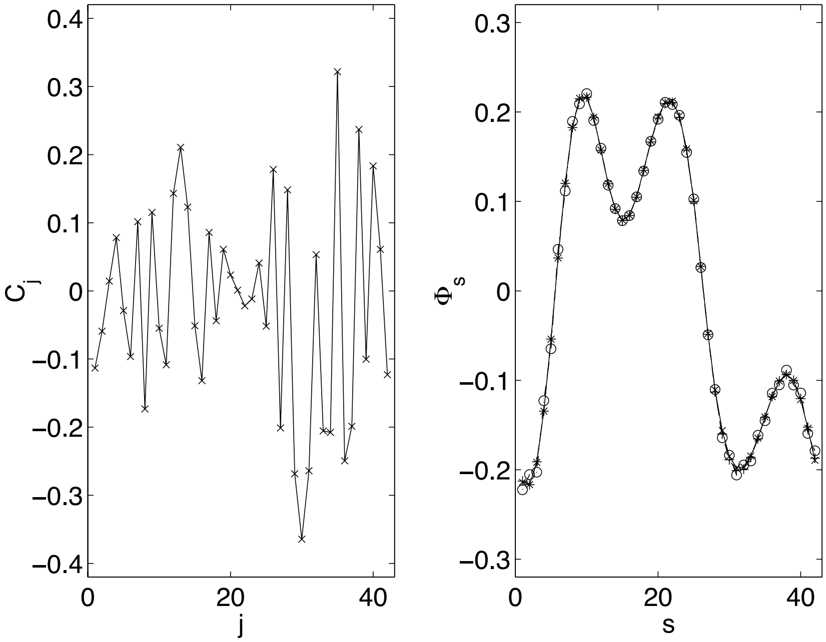

Figure 3.2: The eigenvectors of the Fredholm matrix (Equation (3.5)) are found for $k = k_n = 6.82754592867694$. Right plot: The right-eigenvector Φ. The symbols (x) and (+) and (o) correspond respectively to the PWDM choice of Equation (3.2), to the H1-BIM choice of Equation (3.39), and to the J0-GFM choice of Equation (3.4). Left plot: The left-eigenvector C for the PWDM Fredholm matrix. In the two other cases (H1-BIM, J0-GFM) the Fredholm matrix is symmetric and $\mathsf{C} = \Phi$.

Accordingly, we shall refer to it as either the Y1-BIM or the H1-BIM, respectively.

3.3.2 The GFM

The GFM is a different strategy to obtain the charge density $\Phi(s)$. Rather than using the BIM Equation (3.12) or one of its variants, a gauge freedom argument is invoked in order to introduce a new type of equation (Equation (3.13) below). It is clear that Equation (3.12) should be valid for *any* choice of gauge. In other words, Equation (3.12) should be satisfied with any Green function (Equation (3.8)), whatever is the choice of $\mathcal{C}(x, x')$. Therefore, for a given $\mathcal{C}(x, x')$, the charge density $\Phi(s)$ must satisfy the equation

$$\int \mathcal{C}(x(j), x(s))\Phi(s)ds \quad = \quad 0 \quad \text{[GFM equation]} \tag{3.13}$$

For example, we may take $\mathcal{C}(x, x') = J_0(k|x - x'|)$. In such a case, the GFM equation can be written as the matrix equation $\mathbf{A}\Phi = 0$, corresponding to the choice of Equation (3.4). We shall refer to this version of GFM as J0-GFM.

The kernel $\mathbf{A}_{js} = J_0(k|x - x'|)$ of the J0-GFM is non-singular, and very well-behaved. Thus, the J0-GFM method, unlike the Y0-BIM, provides an extremely convenient way to obtain the eigenvalues of the Helmholtz equation. Figure 3.2 shows an example of a charge density that was found via the J0-GFM equation (for more details see next section). The result is indistinguishable from the $\Phi(s)$ that is generated by the traditional H1-BIM. [We note however that the J0-GFM method has certain numerical limitations that we are going to discuss later]. Once the eigenvector $\Phi(s)$ is found via the GFM equation, we can proceed as with the traditional BIM, and construct the wavefunction $\Psi(x)$ using Equation (3.7).

3.4 Constructing the wavefunction

3.4.1 Green function method (Equation (3.7))

Both the BIM equation (Equation (3.12)) and the GFM equation (Equation (3.13)) can be written as the matrix equation $\mathbf{A}\Phi = 0$ for the charge vector Φ_s. The only difference between the two is in the choice of $\mathbf{A}$. The numerical procedure for solving the BIM/GFM equation is as follows: Given k, one performs the SVD of the matrix $\mathbf{A}$. Figure 3.4 displays an example of the output of such a SVD procedure. One then finds the right eigenvector Φ that corresponds to the *smallest* singular value. Whenever the smallest singular value equals zero (in a numerical sense), the Φ constitutes a non-trivial solution of the BIM/GFM equation, and the corresponding $k = k_n$ is an eigenvalue of the Helmholtz equation.

Once the charge vector Φ_s has been determined, as in the example of Figure 3.2, one can construct the wavefunction using Equation (3.7). For the Green function (Equation (3.8) it is most natural to use the simplest gauge ($\mathcal{C} = 0$). Any different gauge should give the same result, and in particular any complex part should vanish anyway. The outcome of the Green function method is illustrated in Figure 3.3. In the following paragraphs we are going to discuss the practical issue of wavefunction normalization, and then to explain why the constructed wavefunction vanishes outside of the boundary.

In a practical numerical implementation, the vector Φ_s is normalized in the sense $\sum_s |\Phi_s|^2 = 1$, and therefore Ψ_r does not have proper normalization within the interior region. Adopting the usual philosophy of boundary methods, the problem of

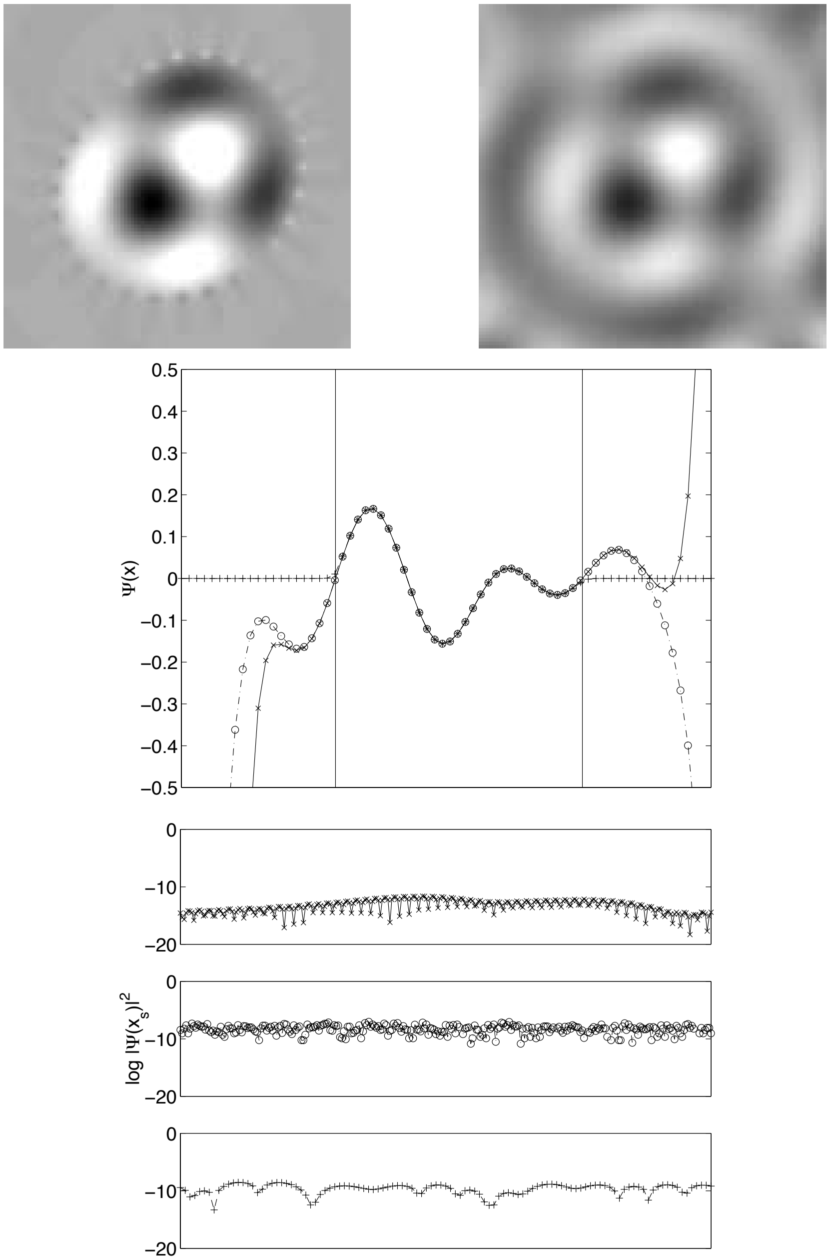

Figure 3.3: The eigenfunction at $k = k_n$ is found using the eigenvectors of Figure 3.2. (a) An image of $\Psi(x)$ using Equation (3.7). (b) The same using PWDM and Equation (3.6). (c) Plot of $\Psi(x)$ along the cross section line of Figure 3.1. The vertical lines indicate the location of the boundary. The wavefunctions that correspond to images a-b are shown with (+) and (x) respectively. We also show with (o) the wavefunction that is obtained using J0-GFM and Equation (3.6). Panels d-e-f display plots of $\log(|\Psi(x)|^2)$ along the boundary. The symbols are as in c.

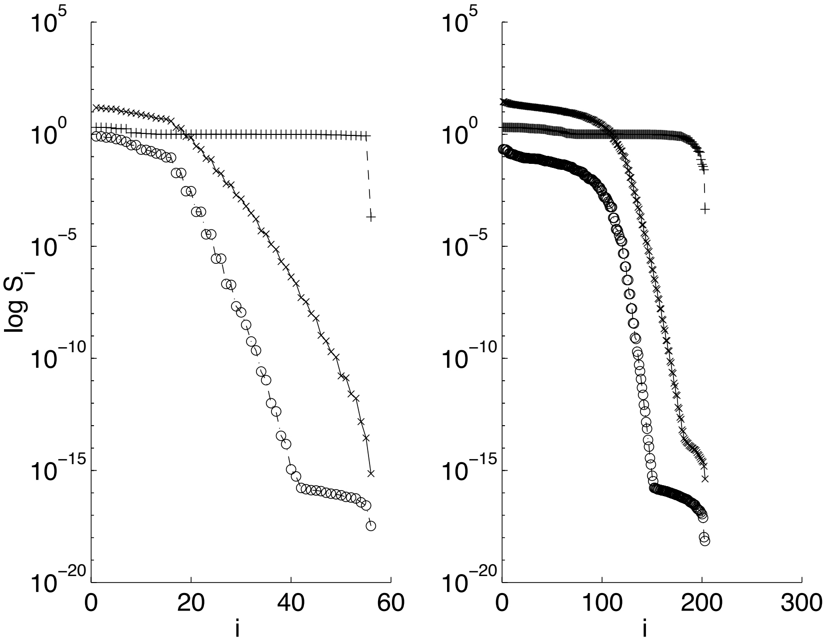

Figure 3.4: Singular values of the Fredholm matrix for $k_n = 6.82754592867694$ (left panel) and for $k_n = 50.05474912004408$ (right panel). The various symbols are as in Figure 3.2.

calculating the Ψ_r normalization is reduced to that of evaluating a boundary integral, namely [10, 13]

$$\int |\Psi(x)|^2 dx = \frac{1}{2k^2} \oint |\Phi(s)|^2 (n(s) \cdot x(s)) ds \tag{3.14}$$

By discretizing Equation (3.14), we obtain the following numerical expression for the proper normalization factor:

$$\|\Psi_r\| \quad = \quad \frac{1}{\Delta s} \sum_s \mathbf{w}_s (\Phi_s)^2 \quad = \quad \Phi^\dagger \mathbf{W} \Phi \tag{3.15}$$

where $\mathbf{W} = (1/\Delta s)\mathrm{diag}(\mathbf{w}_s)$ is a diagonal matrix, and the weight factor $\mathbf{w}_s$ is defined in Table 3.1.

Once we have settled the question of the wavefunction inside the boundary, it is natural to ask what is $\Psi(x)$ outside of it. The answer turns out to be $\Psi(x) = 0$. For completeness, we give a proof of this statement. Let us define an extended function $\Psi_{\mathrm{ex}}(x)$ such that $\Psi_{\mathrm{ex}}(x) = \Psi(x)$ inside and $\Psi_{\mathrm{ex}}(x) = 0$ outside of the boundary. We would like to show that $\Psi(x)$ as defined by Equation (3.10) is also equal to $\Psi_{\mathrm{ex}}(x)$ outside of the boundary. It is clear that $\Psi(x)$ is a solution of the GPL equation by construction [see discussion following Equation (3.9)]. In the next paragraph, we are going to argue that $\Psi_{\mathrm{ex}}(x)$ is a solution of the *same* GPL equation. It follows that the difference $R(x) = \Psi(x) - \Psi_{\mathrm{ex}}(x)$ is a solution of Helmholtz equation in free space. From the definition of $\Psi_{\mathrm{ex}}(x)$, we have $R(x) = 0$ in the interior region, which implies by the unique continuation property that $R(x) = 0$ over all space.

The proof that $\Psi_{\mathrm{ex}}(x)$ is a solution of the GPL equation with a charge density given by Equation (3.11) goes as follows: By construction, $\Psi_{\mathrm{ex}}(x)$ satisfies the GPL equation inside as well as outside of the boundary. All we have to show is that it also satisfies the GPL equation across the boundary. The latter statement is most easily established by invoking Gauss' law. This approach is valid because at short distances, $G(x, x')$ coincides with the electrostatic Green function. Thus, the gradient of $\Psi_{\text{ex}}(x)$ corresponds, up to a sign, to the electric field. Gauss' law implies that the electric field should have a discontinuity equal to the charge density $\Phi(s)$. Indeed, $\Psi_{\text{ex}}(x)$ is consistent with this requirement.

The numerical wavefunction Ψ_r satisfies Helmholtz equation in the interior region *by construction.* Thus, whether Ψ_r is an actual eigenstate depends on its behavior near the boundary. Following [22] we would like to define a 'tension' measure in order to estimate whether, and to what accuracy, the numerical Ψ_r satisfies the boundary conditions. In the context of the PWDM, the tension is defined as the integral of $|\Psi(x)|^2$ along the boundary. For the BIM on the other hand, this definition is not practical due to the singular nature of the basis functions. For any finite M, the numerical wavefunction blows up at each boundary point. However, since the BIM wavefunction vanishes everywhere outside of the billiard, a numerically unambiguous definition of tension arises as an integral of $|\Psi(x)|^2$ along an outer-boundary:

$$||\Psi_{\mathsf{s}}|| \;=\; \Delta s \sum_{\mathsf{s}} (\Psi_{\mathsf{s}})^2 \;=\; \Delta s \sum_{\mathsf{s}} \left(\sum_{s} \mathbf{G}_{\mathsf{s}s} \Phi_s \right)^2 \tag{3.16}$$

By 'outer boundary' (see Figure 3.1), we mean the set of external points (s points, as opposed to s points for the true boundary) that have a fixed transverse distance ΔL from the the true boundary. The distance ΔL between the boundary and the outer-boundary should be small on any classical scale but large compared with ds, in order for the tension to be independent of the choice of ΔL. See Figure 3.5c for a numerical demonstration.

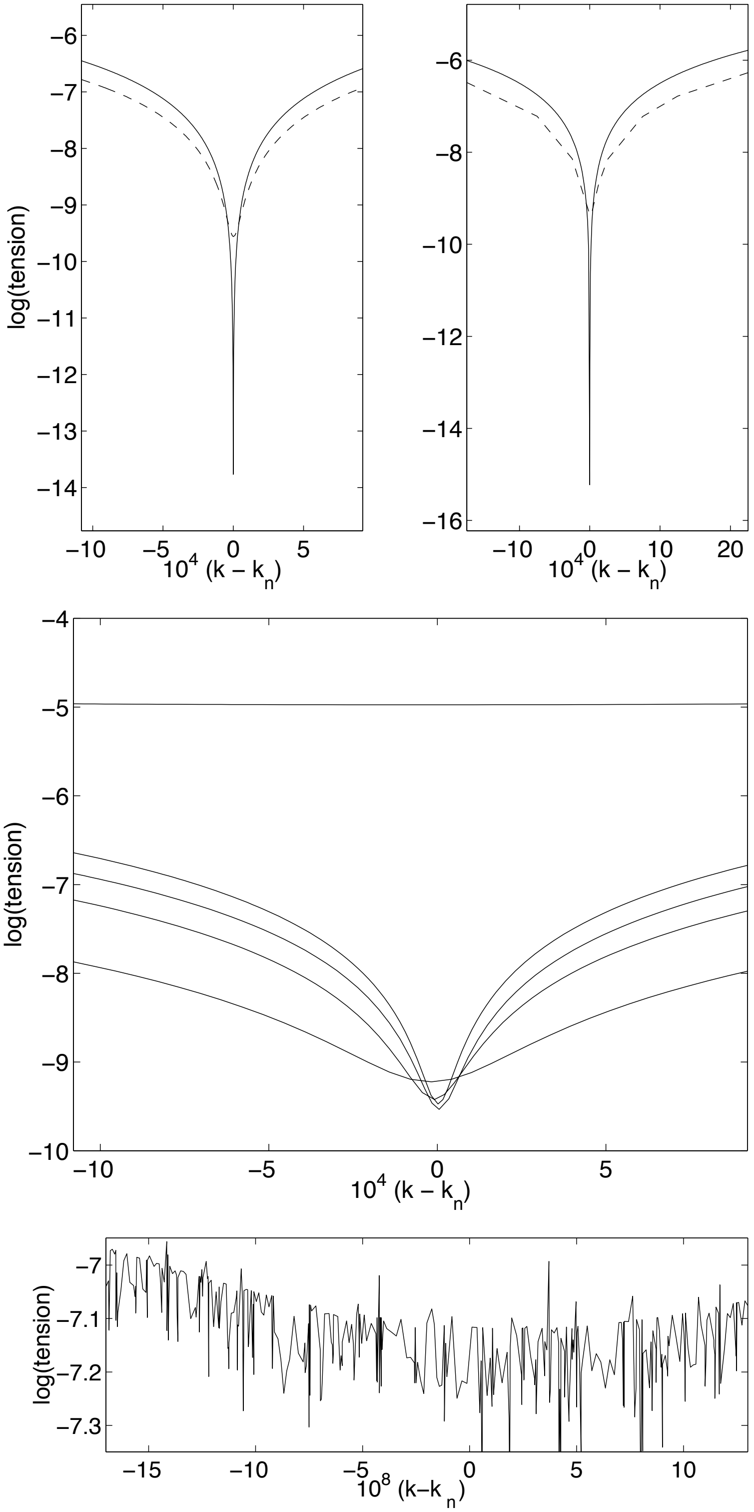

Figure 3.5: The tension as a function of k in the vicinity of $k_n = 10.14707971517264$ (upper-left and lower panels), and of $k_n = 50.05474912004408$ (upper right panel). In the upper panels (a-b) the full line is for the PWDM constructed wavefunction, while the dashed line is for the BIM constructed wavefunction. For the low k state we chose $b = 4$, while for the high k we used $b = 2$. Panel (c) demonstrates the dependence of the BIM tension on the choice of the distance ΔL. The different curves (from the upper to lower) correspond to $\Delta L/\Delta s = 1, 8, 16, 12, 4$. Panel (d) is a zoom over the PWDM minimum.

3.4.2 Decomposition method (Equation (3.6))

The other procedure to construct the wavefunction is to use Equation (3.6). The idea is to regard $F_j(x;k)$ as a basis for the expansion:

$$\Psi(x) \approx \sum_j \mathsf{C}_j F_j(x;k) \tag{3.17}$$

The PWDM is a special case of the DEM, corresponding to the choice Equation (3.2) of basis functions. Any such superposition is a solution of Helmholtz equation within the interior region. Naively, in order to satisfy the Dirichlet boundary conditions, we should look for a vector C of expansion coefficients that satisfy $\mathsf{C}\mathbf{A} = 0$. However, the actual implementation of this idea is associated with a numerical problem which we are going to explain below. In later subsections, we discuss the actual methods for the determination of C.

In Figure 3.2, we display an example of a numerically determined C for one of the Pond eigenstates, while in Figure 3.3 we illustrate the constructed wavefunction. Unlike the Green function construction, the DEM/PWDM constructed wavefunction does not vanish outside of the boundary. Actually, it is quite the opposite: Typically the DEM/PWDM wavefunction becomes exponentially large as we go further outside. Whenever this happens, it constitutes an indication for the *evanescent* nature of the wavefunction. Namely, in typical cases, in order to accommodate itself to the boundary, the wavefunction should contain sub-wavelength features. This requires exponential behavior (negative kinetic energy) in the transverse space direction.

One may think that a practical numerical definition for C would be as the (left) eigenvector that corresponds to the smallest singular value of $\mathbf{A}_{js}$. However, in a practical numerical procedure, this definition is hard to implement. This difficulty can be explained by looking at the behavior of the singular values of $\mathbf{A}_{js}$. Figure 3.4 gives some examples for the singular values which resulted from the SVD of the $\mathbf{A}_{js}$ matrix. In the case of the PWDM, as k become large, one observes that the the singular values separate into two groups: rather than having one distinctly smaller singular value, we obtain a whole set of them. Accordingly, we can define a numerical 'null space' of the $\mathbf{A}_{js}$ matrix. The interpretation of this null space is quite clear. It is well known [17, 19] that it is not efficient to include much more than N_{sc} plane waves in the basis set $F_j(x;k)$, where

$$N_{sc} \;=\; \frac{1}{\pi}kL \tag{3.18}$$

and L is the perimeter of the billiard. The reason for this ineffectiveness is that k_i and k_j cannot be distinguished numerically within the interior region unless $|k_i - k_j|L > 1$. In order to obtain the semiclassical result (3.18), we divide the total phase space area $(L \times (2mv))$ of the boundary Poincaré section by the size of Planck cell $(2\pi\hbar)$. If we use $N > N_{sc}$ plane waves, then we can create wavefunctions that are nearly zero in the interior, and become large only as we go far away from the center. Such superpositions are called 'evanescent' [7]. It is clear that the SVD can be used to determine the $N - N_{sc}$ null space of evanescent states. Whenever k is an eigenvalue, this null space includes, in addition to the evanescent waves, the single eigenvector that constitutes an eigenstate of the Helmholtz equation. The problem is to distinguish this eigenvector from the other vectors in the null-space.

For the later numerical discussion of the PWDM, it is useful to characterize the numerics using

$$b \;=\; \frac{N}{N_{sc}} \;=\Big|_{M=N}\; \frac{\lambda/2}{\Delta s} \tag{3.19}$$

The latter equality holds if we take $M = N$, leading to the interpretation of b as the number of boundary points per half De-Broglie wavelength. If $b < 1$ the null space problem does not exist, and we can define C as the (left) eigenvector that corresponds to the smallest singular value of $\mathbf{A}_{js}$. Of course, we want to push PWDM to the limit, and therefore in practice we always take $b > 1$. One may naturally wonder whether choosing a very large b is numerically useful. Or, as a related issue, whether one gains anything from taking $M > N$. In the following section, it will become clear that taking $b > 1$ does improve the numerics, while $b \gg 1$ generally leads to instabilities that should be avoided. The optimal choice of b depends on the details of the implementation and on the computer hardware. It should be clear that if the numerical accuracy were unlimited, then the $b \to \infty$ limit should lead to numerically exact solutions, though the convergence may be very very slow. This follows from the observation that plane-waves can serve as a complete basis: In principle any evanescent feature of the wavefunction can be reconstructed by a suitable superposition of plane-waves [7]. As for the the $M > N$ issue, contrary to the impression that one may form from reading past literature, our experience (and see also [5]) has been that using $M > N$ does not have a significant effect. Therefore, as a default we simply take $M = N$.

Finally, it should be noted that an effective way to get significant improvements with the DEM is to increase N by going beyond the PWDM. By adding different types of functions into the expansion, we can effectively increase N_{sc}. Specific ad-hoc recipes for this kind of improvement has been introduced in past literature (see e.g. [48]). In a follow-up paper [28] we integrate these and other recipes into the present unified framework.

3.4.3 The metric method

The mathematically 'clean' solution for the null-space problem is to adopt a metric method. Unfortunately, as we explain in the next few paragraphs, this procedure is sensitive to cumulative numerical errors. What we are going to discuss is the straightforward version of the metric method. A modified implementation of the metric method, that avoids some of the numerical problems to be discussed below, had been introduced by Barnett [5].

In practical numerical implementations, the vector C_j is normalized in the sense that $\sum_j |\mathsf{C}_j|^2 = 1$. Therefore, Ψ_r of Equation (3.6) is not normalized appropriately within the interior region. By using the derivative of Equation (3.17) in Equation (3.11), and substituting into Equation (3.14), we get the following numerical expression for the proper normalization factor:

$$\|\Psi_r\| = \Delta s \sum_s \mathbf{w}_s \left(\sum_j \mathsf{C}_j \mathbf{D}_{js} \right)^2 \tag{3.20}$$

$$= \sum_{ij} \mathsf{C}_i \mathbf{B}_{ij} \mathsf{C}_j = \mathsf{C}\mathbf{B}\mathsf{C}^\dagger \tag{3.21}$$

The definitions of D_{js} and of the metric B_{ij} can be found in Table 3.1. Following [22] the tension is defined as the boundary integral

$$\|\Psi_s\| = \Delta s \sum_s \left(\sum_j \mathsf{C}_j \mathbf{A}_{js} \right)^2 \tag{3.22}$$

$$= \sum_{ij} \mathsf{C}_i \mathbf{T}_{ij} \mathsf{C}_j = \mathsf{C}\mathbf{T}\mathsf{C}^\dagger \tag{3.23}$$

The standard practice to date for the tension calculation has been to use a denser set of boundary points located between the x_s points. However, our experience (see also [5]) is that the tension estimate obtained from the initial set of points is just as effective. This is demonstrated in Figure 3.3d. Therefore we routinely rely on the same set of boundary points to determine the tension.

The normalization $||\Psi_r||$ and the tension $||\Psi_s||$ can be calculated using the metrics $\mathbf{B}_{ij}$ and $\mathbf{T}_{ij}$ respectively. This method looks quite elegant, but it turns out not to be very effective numerically. Consider Equation (3.20). This equation is quite safe computationally for two reasons: (i) all its terms are non-negative; (ii) standard summation routines order these terms in descending order. Now, let us look instead at Equation (3.21). In this case the numerical calculation can give *any* result (if we go to large k). Sometimes, the answer even comes out to be negative! This occurs because the calculation involves many arbitrarily ordered terms that each have a different algebraic sign.

The metric method works as follows: First, one finds the basis in which the normalization metric $\mathbf{B}_{ij}$ becomes δ_{ij}. The tension metric $\mathbf{T}_{ij}$ should then be written in that same basis. The SVD is done on the transformed tension metric. In this case, the null space becomes at most one-dimensional (whenever $k = k_n$). Unfortunately, this elegant and straightforward metric scheme does not work very well, due to the finite precision problems discussed in connection with Equation (3.21) and Equation (3.23). Furthermore, **B** and **T** are ”squares” of **A**, which leads to a loss of numerical precision compared with an **A**-based strategy.

3.4.4 Heller's method

The most widely used **A**-based strategy is referred to as Heller's method [22]. The idea is to find C_j as the solution of the $M \geq N$ set of equations $\sum_j \mathsf{C}_j \mathbf{A}_{js} = 0$, with the additional constraint $\sum_j \mathsf{C}_j \mathbf{A}_{j0} = 1$. Table 3.1 gives the definition of $\mathbf{A}_{j0}$.

By constraining the wavefunction to be $\Psi(X_0) = 1$ at a selected point X_0 in the interior of the billiard, we eliminate the problems associated with evanescent states, so that we no longer have the null-space problem. As a result, quite large b can be used without encountering numerical instabilities. The only worry with this method is that X_0 may happen to be very close to a nodal line. In such cases, the tension will be large due to improper normalization, so we will miss these eigenstates.

3.5 The GFM and DEM

In addition to providing a boundary method of its own, the GFM also serves to bridge the gap between the BIM and the DEM. Consider the version of the GFM that is based on the choice $\mathcal{C}(x, x') = F_j(x; k)$, where the F_j are solutions of the Helmholtz equation in free space (with neither singularities nor cuts). With this choice, we immediately realize that the DEM and the GFM are dual methods:

$$\mathbf{A}\Phi = 0 \qquad \text{[GFM equation]} \tag{3.24}$$

$$\mathsf{C}\mathbf{A} = 0 \qquad \text{[DEM equation]} \tag{3.25}$$

The only difference lies in whether one looks for the *left* or the *right* eigenvector. This point is numerically demonstrated in Figure 3.2.

The PWDM version of the DEM also satisfies this duality. In this special case, a somewhat more elegant version of the above argument is as follows: Consider the version of the GFM that is based on the choice $\mathcal{C}(x, x') = \exp(ikn_j \cdot (x - x'))$, where n_j is a unit vector in a given direction. We can take N different choices of n_j, thus obtaining the matrix equation $\mathbf{A}\Phi = 0$ with

$$\mathbf{A}_{js} = \exp(ikn_j \cdot x_s) \tag{3.26}$$

An equivalent matrix equation is found by multiplying each equation by $\exp(ik\phi_j)$, where ϕ_j are random phases. We can then take the real part of these equations, thus obtaining a set of equations that involves the same matrix $\mathbf{A}$ as that of PWDM, namely (3.5) with the basis defined by (3.2).

The duality of the PWDM and the GFM is very important from a mathematical point of view. The mathematical foundations of the PWDM are quite shaky. It is clear that PWDM is well-established mathematically if we have a so-called 'inside-outside duality' (IOD) [19]. Having an IOD in a strict sense implies that the boundary of the billiard may be regarded as a nodal line of some plane-wave superposition. Obviously, this is rarely the case [7]. Therefore, one may wonder whether we indeed have $\det(\mathbf{A}) = 0$ whenever $k = k_n$. Using the duality Equation (3.24), it is obvious that the Fredholm determinant is still a useful tool for quantization, even in the absence of an exact IOD.

It is quite clear from the first paragraph of this section that any expansion method can be associated with a corresponding GFM. Whenever the left eigenvector is used with the expansion method, the right eigenvector can be used with the GFM. We have already demonstrated this point in Figure 3.2. Is it possible to make the inverse statement? Do we have a well defined expansion method associated with any GFM?

The answer is negative. We discuss this issue in the rest of this section, and it can be skipped at first reading.

For the following, it is convenient to consider Equation (3.6) as $N \to \infty$. Subsequently, we are going to talk about whether this limit is meaningful. In the case of the usual PWDM, the $N \to \infty$ limit of Equation (3.6) can be written as

$$\Psi(x) = \int_0^{2\pi} C(\theta) d\theta \;\exp(ikn(\theta) \cdot x) \tag{3.27}$$

Similarly, in the case of the J_0 decomposition, using the basis functions of Equation (3.4), we can write in complete analogy:

$$\Psi(x) = \oint \Phi(s) ds \; J_0(k|x - x(s)|) \tag{3.28}$$

In writing Equation (3.28) we have used the fact that $J_0(x(j) - x(s))$ is a symmetric kernel, and therefore we could make the substitution $\mathsf{C} = \Phi$.

Equation (3.28) looks at first sight like an innocent variation of Equation (3.27). The Bessel function J_0 is just a superposition of plane waves, and therefore one may possess the (incorrect) idea that there is a simple way to go from Equation (3.28) to Equation (3.27). If we expand each J_0 in Equation (3.28) in plane waves, and re-arrange the expression in order to identify the PWDM coefficients, we end up with the relation

$$\mathsf{C}(\theta) = \int \mathrm{e}^{-ikn(\theta)\cdot x(s)} \; \Phi(s) ds \tag{3.29}$$

This relation implies the trivial result $\mathsf{C}(\theta) = 0$ due to gauge freedom [see discussion of Equation (3.26)]. Hence we conclude that the constructed wavefunction is $\Psi(x) \equiv 0$ in the $N \to \infty$ limit!

Having $\Psi(x) \equiv 0$ from Equation (3.28) could have been anticipated using a simpler argument: We know that Equation (3.10) should hold for *any* gauge choice. This gauge freedom implies that we have

$$\oint \mathcal{C}(x, x(s))\Phi(s)ds \quad = \quad 0 \tag{3.30}$$

The above equation should hold for any x inside as well as on the boundary. Furthermore, the left hand side of (3.30) is manifestly a solution of Helmholtz equation in free space, and it follows from the unique continuation property that Equation (3.30) holds also for points outside of the boundary. Having $\Psi(x) = 0$ as a result of the integration in Equation (3.28) is just a particular case of Equation (3.30).

In spite of the observation that Equation (3.28) yields $\Psi(x) \equiv 0$ in the $N \to \infty$ limit, the vector Ψ_r is non-zero numerically for any finite N. In fact, after proper re-normalization, Ψ_r becomes a quite good approximation to the wavefunction (see Figure 3.3c and Figure 3.3e). Sometimes the result so obtained is even better than the one which is found via the traditional BIM Equation (3.7). As strange as it sounds, this success is entirely due to the fact that we are using finite N.

3.6 The quantization measure

Once we have constructed the wavefunction at a given k, the next step is to determine whether Ψ is an eigenstate. As we will explain below, our choice of measures reduces to finding the minima of one of:

$$S(k) \quad = \quad \text{tension} \tag{3.31}$$

$$S(k) \quad = \quad \text{smallest singular value} \tag{3.32}$$

$$S(k) \quad = \quad \text{determinant} \tag{3.33}$$

Here, 'determinant' is used to represent the product of all the singular values. Two questions arise: (i) Are these measures mathematically equivalent? (ii) Are they numerically equivalent? The first of these questions is easily resolved, while the second one requires a somewhat more lengthy discussion.

We first settle the simpler question of the mathematical equivalence. The BIM Equation (3.12) and the GFM Equation (3.13) can both be written as $\mathbf{A}\Phi = 0$, with the appropriate choice of $\mathbf{A}$. Thus, if k is an eigenvalue, $\mathbf{A}$ must have a singular value that tends to 0 as N is increased. The determinant is just the product of all the singular values, and therefore it vanishes whenever one of the singular values does. At the same time, the constructed wavefunction should have small tension. It follows that low tension must be correlated with having vanishingly small singular value. Thus in the large N limit all three quantization measures are mathematically equivalent.

The argumentation above implies that neither the traditional implementation of PWDM, nor that of the BIM should be considered to be 'package deals'. For example, the BIM could be used with the tension as a measure, rather than looking for minima of the the singular values. Similarly, the usual Heller method for the PWDM could be replaced by a search over determinant values.

3.6.1 The tension as a quantization measure

The tension is a robust measure for quantization. Figure 3.5 displays some examples of the corresponding $S(k)$ plots. The PWDM minima are typically much 'sharper' than their BIM equivalents. Zooming over a PWDM minimum (Figure 3.5d) reveals some amount of roughness. This feature is actually helpful, because it gives an indication of and control over the stability of the numerics. We interpret the roughness of the PWDM minimum as a reflection for the existence of a null-space. In the same spirit, the smoothness of the BIM minima can be regarded as an indication that better accuracy can be obtained by making N larger. We discuss this issue further below.

The tension provides a common measure that may be used to monitor improvements, as well as to compare the success of the different methods. Naturally, the first issue to discuss is the dependence of the tension on the size N of the basis set (see Figure 3.6). For the BIM, the tension becomes better as N grows, and disregarding the computer hardware, there is no reason to suspect that there is an inherent limitation on the accuracy. The situation is different for the PWDM. Here, taking N much larger than N_{sc} is not effective. In practice, the method reaches a limiting accuracy, which, taking into account present hardware limitations, is still very good compared with that of the BIM.

From Figure 3.6, it is also clear that the tension of the PWDM becomes much better as k becomes larger. This is expected on the basis of the following semiclassical reasoning: larger uncertainties in k result from confining a particle to a smaller box (taking a smaller box for a given k is equivalent to making k smaller for a given box size). Thus, it is more difficult to build a wavefunction with a precise value of $|k_j| = k$ for low lying eigenstates. On the other hand, the BIM does not seem to be sensitive to the value of k.

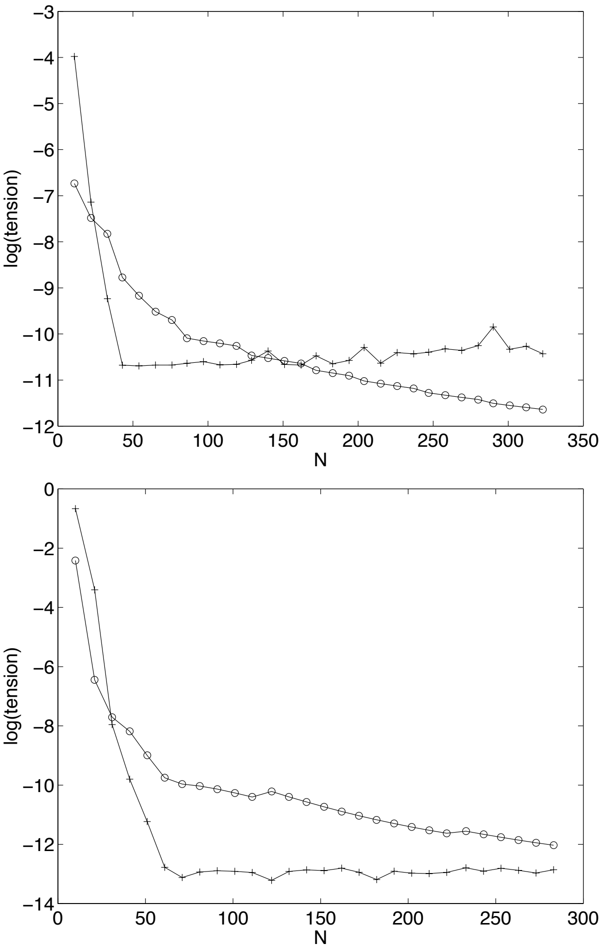

Figure 3.6: The tension for the constructed eigenstate versus the number N of basis functions. The upper panel is for the $k_n = 2.40425657792391$ eigenstate, and the lower panel is for the $k_n = 6.82754592867694$ eigenstate. The symbols (o) and (+) are for the BIM and for the PWDM, respectively.

The tension can be regarded as a measure of the *local error* in the determination of the eigenfunction. The tension is 'local' in the sense that it pertains only to points along boundary. We can also define a measure for the *global error*: That is the error which is associated with all the interior points.

$$(\Delta\Psi)^2 \quad = \quad \langle|\Psi_r - \Psi_{\text{exct}}(X_r)|^2\rangle \tag{3.34}$$

Here $\Psi_{\text{exct}}(x)$ is the numerically exact wavefunction. The average is taken over the set X_r of selected points inside of the boundary. Figure 3.7 gives an example for the variation of the error along the cross section line of Figure 3.1. In order to eliminate a possible bias due to a global normalization-error, we re-renormalized the 'non-exact' wavefunction so that $\Psi_r = \Psi_{\text{exct}}(X_r)$ at the selected point $X = X_0$. In retrospect, we realized that such an error did not significantly affect the result. However, we still chose to be on the safe side, and we adopted this procedure routinely.

It is natural to expect the average error $(\Delta\Psi)^2$ to be correlated with the tension. In other words, if $|\Psi_r - \Psi_{\text{exct}}(X_r)|$ is small on the boundary, then one may expect it to be small in the interior. The degree of such correlation is important for practical reasons. Moreover, we have introduced two different versions of tension definitions, one for each of the PWDM and the BIM. It is not a-priori clear that the above correlation is independent of the choice of numerical method. In Figure 3.8, we study this issue by plotting $(\Delta\Psi)^2$ against the tension for the BIM and the PWDM. In the case of the PWDM, the error saturates below a critical tension. Below this point, further improvements on the boundary do not seem to affect the bulk of the eigenstate. It is not clear from the numerics that the BIM show this saturation. In any case we see that for the same tension, the BIM does a poorer job in reproducing the wavefunction inside of the boundary.

The saturation of the error well inside the billiard can be explained as a manifestation of the fact that the wavefunction there is not very sensitive to sub-wavelength roughness of the boundary: If N is reasonably large,the numerical wavefunction vanishes on a nodal line that almost coincides with the true (pre-defined) boundary. Increasing N further affects the sub-wavelength features of the (distance) difference between that nodal-line and the true boundary. This distance difference is important for the tension, but not very it is not very important for the wavefunction well inside the billiard.

3.6.2 The determinant as a quantization measure

As we have already discussed in the introduction, the tension is the natural measure of quantization. However, from a numerical point of view, it is much more convenient and time efficient to compute the singular values of $\mathbf{A}$, without having to find the eigenvectors for each k value, and without having to compute the wavefunction along the boundary (for tension calculation).

The smallest singular value is traditionally used as a quantization measure for the BIM. From Figure 3.7, it is quite clear that one of the singular values is significantly smaller than the others, so that the eigenstate is unambiguously determined by this method. Is it possible to use the same approach, with comparable success, for the PWDM? We have already determined that looking at the smallest singular values is not very meaningful numerically. For $N > N_{sc}$, there exists a large null-space of evanescent states for any k, unless we use a metric method. However, the metric

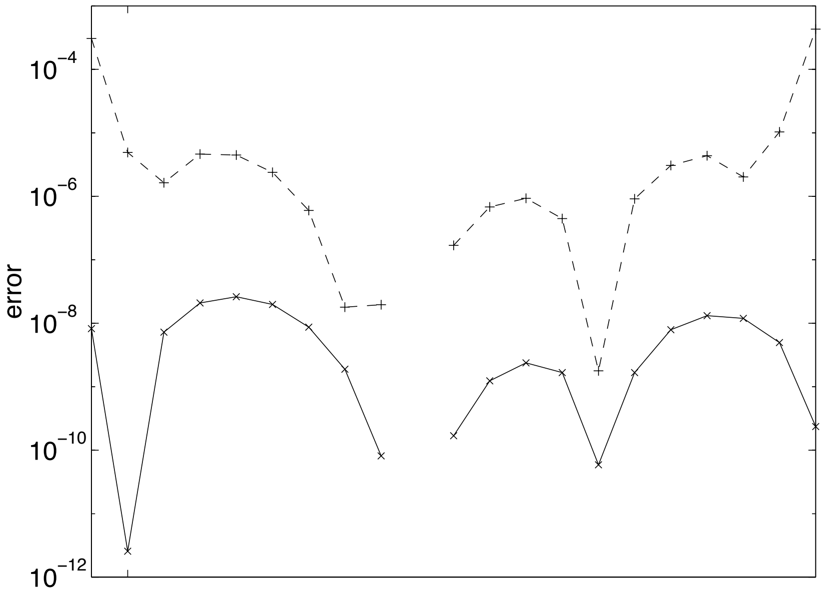

Figure 3.7: Plot of the error $|\Psi_r - \Psi_{exct}(X_r)|^2$, along the cross section line of Figure 3.1. We refer here to the $k_n = 6.82754592867694$ eigenfunction. The numerically 'exact' wavefunction is our best PWDM-constructed wavefunction ($N = 69$) with tension= 10^{-13}. The 'non-exact' wavefunction is either BIM-constructed (+) or PWDM-constructed (x), with tension $\approx 10^{-8}$. In the middle point the error is zero by construction (see explanation in the text).

method is numerically complicated, so let us not take it as a practical option. Can we do better? Each time that $k = k_n$, the null space should include one more 'dimension'. Therefore, the determinant, rather than the smallest singular value, becomes the reasonable quantity to look at. Thus, from numerical point of view, (3.32) should be superior to (3.31).

Figure 3.9 illustrates how the determinant can be used in practice as a quantization measure. As a general rule, as is the case for the tension, the PWDM/GFM minima are 'sharper' than the BIM ones. On the one hand, this extra sharpness can be regarded as an advantage, because it leads to a better resolution of the eigenvalue

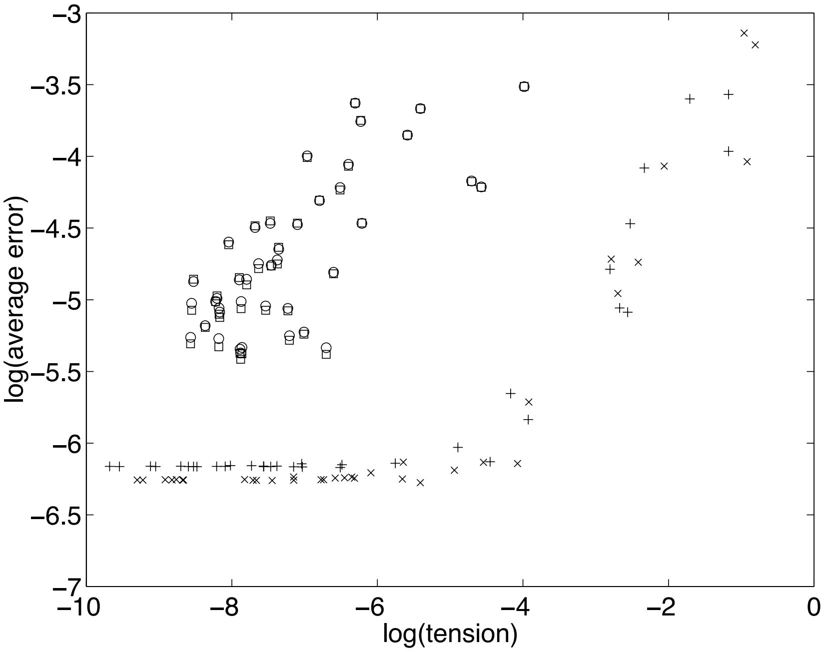

Figure 3.8: The averaged error in the determination of the wavefunction, versus the tension for the $k_n = 6.82754592867694$ eigenfunction. For the BIM-constructed wavefunction we use squares and (o), while for the PWDM one we use (+) and (x). The error has been determined with respect to the 'exact' wavefunction Ψ_{exct}. The latter is numerically defined as either the best BIM eigenstate (squares and (+)) or as the best PWDM one ((o) and (x)). For both choices Ψ_{exct} had a tension better than 10^{-10}.

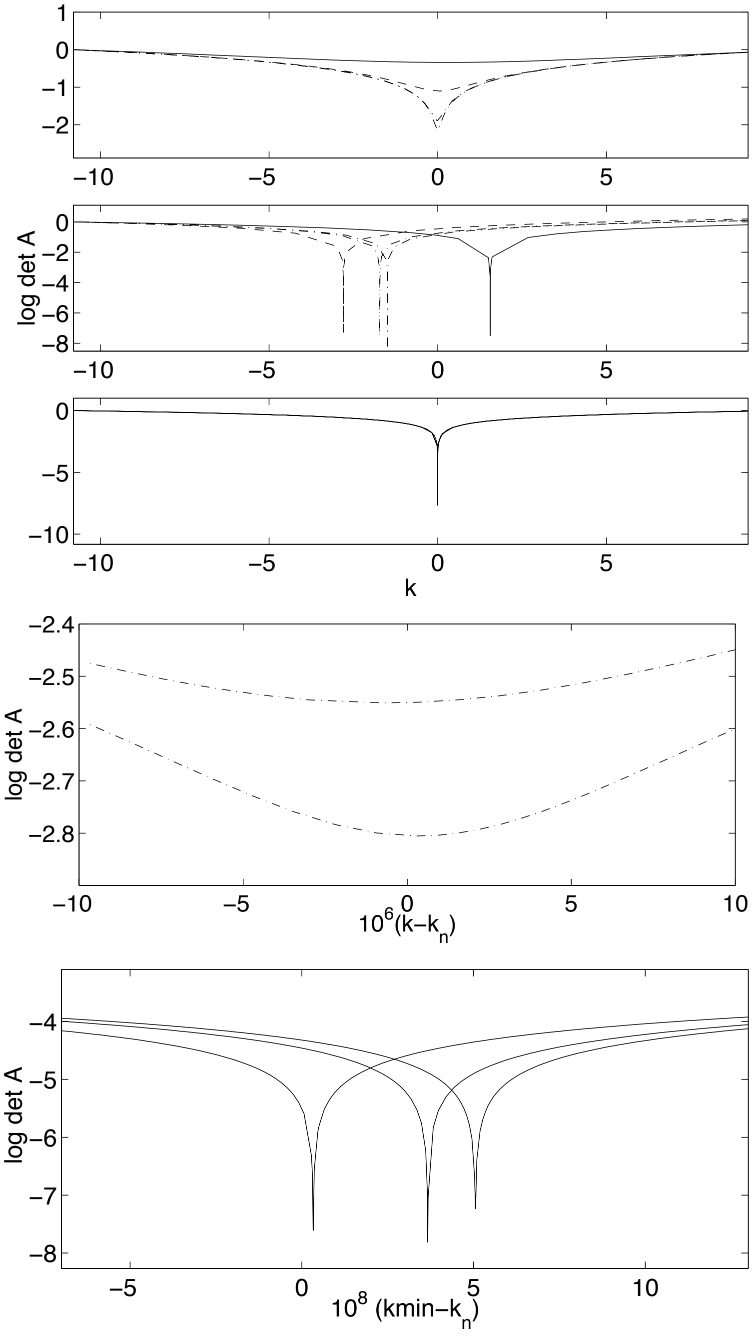

Figure 3.9: The Fredholm determinant ($S(k)$) versus k in the vicinity of $k_n = 10.14707971517264$. Note that $S(k)$ is normalized such that $S(k) = 1$ away from the minima. Panels a-b-c show $S(k)$ in the cases of the H1-BIM, the Y1-BIM and the PWDM, respectively. The lines plotted, in order of decreasing $S(k)$ minimum, correspond to $b = 2, 3, 4, 8$ in panel (a), $b = 4, 8, 13, 12$ in panel (b) and $b = 2$ in panel (c). Panels (d) and (e) give a zoom over the minima of panels (a) and (c), respectively. We witness some numerical instabilities for both the Y1-BIM and the PWDM, though in the latter case it is much much weaker, and can be resolved only in the zoomed plot (panel (e)). For larger b values, the PWDM instability is enhanced, and the results are reduced to numerical garbage (not shown).

spectrum. However, more computer time is needed in order to find these minima. The BIM minima are broader, and therefore 'digging' algorithms that search for local minima become extremely effective.

In the case of the traditional BIM, using a larger N leads to a better resolution of the local minima, as expected. The traditional H-BIM uses the complex Hankel Bessel function as its Green function. One may wonder why the real Neumann function could not be used instead. A-priori, there is no reason to insist on Hankel choice. However, it seems that with Neumann choice the numerics are not very stable: The locations of the local minima vary on a k range which is large compared to their k width. Because of this problem, search routines in case of Y-BIM may yield misleading values for the error in the k_n determination. The numerical stability of the H-BIM can be attributed to the fact that the BIM equation $\mathbf{A}\Phi = 0$ becomes complex. Its real part is just the Y-BIM equation, while its imaginary part is the J-GFM equation. Thus one may say that the H-BIM benefits from combining the Y-BIM with the J-GFM.

Is it always possible to use the Fredholm determinant as a quantization measure in the GFM/PWDM case? Here we observe that the null-space problem is reflected in the stability of the determinant calculation. For $1 < b < 1.8$, we get nice minima, which actually look much sharper than the BIM ones. However, we are faced once again with the usual problem: As we try to increase b in order to improve accuracy, the numerics loose stability. This is illustrated in Figure 3.9 for the PWDM case. The same phenomenon occurs with J0-GFM, which has somewhat larger tendency for instability. This is apparently because the J0-GFM is involved with a larger null-space (see Figure 3.4). The larger null-space in the case of the J0-GFM is probably related to the fact that the J_0 basis functions are quite localized on the boundary, so that as a result they span a smaller space of non-evanescent wavefunctions. Note also our discussion in Section III-C.

3.7 Appendix A: The BIM for the scattering problem

The solution of the Helmholtz equation for the scattering problem is just another variation of the BIM. Consider a boundary, one that in general may be composed of several disconnected pieces. The incident wave $\Psi_{\text{incident}}(x)$ is a solution of Helmholtz equation in free space. Formally, $\Psi_{\text{incident}}(x)$ includes both the ingoing and the outgoing wave components. We look for a solution $\Psi(x)$ that has the same ingoing component as $\Psi_{\text{incident}}(x)$, and that satisfies $\Psi(x) = 0$ on the boundary. Such solution can be written as a sum of the incident wave and a scattered wave, and hence must be of the form

$$\Psi(x) = \Psi_{\text{incident}}(x) + \oint G(x, x(s'))\Phi(s')ds \tag{3.35}$$

Equation (3.35) is a variation of Equation (3.10). Note that the Green function should satisfy outgoing boundary conditions in order to yield the desired solution. The charge density $\Phi(s)$ is fixed by the requirement that $\Psi(x) = 0$, which leads to the boundary equation

$$\oint G(x(s), x(s'))\Phi(s')ds = -\Psi_{\text{incident}}(s) \tag{3.36}$$

This inhomogeneous equation is a straightforward generalization of Equation (3.12). A discretized version of it was used in [14] in order to obtain numerical solutions of the Helmholtz equation for some scattering problems.

The derivation of Equation (3.36) in [14] is much more complicated than ours, and involves the use of Lippmann-Schwinger equation. The boundary is represented by a large delta-potential V, and the limit $V \to \infty$ is taken. Using this procedure, the charge density $\Phi(s)$ can be obtained as the $V \to \infty$ limit of $V\Psi(x(s))$. Note the correctness of the physical units. Namely, $[\mathcal{H}][\Psi] = [\rho]$ and therefore $[V][\Psi] = [\Phi]$. Note also that the wavefunction is in general non-zero in both sides of the boundary. Therefore the charge density $\Phi(s)$ is equal to the *difference* between the normal derivatives on both sides of the boundary. The simplest way to derive the relation between $\Phi(s)$ and $V\Psi(x(s))$ is to integrate the Helmholtz equation over an infinitesimal range across the boundary, as in the treatment of the 1D Schrodinger equation with delta potential.

3.8 Appendix B: Traditional BIM

The primitive BIM equation (Equation (3.12)) is based on Equation (3.10). The traditional BIM is a variation of the same idea. Rather than using Equation (3.10) directly, one considers its gradient, leading to

$$\partial_{\pm}\Psi(x(s)) \;=\; \oint \partial_{\pm}G(x(s), x(s'))\Phi(s')ds' \tag{3.37}$$

This equation is analogous to Equation (3.12). We use the notation ∂_+ and ∂_- in order to refer to the normal derivative on the interior and exterior sides of the boundary respectively. By definition, $\partial_- \Psi(x(s)) = \Phi(s)$, and from the discussion in section III we have $\partial_+ \Psi(x(s)) = 0$. Adding the two equations of (3.37), we obtain

$$\Phi(x(s)) \; = \; \oint 2\partial G(x(s), x(s'))\Phi(s')ds' \tag{3.38}$$

where $\partial \equiv (\partial_+ + \partial_-)/2$ is just the derivative on the boundary in the principal sense. Thus, in the traditional BIM, the definition of the Fredholm matrix is

$$\mathbf{A}_{ss'} \; = \; \frac{1}{\Delta s}\delta_{ss'} \; - \; 2\partial G(x(s), x(s')) \tag{3.39}$$

and the BIM equation (3.38) is $\mathbf{A}\Phi = 0$. The kernel $\partial G(x(s), x(s'))$ is well behaved, and its diagonal elements are finite thanks to the presence of a geometrical factor. Namely, if $G(x(s), x(s')) = g(k|x(s) - x(s')|)$ then

$$\partial G = k\frac{n(s) \cdot (x(s) - x(s'))}{|x(s) - x(s')|} g'(k|x(s) - x(s')|) \tag{3.40}$$

If either one of the Bessel functions H_0 or Y_0 is used for the Green function, then the definition of $\mathbf{A}_{ss'}$ above involves either H_1 or Y_1, respectively.

Chapter 4

Improved boundary methods for the eigenstates of convex billiards

4.1 Abstract

The plane-wave decomposition method (PWDM) for two-dimensional billiards is extended to include basis functions which are solutions of Helmholtz equation inside of the boundary, but are singular at some exterior points. The accuracy of the PWDM is compared for convex and concave triangles. The eigenvalues of a non-convex, multiply-connected billiard are resolved.

4.2 Introduction

The eigenstates of a free particle in a two-dimensional billiards are described by the Helmholtz equation

$$(\vec{\nabla}^2 + k^2)\Psi(x, y) = 0 \tag{4.1}$$

with $\Psi(x, y) = 0$ at the wall. Here k denotes the wavenumber, and $k^2 = E$.

The Plane Wave Decomposition Method was first implemented by Heller [22], and is one of the most successful methods to date at solving the billiard problem. The PWDM is mathematically justified in cases where the shape of the boundary leads to an exact correspondence with the associated scattering problem on the external surface of the billiard. This so called inside-outside duality was studied extensively by Dietz *et al.* [19]. The authors found that whenever the wavefunction $\Psi(x)$ can be analytically continued outside of the boundary, it is possible to write $\Psi(x)$ as an expansion of plane waves $\exp i\vec{k} \cdot \vec{x}$ with $\vec{k} \,\epsilon\, \mathbf{R^2}$ and with finite coefficients. More precisely, it was shown [18] that for energies at which the scattering matrix of the exterior problem has n eigenvalues equal to 1, the inner part of the boundary has an eigenstate of degeneracy n (strong spectral duality).

In all but the simplest shapes, attempts at analytically continuing $\Psi(\vec{x})$ outside of the billiard fail, and the resulting exterior wavefunction will have branch cuts or singularities somewhere in the plane. Thus, the strong spectral duality is not realized for the general billiard. For convex open domains, it can be demonstrated [32] that solutions of the Helmholtz equations can be written as superpositions of plane waves if the components of $\vec{k}$ are allowed to take on complex values (but its norm remains fixed). Furthermore, Berry [7] showed that it was possible to construct the evanescent solutions as sums of plane waves with real wavevectors. Thus, as Gutzkin [20] pointed out, the solutions of equation 4.1 may be approximated as a linear combination of plane waves in convex, bounded domains.

Dietz *et al.* [19] implemented the PWDM for the irrational wedge billiard. For this system, the strong spectral duality does not hold. The solutions inside the billiard consists of Bessel functions of the form $\Psi = \sum_l J_{\pi l/\alpha}(kr)$, where α is the opening angle of the wedge. Thus, for non integer π/α, the extended solutions are not single valued in the plane, and the condition for strong spectral duality is not satisfied. These authors showed that the amplitude of the plane wave coefficients outside of the billiard was several orders of magnitude higher than the wavefunction amplitude inside the billiard. Furthermore, though the convergence improved with the number of basis functions, the divergence of the external coefficients increased.

For such billiards, an exponentially large number of plane waves need to be included in the basis to account for the evanescent wave contribution. The number of useful plane waves in the basis is limited by to Nyquist's theorem to be of the order of one plane wave per half wavelength or $N > N_{sc} = 2L/\lambda$ (see Chapter 3). Beyond that number, the convergence is extremely slow [5]. Therefore, the evanescent solutions must be included directly into the numerics. Unfortunately, no natural truncation exists for the evanescent functions in general, so that the set of optimal evanescent basis functions need to be determined individually for each system. For the stadium billiard, Vergini[49] found that adding evanescent waves at the joint between the straight part of the billiard and the end cap significantly improved the convergence. A similar technique was applied in [50], where evanescent waves were placed at the largest corner of a truncated triangle with rational corners to counteract the diffraction generated at that point.

An even stronger limitation exists in the case of non-convex billiards. Gutzkin [20] demonstrated that the eigenstates of these billiards can not be written in terms of solutions of the Helmholtz equation which are regular over the whole plane. More specifically, Gutzkin looked at the norm of the difference between the plane wave approximation and the true eigenstate over the billiard. He found that billiards containing one periodic orbit whose continuation to the exterior of the billiard crosses the boundary at least once is bounded below by a finite positive constant η_n, where n labels the state. Thus, in such cases, it is necessary to resort to bases that satisfy the Helmholtz equation inside the billiard, but not necessarily outside of it.

In this chapter, we study non-convex billiard shapes in order to find an appropriate basis for their solutions. We chose shapes with generic, symmetry-less boundaries in order for the solutions we obtain to be valid for most of the billiards in these classes. Thus, all our shapes have mixed phase spaces. In the first section, we numerically test Gutzkin's theory by comparing the convergence of the PWDM for triangular billiards with inwardly and outwardly curved boundaries. We then move on to the problem of non-simply connected billiards, which is exemplified by a smooth boundary with a circle cut out of its center.

Figure 4.1: **left** Concave triangle and **right** convex triangle. The concave triangle is composed of 3 arcs of circles of radii 2.1, 2.2 and 2.3. The convex triangle is made of arcs of circles of radii equal to 2.0, 2.1 and 2.6.

4.3 Concave versus convex

In this section, we compare two triangular shapes. One is a concave generalized Sinai billiard, while the other is a convex triangle (Figure 4.8).

According to Gutzkin‘s theory, the eigenstates of the concave triangle should not be solvable using a basis composed only of plane waves.

We looked at a range of states from $n = 1000 - 1500$. The concave triangle calculation was unstable, and did not yield any states. In comparison, for the convex triangle, we found all the states in that range, and average tensions of -5.57, in agreement with our predictions.

4.4 Non-simply connected shapes

Problems with the PWDM are much more severe in multiply connected geometries, as compared to the irrational corners that were considered in the previous section. In fact, all but a few eigenstates of such shapes may be resolved using this

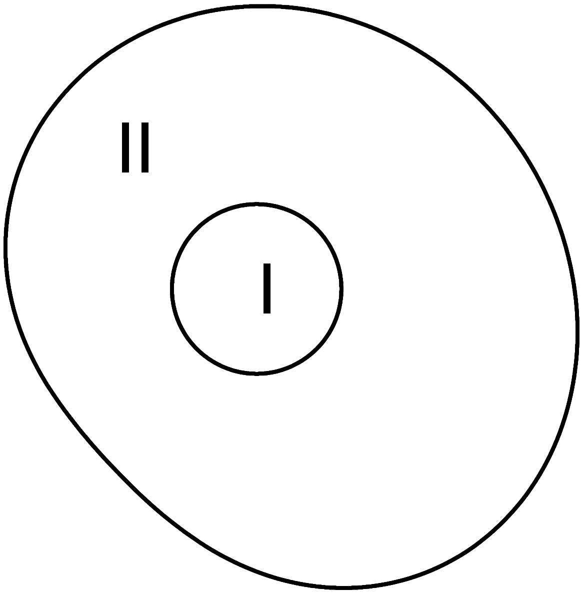

Figure 4.2: Eye shape. The inner boundary is the circle $r = 0.3$, and the equation of the outer boundary is $r = 1 + 0.2cos(\phi + 0.9cos(\phi))$.

method. The failure of the PWDM can be easily understood by considering the example of the eye shape of Figure 4.4. This shape contains two interior regions, labeled I and II. Region II has the topology of an annulus, whereas the exterior boundary is the pond shape described in Chapter 3. It is clear that a continuation of the wavefunction into the pupil region must lead to a complicated structure of cuts and singularities.

Intuitively, the problem with such a geometry becomes evident once we try to apply the PWDM. Strong spectral duality requires that the expansion be vanishingly small on both the inner and outer boundaries, implying that the solution should be a simultaneous eigenstate of regions I and II. The set of such eigenstates has zero measure, with the exclusion of particular systems where some special symmetry forces such a degeneracy. Thus, it is clear that the primitive version of the PWDM will fail in such cases. In particular, since the eye shape is not convex, the addition of evanescent waves will not significantly improve the results. In this case, it is therefore necessary to use solutions which are singular somewhere in the plane outside of the billiard.

For the eye shape, the most natural basis to try is $Y_m(k|x|)\cos(m\arg(x))$ and $Y_m(k|x|)\sin(m\arg(x))$, where $m = 1, 2, 3, \cdots$. However, this basis is particular to the circular inner boundary, and the extension to general billiards is not immediate. Thus, we tried instead a more general basis made out of a single row of Y_0's around the boundary. The Y_0's were placed half a wavelength away from the boundary in order that the wavefunction be well-behaved in the region of interest. The $Y0$s need to be placed a distance less than the wavelength away, so that the regions around the singularity interact with each other. The number of plane waves N_w was again taken to be equal to the number of points N_s in the boundary grid.

In figure 4.5, we plot the tension vs wavenumber for a typical range of 20 eigenstates (according to Weyl's law) at $n = 1000$ for both bases. The basis containing only plane waves misses most of the states. On the other hand, the tensions minima found by including the Y_0s gives sharp and well-defined minima, and very few of the states are missed.

Figure 4.6 displays the tension on the boundary for both bases. For the standard plane wave basis, the tension is much higher around the inner circle. However, once the Neumann functions are included, the tension becomes evenly distributed over the whole length of the wall.

Eigenstates that were found using this method are shown in figure 4.7. Figure 4.7a shows a state generated by the straightforward PWDM. It is clear that it is a

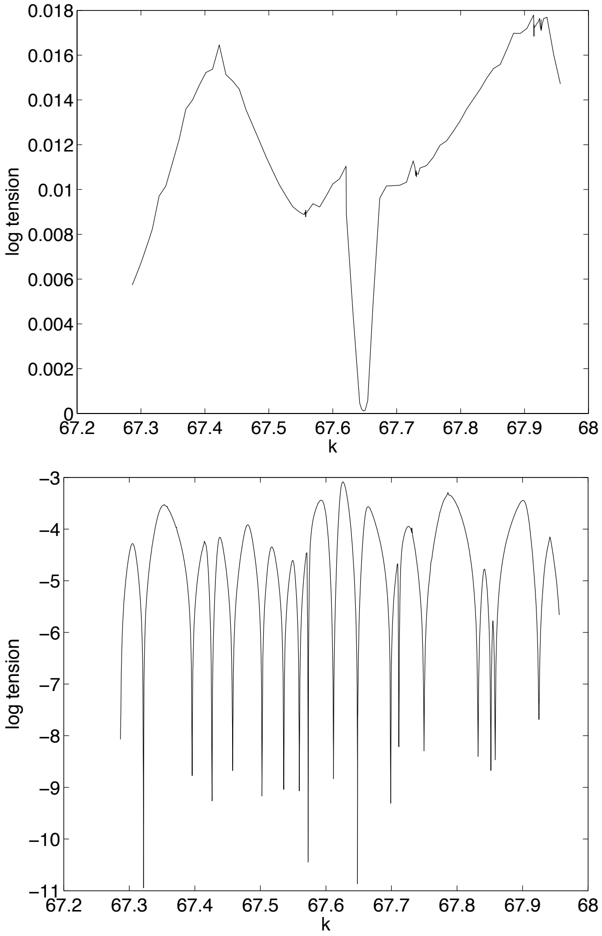

Figure 4.3: Tension vs k around $n = 1000$ for bases composed **top**: of plane waves only **bottom**: of plane waves and 100 Y_0s.

whispering gallery mode, which lives far away from the inner boundary. An eigenstate from the $Y0$ basis in displayed in Figure 4.7b.

4.5 Conclusion

We also compared concave and convex triangles, thereby providing a numerical test of Gutzkin‘s theory. We also showed that the addition of singular basis functions

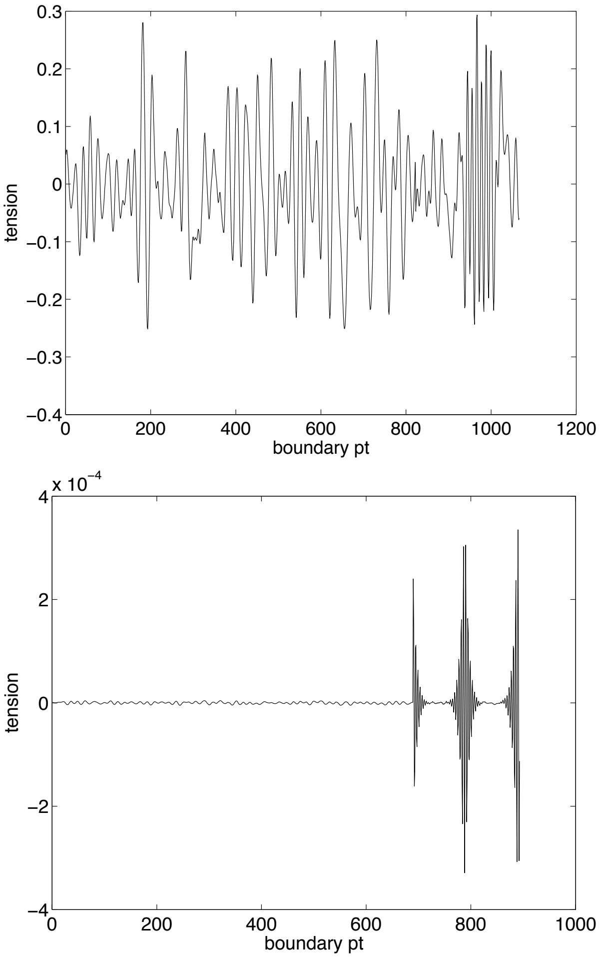

Figure 4.4: Boundary tensions around $n = 1000$ for the bases of Figure 4.6.

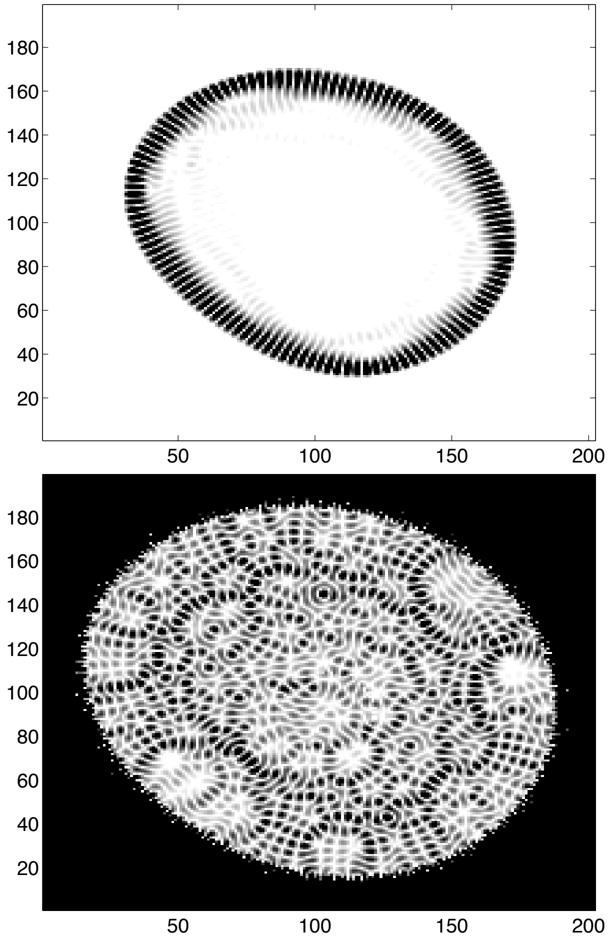

Figure 4.5: Eigenstates at **top**: $k = 67.64851$ and **bottom**: $k = 67.61155$ for the bases of Figure 4.6. Only the wavefunction inside of the boundary is plotted in the top plot.

to the standard plane wave basis of the PWDM significantly improves the tension for non-convex shapes. For the eye billiard, Y_0's were added to the plane waves. It is our hope that this method can be extended in the future to a broader range of shapes.

Chapter 5

Quantum billiards and constrained random wave correlations

5.1 Abstract

We study chaotic eigenfunctions in wedge-shaped and rectangular regions using a generalization of Berry's conjecture. An expression for the two-point correlation function is derived and verified numerically.

5.2 Introduction

According to Berry's conjecture,[6] chaotic eigenfunctions behave locally like random superpositions of plane waves with wavevector k, where $k = (1/\hbar)\sqrt{E - V}$. This description is consistent with random matrix theory. The Gaussian random wave model does not account for the localization properties of eigenfunctions, such as scarring [21] and weak quantum ergodicity.[27] In particular, for quantum billiards with Dirichlet boundary conditions, the wavefunction must vanish at the boundary, and thus no longer looks random in its vicinity. For straight boundaries, the problem can be solved by reducing the set of available plane waves to those which are antisymmetric with respect to reflection across the wall, thereby ensuring a zero value along that boundary; see Berry.[8] If, for instance the boundary is given by the line $y = 0$, the chaotic wave function will be composed of a seemingly random combination of plane waves of the form $\sin(k_y y)\cos(k_x x + \phi)$ where $k_x^2 + k_y^2 = k^2$ and ϕ is a random phase shift. Bies and Heller [11] discuss similar boundary effects in soft potentials.

Some criteria for unconfined random waves appear to be well satisfied by eigenfunctions of chaotic billiards. McDonald and Kaufman [35] and McDonald [33] checked for random nodal patterns, Gaussian statistics and Bessel function correlations. In their original work on the stadium, these authors emphasized the qualitative appearance of nodal lines in the eigenfunctions. The nodal lines appear to wander randomly throughout the billiard, which is indicative of an isotropic distribution of local wave vectors. Furthermore, they found the wavefunction statistics to be Gaussian. However, the correlation function is not a Bessel function for a general billiard.

We first generalize Berry's boundary-adapted form of the Gaussian random wave model to wedge-shaped regions. The case of a 90° angle is immediately solved: one just antisymmetrizes with respect to reflections in both x and y. The simplest non-trivial case consists of a wedge with an opening angle of 60°. We focus on this example in what follows, although our method extends to all opening angles of π/n radians, where n is a positive integer. We first determine the right boundary-adapted plane wave basis. The two-point correlation function can be used to compare our model to numerically generated chaotic eigenstates. For Gaussian random waves in free space, the later is known to give

$$\langle \psi(\mathbf{x}) \bar{\psi}(\mathbf{x}') \rangle = J_0(|\mathbf{x} - \mathbf{x}'|) \tag{5.1}$$

where the average is taken over a set of eigenstates. As we shall see, the two point correlation function for 60° wedge again reduces to a sum of Bessel functions. Our numerically generated ensemble of wavefunctions is compared to this form of the correlation function, including the interference effects of two or more Bessel functions.

Our second type of billiard consists of two semi-infinite parallel lines at $x > 0, y = \pm a/2$, which are connected by a perpendicular wall at $x = 0$. The wavefunction can be made to vanish on the back wall by antisymmetrizing it with respect to the y-axis. The parallel walls are not so readily handled. The antisymmetrization procedure extends over an infinite periodic array of such lines a distance a apart. The two-point correlation function will be composed of an infinite sum of Bessel functions. Since the later diminish rapidly with distance, only the nearest neighbours contribute, allowing us to compare our formula with its numerically determined value.

5.3 The two-point correlation function

5.3.1 The wedge

We first look for the properly antisymmetrized wavefunctions. Let

$$\psi(\mathbf{x}) = \int d\theta a_\theta e^{-i\mathbf{k}_\theta \cdot \mathbf{x} + i\delta_\theta} \tag{5.2}$$

denote a random sum of plane waves. Here $\mathbf{k}_\theta = k\cos\theta\hat{\mathbf{x}} + k\sin\theta\hat{\mathbf{y}}$, the a_θ are independent Gaussian distributed random variables and the δ_θ are independent uniformly distributed random phase shifts. Let $\tilde{\psi}(\mathbf{x})$ denote the desired boundary-adapted version of $\psi(\mathbf{x})$. Since $\tilde{\psi}(\mathbf{x})$ vanishes on the boundary of the wedge, it can be extended to a fictitious wavefunction living in the whole plane by reflecting antisymmetrically across either boundary. To obtain $\tilde{\psi}(\mathbf{x})$, we let R_1 denote reflection with respect to one of the lines bounding the wedge and R_2 reflection with respect to the other line. We would like to antisymmetrize $\psi(\mathbf{x})$ with respect to both of these reflections. The projection operator $(1/4)(1-R_1)(1-R_2)$ does not work, however, because R_1 and R_2 do not commute. Instead we must resort to the following group-theoretical construction. Let R_3 denote the reflection with respect to the line that passes through the vertex of the wedge and meets the two edges of wedge at a 60° angle. The product R_1R_2 of the two reflections R_1 and R_2 is a rotation through 120° centered on the vertex, and R_2R_1 is the opposite rotation. Thus, the set $1, R_1, R_2, R_3, R_1R_2, R_2R_1$ forms a representation of the dihedral group C_3. It is now easy to see that $\tilde{\psi}(\mathbf{x})$ transforms under the one-dimensional representation of C_3 that assigns a character of -1 to the reflections and 1 to the rotations. Put another way, the problem of going from $\psi(\mathbf{x})$ to $\tilde{\psi}(\mathbf{x})$ is that of projecting onto this irreducible representation of C_3. Formally, this transformation is expressed as:[47]

$$\tilde{\psi}(\mathbf{x}) = \frac{1}{\sqrt{6}} \sum_{A \in C_3} \chi(A) A \psi(\mathbf{x}). \tag{5.3}$$

Here, A denotes the group elements $1, R_1, R_2, R_3, R_1R_2$ and R_2R_1, and the character is given by $\chi(R_1) = \chi(R_2) = \chi(R_3) = -1$ and $\chi(1) = \chi(R_1R_2) = \chi(R_2R_1) = 1$. The normalization factor of $1/\sqrt{6}$ is chosen to ensure that the two-point correlation function gives the free-space result far away from the wall. If we then restrict $\tilde{\psi}(\mathbf{x})$ to the wedge-shaped region, we obtain the required boundary-adapted sum of plane waves.

Now that we have an explicit expression for $\tilde{\psi}(\mathbf{x})$ we can use it to calculate the two-point correlation function $C(\mathbf{x}, \mathbf{x}+\mathbf{r}) = \langle \tilde{\psi}(\mathbf{x}) \bar{\tilde{\psi}}(\mathbf{x}+\mathbf{r}) \rangle$. The correlation function is a sum of thirty-six terms of the form

$$\begin{aligned}
\langle \chi(A) A\psi(\mathbf{x}) \chi(B) B\bar{\psi}(\mathbf{x}+\mathbf{r}) \rangle &= \chi(A)\chi(B) \int d\theta e^{-i\mathbf{k}_\theta \cdot (A\mathbf{x} - B\mathbf{x}) + i\mathbf{k}_\theta \cdot B\mathbf{r}} && (5.4) \\
&= \chi(A)\chi(B) \int d\theta e^{ik\rho \cos(\theta - \theta_0)} && (5.5) \\
&= \chi(A)\chi(B) J_0(k\rho) && (5.6)
\end{aligned}$$

Here $\rho = |A\mathbf{x} - B(\mathbf{x}+\mathbf{r})|$, that is, the distance from $\mathbf{x}+\mathbf{r}$ to $B^{-1}A\mathbf{x}$. The correlation function becomes

$$\begin{aligned}
C(\mathbf{x}, \mathbf{x}+\mathbf{r}) &= \frac{1}{6} \sum_{A,B \in C_3} \chi(A)\chi(B) J_0(k\rho_{B^{-1}A}) && (5.7) \\
&= \sum_{C \in C_3} \chi(C) J_0(k\rho_{C^{-1}}) && (5.8) \\
&= J_0(kr) - J_0(k\rho_{R_1}) - J_0(k\rho_{R_2}) - J_0(k\rho_{R_3}) + J_0(k\rho_{R_1 R_2}) + J_0(k\rho_{R_2 R_1}) && (5.9)
\end{aligned}$$

In the second line, we replaced B by AC. The sum over A then becomes trivial, since $\chi(A)\chi(B) = \chi(A)\chi(A)\chi(C) = \chi(C)$. In the last line ρ_A denotes the distance from $\mathbf{x}+\mathbf{r}$ to $A\mathbf{x}$.

This formula predicts that the two-point correlation function should display the interference of Bessel functions centered at all the points given by applying the group transformations on $\mathbf{x}$. Far from the boundary, Equation 5.7 reduces to the single Bessel function $J_0(kr)$, the value that it would have if no boundary were present.

However, the interference is pronounced near the boundary, and more especially near the vertex of the wedge.

5.3.2 the rectangular corridor

In the case of the rectangular corridor, the back wall and the semi-infinite walls need to be handled separately. The wavefunction at $\mathbf{x}$ in the $x < 0$ half-plane is obtained by reflecting about the y-axis. To extend the wavefunction in the y direction, we reflect it with respect to the wall at $y = a/2$. By repeating this process for all $y = (1 + 2m)a/2$ where $m = \{..., -1, 0, 1, ...\}$, the whole plane is tiled with positive or negative copies of $\psi(\mathbf{x})$.

Mathematically, the process by which $\tilde{\psi}(\mathbf{x})$ is obtained is as follows. The initial billiard is placed on an infinitely long cylinder of circumference $2an$. Our initial x-axis is now parallel to the axis of the cylinder, whereas the y-axis is wrapped around the cylinder and truncated at $y = (1 \pm 2n)a/2$. The wavefunction is first reflected across the y-axis. Therefore the antisymmetrization in the x-direction transforms as a one-dimensional representation of the reflection group $\mathbf{Z_2}$. Rotations by multiples of $2a$ should give back the wavefunction, while reflections about any of the lines parallel to the x-axis give its negative version. We thus obtain a representation of the dihedral group C_n. It is now clear that on the cylinder, $\tilde{\psi}(\mathbf{x})$ transforms under the one-dimensional representation of $C_n \otimes \mathbf{Z_2}$ that assigns a character of -1 for reflections and 1 for rotations. This time the transformation is given by as

$$\tilde{\psi}_n(\mathbf{x}) = \frac{1}{\sqrt{4n}} \sum_{A \in C_n \otimes \mathbf{Z_2}} \chi(A) A \psi(\mathbf{x}). \tag{5.10}$$

As in the case of the wedge, the normalization factor is found by requiring that the correlation function give $J_0(k\rho)$ far away from the wall.

The correlation function is given by:

$$
\begin{aligned}
C(\mathbf{x}, \mathbf{x}+\mathbf{r}) &= \lim_{n\to\infty} \frac{1}{4n} \sum_{A,B \in C_n \otimes \mathbf{Z_2}} \chi(A)\chi(B) J_0(k\rho_{B^{-1}A}) && (5.11) \\
&= \lim_{n\to\infty} \sum_{C \in C_n \otimes \mathbf{Z_2}} \chi(C) J_0(k\rho_{C^{-1}}). && (5.12)
\end{aligned}
$$

However, $J_0(k\rho_{C^{-1}}) \to 1/\sqrt{k\rho_{C^{-1}}}$ for large $\rho_{C^{-1}}$.' Hence, only the Bessel functions centered at nearby points contribute, and the correlation function remains finite as we take the $n \to \infty$ limit.

5.4 Numerical results

Here we apply the theory to check further the properties of random waves in billiard systems. There are some obvious and some more subtle modifications of random wave behavior known in closed chaotic billiards. The wavefunction must vanish on the boundary, and scarring affects some states in a nonrandom way [25]. The theory given here suggests new correlations which ought to be checked in chaotic systems. As we incorporate more about a specific billiard geometry into our correlation functions, we are probing the properties of waves which are "as random as possible" within the constraints, such as a wedge boundary being present. In checking the numerics of a billiard such as the cone or stadium, we are really asking whether the eigenstates are truly random but for the constraint of interest, say a wedge boundary. Naturally this cannot be strictly true, since there are more constraints that we haven't included. At the end of this strategy comes a tautology: if, in a closed billiard we incorporate *all* the constraints, we have only the eigenstates left, as the *only* waves which are

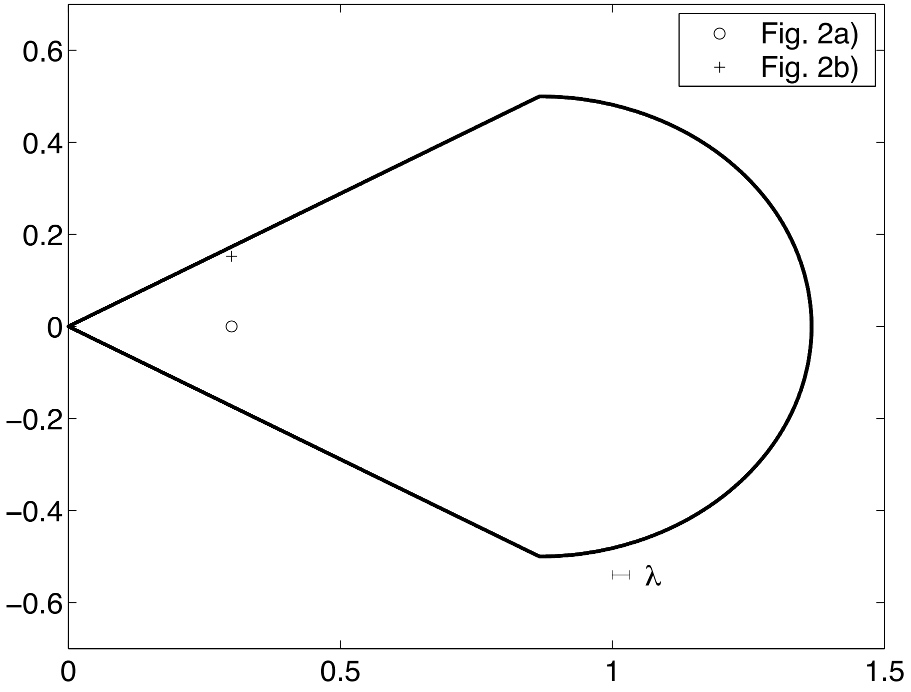

Figure 5.1: The cone billiard

consistent with all the constraints!

5.4.1 The wedge

To validate our expressions for $\tilde{\psi}(\mathbf{x})$ and $C(\mathbf{x}, \mathbf{x}+\mathbf{r})$, we generated an ensemble of 500 eigenstates near $k = 200$ for a 60° wedge which has been closed off by a semicircle; see Figure 5.1. The eigenstates were found using the Boundary Integral Method. Our cone-shaped billiard has a circle diameter equal to 1, which is about 32 wavelengths across. The Poincare section indicates that this billiard is chaotic.

In Figure 5.2, we show $C(\mathbf{x}, \mathbf{x}+\mathbf{r})$ for (a) $\mathbf{x}$ on the symmetry line through the center of the billiard, and (b) for $\mathbf{x}$ placed within a wavelength of one of the edges. Both Figures 5.2(a) and 5.2(b) display the expected interference, but the later is especially pronounced in Figure 5.2(b). Note that since $\mathbf{x}$ is on the symmetry line, only even states contribute to Figure 5.2(a).

For comparison, Figure 5.3 displays the theoretical predictions for the two-point correlation functions of Figure 5.2. Both plots are in good agreement with their numerical equivalent. In particular, the interference pattern of Figure 5.2b is reproduced in Figure 5.3b. However, the angular oscillations are much more pronounced in the theoretical plots, suggesting that an unaccounted-for smoothing process is at work in the numerical experiment. We compared the error quantitatively using

$$\frac{\int d^2r |C_{\mathrm{num}}(\mathbf{x},\mathbf{x}+\mathbf{r}) - C_{\mathrm{th}}(\mathbf{x},\mathbf{x}+\mathbf{r})|^2}{\int d^2r C_{\mathrm{th}}(\mathbf{x},\mathbf{x}+\mathbf{r})^2}. \tag{5.13}$$

We obtained 0.52 for Figure 5.2a and 0.15 for Figure 5.2b. The discrepancy in the predicted and experimental values is expected due to the difference in the angular nodes, and appears to be more pronounced far away from the billiard walls.

In Figure 5.4, we take the radial average of the correlation functions of Figure 5.2. As was found by Li and Robnik,[29] Figure 5.4a resembles the Bessel function $J_0(kr)$. This should be the case whenever boundary effects contribute equally from all sides. Since $\mathbf{x}$ in Figure 5.4b lies very close to the boundary, the radial average is shifted from the $J_0(kr)$ curve.

5.4.2 The rectangular corridor

Once again, we took an ensemble of 500 eigenstates near $k = 200$, this time for a quarter stadium with a endcap radius of $R = 0.6$ and straight length $l = 1.2$ (about 20 wavelengths wide); see Figure 5.5. The numerical correlation function is shown in Figure 5.6 for $\mathbf{x}$ (a) on the symmetry line through the center of the billiard, (b)

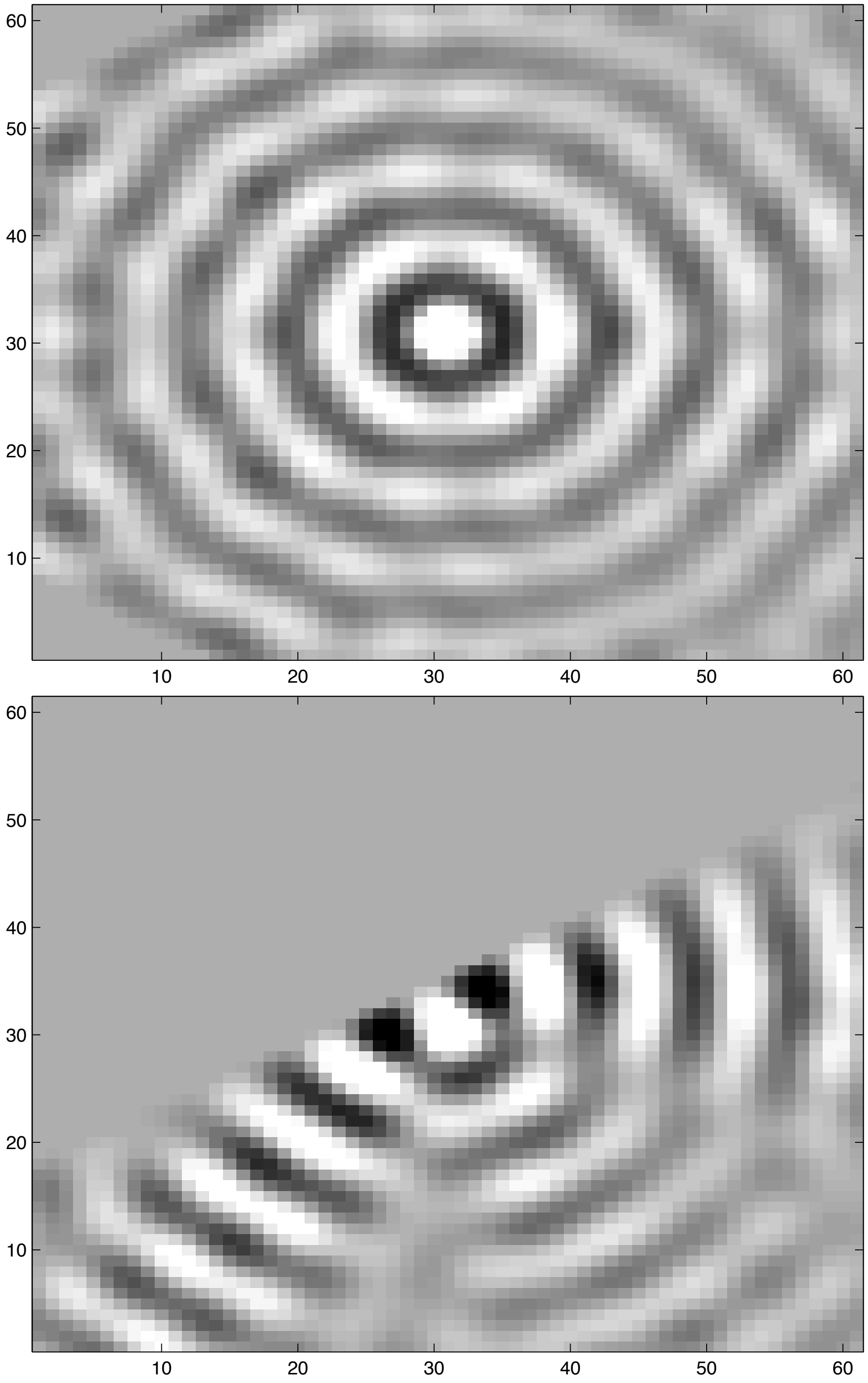

Figure 5.2: (a) Experimental correlation function for $\mathbf{x} = (0.3, 0)$. The grid area is 0.0166, or about 8 wavelengths across in the x and y directions. (b) Same as (a) for $\mathbf{x} = (0.3, 0.153)$.

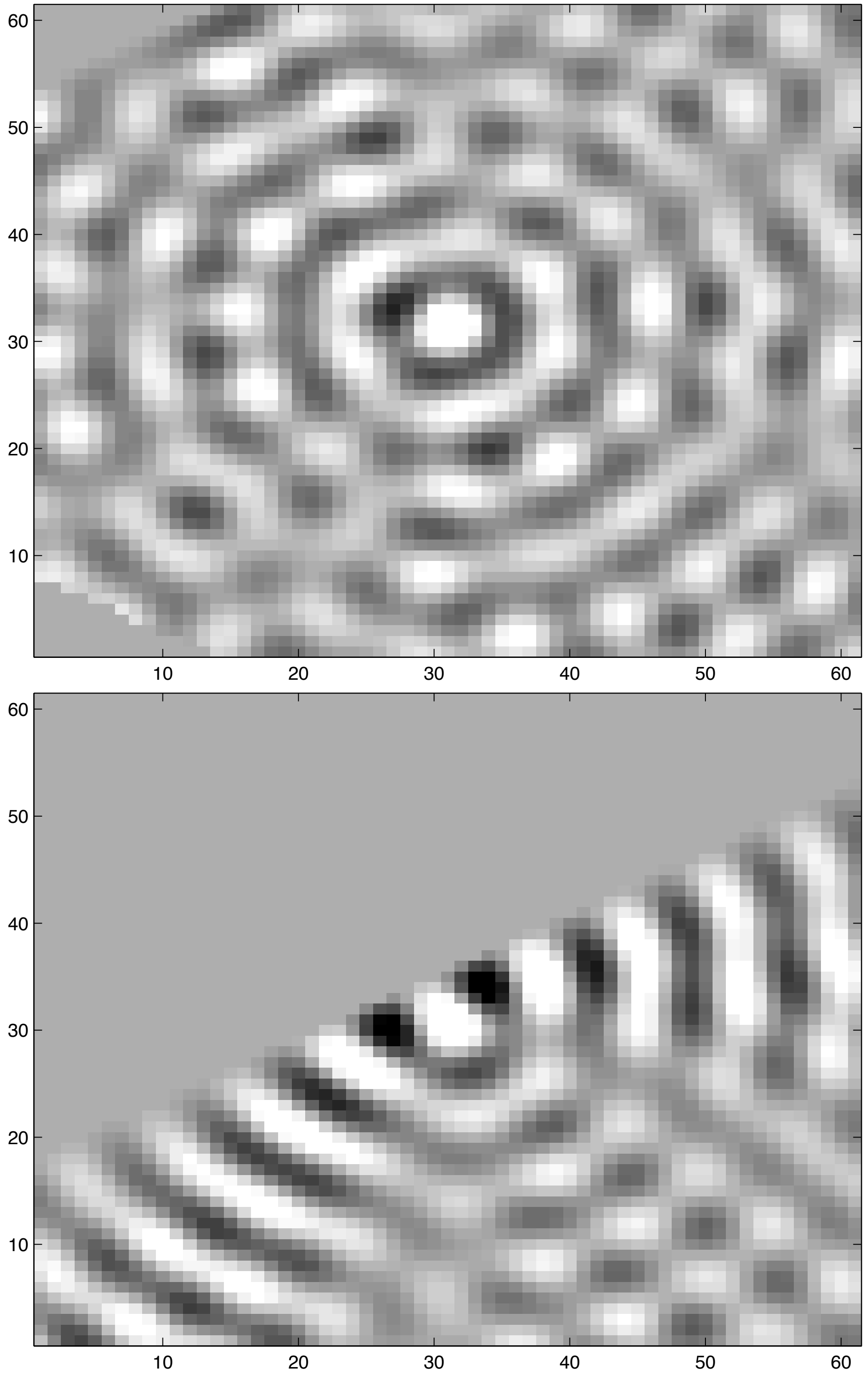

Figure 5.3: **top:** (a) Theoretical correlation function for $\mathbf{x} = (0.3, 0)$. **bottom:** (b)Same as (a) for $\mathbf{x} = (0.3, 0.153)$.

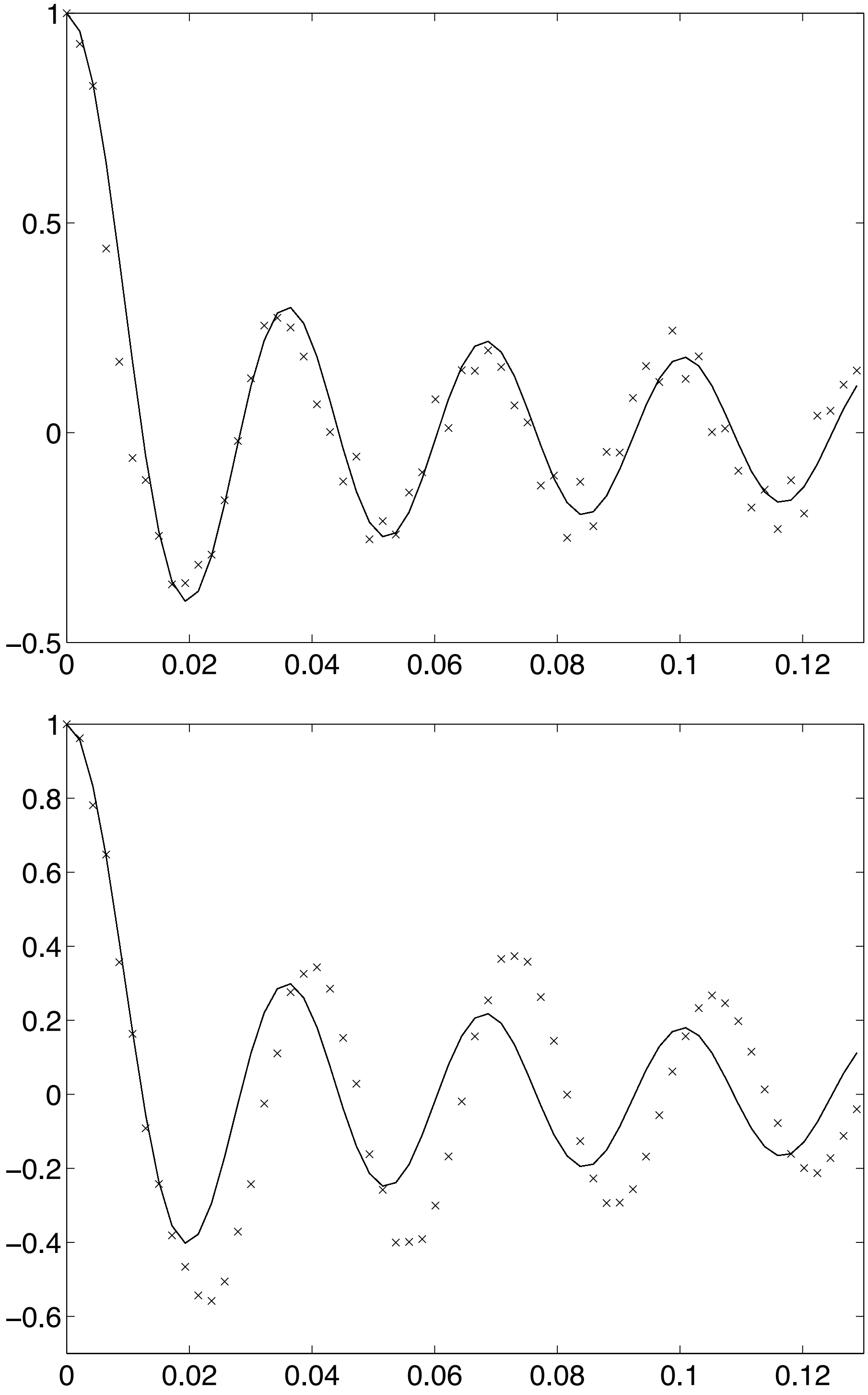

Figure 5.4: **top:**(a) Radial average of $\Psi(\mathbf{x}+\mathbf{r})$ for $\mathbf{x} = (0.3, 0)$. **bottom:**(b)Same as (a) for $\mathbf{x} = (0.3, 0.153)$.

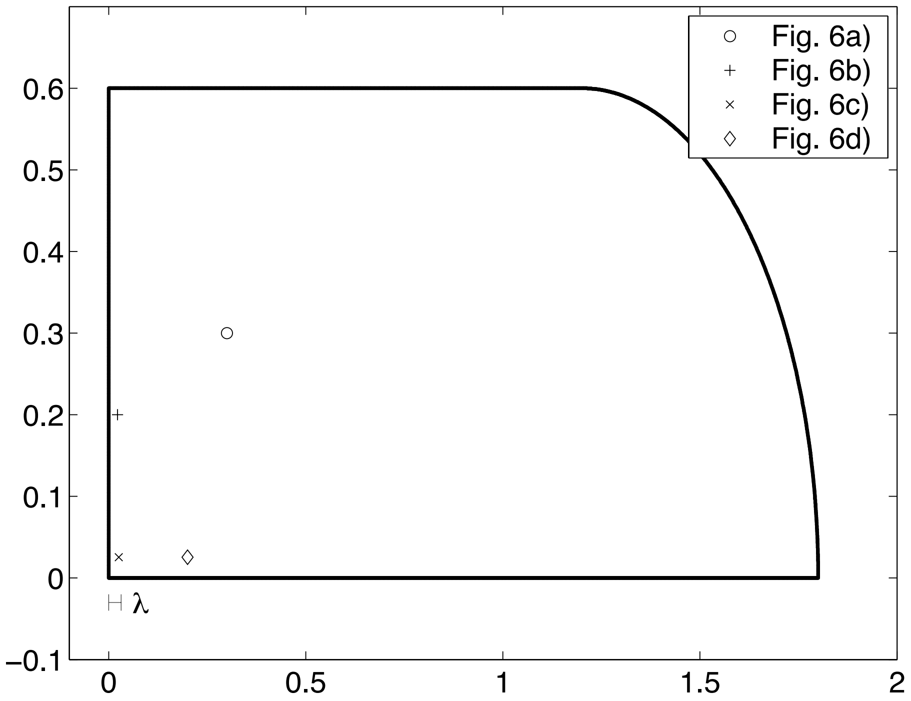

Figure 5.5: The stadium billiard

within 1 λ of the top wall, (c) within 1 λ of a corner and (d) within 1 λ of the back wall. As expected, only the Bessel functions which are less than a few wavelengths away contribute to $C(\mathbf{x}, \mathbf{x}+\mathbf{r})$.

The numerical correlation function of Figure 5.6 was compared to the theoretical prediction of Figure 5.7 using Equation 5.13. Here only the first few terms were kept in $C_{\text{th}}(\mathbf{x}, \mathbf{x}+\mathbf{r})$. We obtain 0.55 for Figure 5.6a, 0.23 for Figure 5.6b, 0.03 for Figure 5.6c and 0.24 for Figure 5.6d, in agreement with our results for the cone billiard.

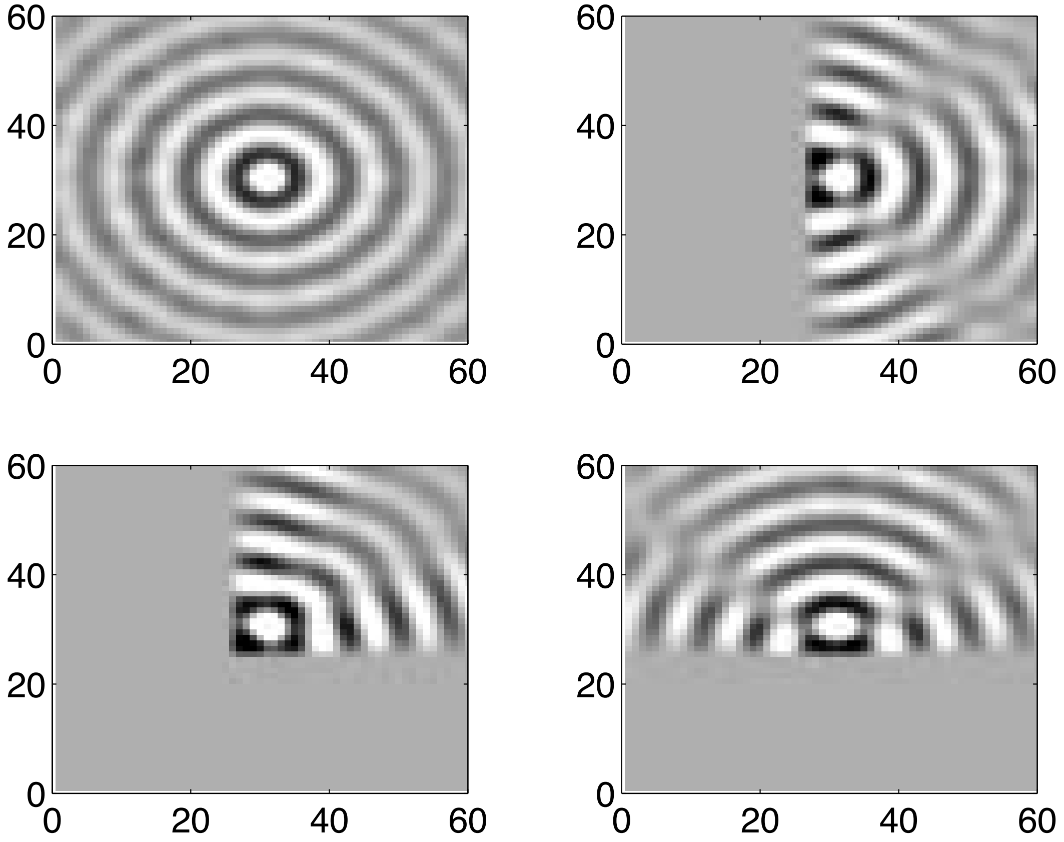

Figure 5.6: **top-left:** (a) Experimental correlation function for $\mathbf{x} = (0.3, 0.3)$. The grid area is 0.0195, or about 8 wavelengths across in the x and y directions.
top-right: (b)Same as (a) for $\mathbf{x} = (0.0223, 0.2)$.
bottom-left: (c)Same as (a) for $\mathbf{x} = (0.0255, 0.0255)$.
bottom-right: (d)Same as (a) for $\mathbf{x} = (0.2, 0.0255)$.

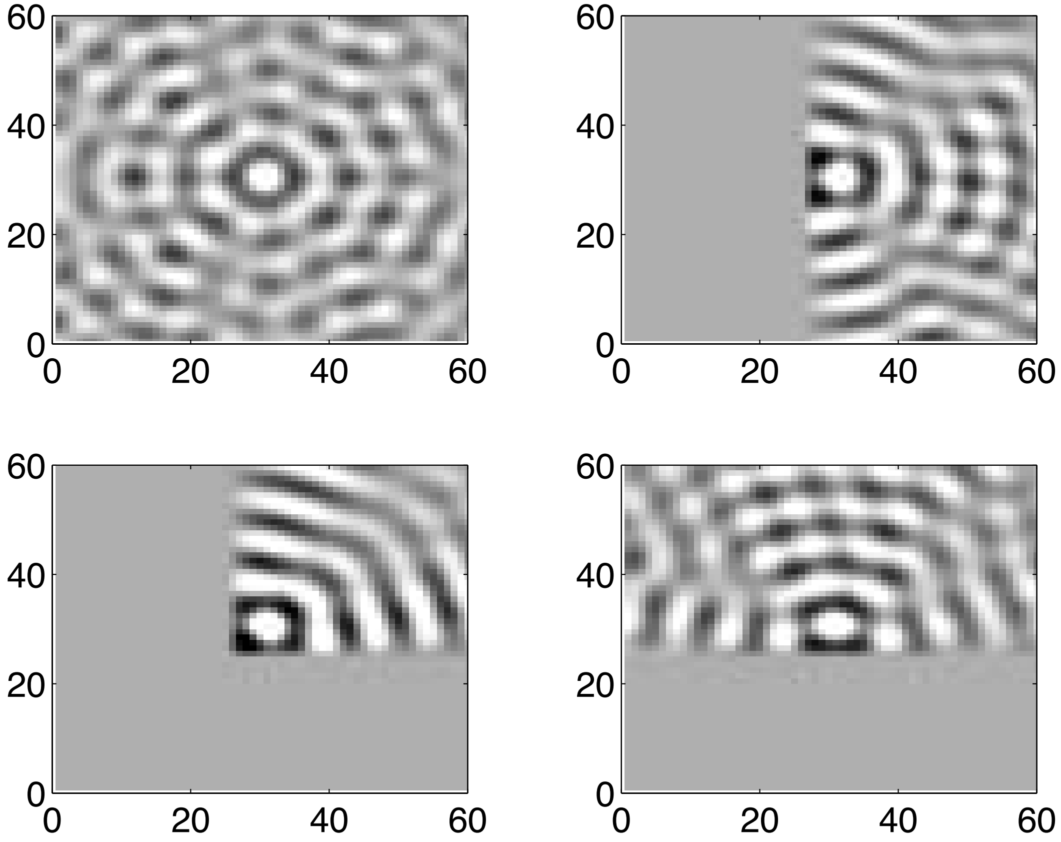

Figure 5.7: **top-left:** (a)Theoretical correlation function for $\mathbf{x} = (0.3, 0.3)$.
top-right: (b)Same as (a) for $\mathbf{x} = (0.0223, 0.2)$.
bottom-left: (c)Same as (a) for $\mathbf{x} = (0.0255, 0.0255)$.
bottom-right: (d)Same as (a) for $\mathbf{x} = (0.2, 0.0255)$.

5.5 Conclusion

We have successfully extended the boundary-adapted Gaussian wave model to a wedge-shaped region with opening angle 60°. Our technique is readily generalized to any opening angle of the form π/n for n integer; one merely replaces the group elements of C_3 with those of the dihedral group C_n. We also solved the case of the semi-infinite rectangular corridor. It is our hope that these results will stimulate more work on boundary effects in arbitrarily shaped billiards; in particular, it would be desirable to compare our exact group-theoretical formula for the correlation function with the semiclassical expression of Hortikar and Srednicki [24].

Chapter 6

Localization and Scars

In many respects, the wavefunctions of chaotic systems agree well with the random pattern of waves described by Berry's conjecture. McDonald [33] and McDonald and Kaufman [34] were the first to observe this behavior numerically for the eigenstates of the stadium billiard. The authors discovered that the nodal lines followed a seemingly random pattern for most eigenstates. Furthermore, the wavefunction intensity distribution was shown to have Gaussian statistics.

As for the eigenvalues of chaotic systems, it was predicted that their level spacing distribution should resemble those of random matrices [9]. That is, the distribution of level spacings $s = A/(2\pi)(E_i - E_{i-1})$ should be approximately

$$P(s) = (\pi/2)s \exp\left(-\pi s/4\right) \tag{6.1}$$

By comparison, the level spacings of integrable systems follow a Poisson distribution

$$P(s) = \exp\left(-s\right) \tag{6.2}$$

McDonald and Kaufman, in their seminal paper, were the first to study the level distributions, and found that they indeed agreed with the predictions of random matrix theory (RMT).

Scars were discovered by Heller [21] shortly after the first numerical billiards experiments were performed. The linear theory of scars, as originally formulated in that paper may be understood as follows. A Gaussian wavepacket $|q_0, p_0\rangle$ is placed on a periodic orbit in phase space. After a time equal to the period T, the wavepacket returns to its starting point. During that time, the coherent state will have spread, and its amplitude will be reduced by a factor of $\exp(-\lambda T/2)$, where λ is the Lyapunov exponent of the orbit. Thus, the autocorrelation function

$$A(t) = \langle q_t, p_t | q_0, p_0 \rangle \tag{6.3}$$

will have peaks at times which are integer multiples of the period. In order to understand the consequences of these peaks for the eigenstates, the spectrum $S(E)$ is obtained by taking the the Fourier transform of $A(t)$. The peaks of decaying amplitude in the autocorrelation function generate an envelope in the spectrum of width λ and spacing $2\pi/T$. Thus, the eigenstates will be localized under bumps of width λ. As a result, states at those energies will have statistically enhanced amplitudes along the periodic orbit (scar), while those that fall in the trough will have an lower density than the average (antiscars). The linear theory says nothing however, about how the overdensity is distributed among states [26], only that some states will be scarred and some antiscarred.

It is interesting that the short-time envelope depends only on the Lyapunov exponent of the orbit. As a consequence, only the shortest periodic orbits which have $\lambda T/2 < 1$ significantly contribute to scarring. Furthermore, if for instance, we study a system with a tunable Lyapunov exponent like the pseudosphere, it is possible to control the amount of scarring by changing the dimensions of the billiard that we choose, and thus the average Lyapunov exponents of the orbits.

Several measures exist to detect localization and scars. Kaplan [25] computed the wavefunction intensity distributions in phase space in the generalized three-strip Baker's map, and found them to have increased small and large tails as compared to RMT. It is important that measures of scarring be taken in phase space rather than in configuration space, since scars may not be evident in the later.

It is also useful to compute the second moment of the overdensity for each of the eigenstates, the IPR, defined as [12]

$$\mathcal{I}_n = \frac{\frac{1}{J}\sum_{j=1}^{J} |\langle q_j, p_j|n\rangle|^4 \; {}^{2}}{\left(\frac{1}{J}\sum_{j=1}^{J} |\langle q_j, p_j|n\rangle\right)} \tag{6.4}$$

where $|n>$ denotes the eigenstates, and the j's label a grid in phase space. The RMT predicts a background of 2 for the IPR of complex eigenstates and and 3 for real ones. Every form of localization will increase the value of the IPR. Thus, an IPR greater than 2 or 3 proves that some form of localization is present, but does not provide the mechanism at work.

The local inverse participation ratio (LIPR) is the second moment of the intensity distribution for points in phase space. More precisely, for N states, [12]

$$\mathcal{L}(q,p) = \frac{\frac{1}{N}\sum_{n=1}^{N} |<q,p|n>|^4}{\left(\frac{1}{N}\sum_{n=1}^{N} |<q,p|n>|^2\right)^2} \tag{6.5}$$

Wherever localization is present, the LIPR will be greater than the background value of 2 or 3. Thus, for instance, the LIPR should be greater than the background on short periodic orbits if scarring is present.

It is possible to determine directly the amount of localization due to scarring. For this purpose, one finds the fraction of phase space over which recurrences occur, and computes the strength of the overlaps in those regions. More precisely, if O_t is the strength of the classical overlap of the wavepacket with itself after time T, Bies and coworkers [12] found that the fraction of the LIPR due to scars is given by

$$LIPR_{scars} = (2 \text{ or } 3) IPR_{short-time}(1 + 2 \sum_{t=T,2T,\ldots} (O_t - 1/N)) \tag{6.6}$$

Here N is the number of phase space cells explored by the mixing time, and $IPR_{short-time}$ is the IPR of the short-time envelope, i. e.

$$IPR_{short-time} = \langle S(E)^2 \rangle_n / \langle S(E) \rangle_n^2. \tag{6.7}$$

where $\langle\rangle_n$ denotes the average over eigenstates.

The properties of billiards on surfaces of constant curvature remain a very interesting and little explored venue in which to study quantum chaos. Some work has been done on the properties of triangles on the sphere (see [41, 42]). Aurich and Steiner [1, 2, 3], and Balazs and Voros [4] published several papers on the properties of chaotic eigenstates of hyperbolic octagons on the pseudosphere.

The pseudosphere is a particularly interesting system in which to study chaos, because the dynamics on the surface is chaotic even in the absence of any walls. In particular, the presence of scarring has long been debated[3]. In Chapter 7, we use all the measures described earlier in this chapter to understand the problem of localization and particularly scarring on the pseudosphere. We choose triangular billiards whose boundaries are geodesics, in order to minimize the effect of the boundaries on the dynamics. The Poincare sections show that these billiards are fully chaotic. Our results demonstrate that scarring is indeed present on the pseudosphere, though it does not account for all the localization that we see. The remaining localization is attributed to diffraction effects in the corners. We also study generic triangles with non-geodesic walls, and find that it the boundaries focus some of the trajectories and thus counteract the effect of the strong chaos induced by the surface curvature.

Chapter 7

Localization on the pseudosphere

7.1 abstract

We study the curvature dependence of localization using triangular billiards on the pseudosphere. While localization in excess of that predicted by random matrix theory is difficult to detect in these billiards owing to their strong chaos, we succeed in doing so by employing sensitive phase-space dependent measures based on overlaps of eigenstates with coherent states. The smoothed local density of states is shown to have the modulation expected from scarring, which allows us to associate this localization with scarring along short periodic orbits. However, the short-time classical dynamics responsible for scarring does not account for all of the localization seen. The excess over scarring must be attributed to hard quantum effects such as diffraction in the corners. We also show that boundary focusing effect can lead to a curvature-dependent localization which originates in the appearance of quasi-integrable motion.

7.2 Introduction

The pseudosphere is a natural system to study quantum chaos, since the curvature itself forces all geodesics to diverge from each other. In this paper, we determine the effects of constant negative surface curvature on localization in quantum billiards. Since the system is chaotic even in the absence of the boundary, one intuitively expects the curvature to reduce the amount of localization in such systems as compared to equivalent planar billiards.

Berry [6] conjectured that the wavefunction of chaotic billiards should look like a random superposition of plane waves. However, even in such random superpositions, some localization creeps in in the form of linear structures (hereafter called scarlets) along the local direction of the momentum O'Connor *et al.* [36]. These structures were explained as follows. The authors studied the overlap of a coherent state with random waves at fixed energy. They showed that overlap remains constant for short times. If the coherent state is initially placed on a region of high amplitude, it will remain on a region of high amplitude for a while, thus explaining the linear structures. Scarlets were also found to be present on negatively curved surfaces (see [3]). In ths paper, we focus on curvature effects beyond those induced by the randomness of the basis coefficients, such as scars or the bouncing ball modes as seen for instance in the stadium billiard.

In particular, the problem of scarring on the pseudosphere has been studied by Aurich and Steiner [3], who investigated the eigenstates of hyperbolic octagons on the Poincare disk. These authors studied the autocorrelation function of a coherent state that was initially placed on a periodic orbit. Scar strength is of the order of

$1/\lambda$, where λ is the Lyapunov exponent of the system [21]. For the periodic orbits of hyperbolic octagons on the pseudosphere, $\lambda = 2\sqrt{E - 1/4}$. Since λ is large, the scar strength was claimed to be below the level of the RMT fluctuations. Furthermore, the energy spectrum was distributed among a large set of eigenstates. As a result, the authors concluded that the increase in amplitude along the periodic orbit was not statistically significant for individual eigenstates.

However, as was pointed out by Kaplan and Heller [26], the scar phenomenon is a statistical effect. They define a scar as follows: "A quantum eigenstate of a classically chaotic system has a scar if its density on the classical invariant manifolds near the periodic orbit is enhanced over the statistically expected density." It is true that scaring is more pronounced in the case where the overdensity of the spectral envelope is shared by very few eigenstates (described as 'totalitarian' filling by those authors). Even if, however, the latter is distributed equally over a large number of eigenstates ('egalitarian' filling), the total density enhancement of each state will still be statistically significant (of order $1/\lambda$) compared to the RMT expectation. Egalitarian filling will not be evident in coordinate space. The enhancement being a statistical effect, it can not be seen in individual eigenstates, but arises upon averaging the intensities of a group of nearby states. This must be kept in mind when comparing with a group of randomly generated states. The existence of a single random state with a large intensity does not show that scarring is absent because the relevant quantity is the average intensity over a group of nearby states. In this light, Figure 8 of [3] can be interpreted as demonstrating the presence of scarring in the hyperbolic octagon at high energy, contrary to the authors' conclusion.

Several measures are available to describe localization. Kaplan [25] looked at the distribution of wavefunction intensities of the Baker's map, and compared it to a random matrix theory (RMT) predictions. The low and high tails of the distribution were found to differ significantly from the RMT generated distribution. The inverse participation ratio (IPR) gives a measure of the the amount of localization in phase space. For complex wavefunctions, RMT predicts a value of 2 for the IPR. Bies *et al.* [12] found that this value was significantly increased in the stadium compared to RMT,even after the bouncing ball modes were removed. Finally, the local inverse participation ratio (LIPR) shows the distribution of localization among points in phase space. Bies *et al.* [12] used this measure in the stadium to understand which part of the localization was due to scars, and which to bouncing ball modes.

We look at the intensity statistics, IPR and LIPR of various billiards on the pseudosphere for coherent states in the interior and on the boundary. we studied two triangles with geodesic boundaries which differ only by their length in the radial direction on the pseudosphere, and thus the amount of curvature that is seen by the wavefunctions. The boundaries being 'straight', they are not expected to focus the wavefunction. Using this method, we determine the surface and boundary curvature contribution to these various measures. The fraction of the localization which is associated with scarring is found by examining the properties of the smoothed local density of states.

We find localization in excess of RMT in both large and small geodesic triangles at high and low k. Some of this localization is indeed due to scarring, while the remainder appears to be a hard quantum effect originating in eigenstates that are localized at the corners. This latter effect cannot be explained by short-time semiclassical dynamics. In addition to localization in the corners, many of the states in the small geodesic triangle appear to remember the fact that this billiard is nearly integrable and display a quasi-integrable type of localization which coexists with the localization due to the scarring mechanism. This makes it more difficult, but not impossible to identify scarring.

We also address the problem of focusing by the boundaries. In flat space, the generic billiard boundary has mixed phase space. On the pseudosphere, we expect some boundaries to focus the trajectories in a similar way, thereby counteracting the effect of the curvature-induced divergence of the trajectories. As a trivial example, the classical dynamics of annuli centered around the origin is integrable. Thus, the boundary fully counteracts the effects of the surface curvature. We study similar generic triangular shapes of different sizes. We notice such a focusing effect for these shapes, and find it to be strongly curvature dependent. Surprisingly, the focusing was increased by the intrinsic negative curvature of the boundary.

7.3 Numerical Method

The plane wave decomposition method (PWDM) [21, 22] is widely used as a means to solve for the eigenvalues and eigenstates of Helmholtz equation in the plane. The eigenstates in this papers were found through an equivalent method for the pseudosphere, which is due to Schmit [40]. We give a brief review of it in this section.

The Helmholtz equation on the pseudosphere is given by

$$(\nabla^2 + E)\Psi = 0 \tag{7.1}$$

where

$$\nabla^2 = \frac{1}{\sinh\tau}\frac{\partial}{\partial\tau}\left(\sinh\tau\frac{\partial}{\partial\tau}\right) + \frac{1}{\sinh^2\tau}\frac{\partial^2}{\partial\phi^2}. \tag{7.2}$$

Here τ is the radial coordinate away from the center of the hyperboloid, and ϕ the angle around its center. For a review of the pseudosphere, see appendix A and the more detailed description given by Balazs and Voros[4]. Using $r \equiv tanh(\tau/2)$, Equation 7.1 can be separated into radial and angular components, yielding solutions $F_{\mu\nu}$ of the form

$$F_{\mu\nu}(r,\phi) = C_\mu P_{\mu\nu}(r)\exp i\mu\phi \tag{7.3}$$

where $\nu = ik - 1/2$ and k is the wavevector, $k^2 = E$. A convenient normalization C_μ for the $P_{\mu\nu}$'s will be chosen later in this section.

For Dirichlet boundary conditions, we have the additional requirement that the solution satisfy $\Psi(\mathbf{r}(\mathbf{s})) = \mathbf{0}$ for all points s along the boundary. Since $F_{\mu\nu}(r)$ is a solution of the Helmholtz equation everywhere inside the billiard, any linear combination of it at fixed ν will also be a solution. Thus, the eigenstates are found by choosing a superposition of these functions such that the coefficients of the superposition satisfy the boundary conditions. That is, the eigenstates are of the form

$$\Psi(\mathbf{r}) = \sum_\mu \mathbf{a}_\mu \mathbf{F}_{\mu\nu}(\mathbf{r}). \tag{7.4}$$

We limit ourselves to billiards that are symmetric with respect to the line at $\phi = 0$, and to odd states. As a result, the factor of $\exp i\mu\phi$ in the basis functions may be changed to $\sin\mu\phi$. To insure convergence, Heller [21] found it necessary to set the wavefunction at a random point (r_i, ϕ_i) inside the billiard to be equal to 1. Thus, we obtain the following set of equations for the $a_m u$'s:

$$0 = \sum_{\mu=0}^{\infty} a_\mu C_m u P_{\mu\nu}(r(s)) \sin \mu\phi(s) \quad \text{for all s} \tag{7.5}$$

$$1 = \sum_{\mu=0}^{\infty} a_\mu C_m u P_{\mu\nu}(r_i) \sin \mu\phi_i \tag{7.6}$$

For each values of k, the a_μ's are found using singular value decomposition. Numerically, of course, the summation is limited to a finite number of basis vectors. Convenient values of the truncation are determined later on in this section. The wavefunction around the boundary is calculated on a grid of equally spaced points. As a consequence of these numerical limitations, the wavefunction will not be exactly equal to 0 on the boundary. However, at the eigenvalues, the wavefunction intensity will be minimized around the boundary. Thus, an eigenstate is found when the tension

$$\text{tension} \equiv \sum_{s} |\Psi(\mathbf{r}(\mathbf{s}))|^{\mathbf{2}} \tag{7.7}$$

is a minimum.

A search algorithm in k was used to find the minima of the tension. The Legendre functions are hard to compute directly for large ν's due to the slow convergence of their defining series. Schmit found a way to get around this problem for hyperbolic octagons centered at the origin. His method, which we describe below, is limited to integer values of μ. This subset is the correct one to use in the case of billiards enclosing the origin, since $\phi \rightarrow \phi + 2\pi$ must be single valued inside of the billiard. However, this is not necessarily the case for a general billiard. It is well known that the wavefunctions of billiards can not always be extended to the entire plane [20]. Thus, in the general case, μ may be any real number. The integer values of μ for

$\mu < \nu$ are the equivalent of plane waves $\exp i\vec{k} \cdot \vec{x}$ which are used for the PWDM on the plane. These are well behaved oscillatory functions. On the other hand, the remaining values of μ are oscillatory on a small region, after which they diverge rapidly. As is the case for the PWDM on flat surfaces, we found that the eigenstates of our simple billiards could be found using the 'plane wave' solutions alone.

Following Schmit, we fix r and solve at once for $F_{\mu\nu}(r)$ for all μ's. The starting point of the method is the recurrence relation

$$\begin{aligned} \sqrt{k^2 + (\mu^2 + 1/2)} C_\mu P_{\mu\nu}(r) &= (\mu + 1)\frac{1 + r^2}{r} C_\mu + 1 P_{\mu+1,\nu}(r) \qquad (7.8) \\ &- \sqrt{k^2 + (\mu^2 + 3/2)} C_\mu + 2 P_{\mu+2,\nu}(r) \qquad (7.9) \end{aligned}$$

where the C_μ's are fixed such that

$$C_\mu = (-1)^\mu \prod_{l=1}^{\mu} \frac{1}{\sqrt{k^2 + (l^2 - 1/2)}}. \tag{7.10}$$

With this normalization, the completeness relation for the $F_{\mu\nu}(r)$ is given by

$$\sum_{\mu=-\infty}^{\infty} C_\mu P^2_{\mu\nu}(r) = 1. \tag{7.11}$$

These two relations are enough to generate all the μ's below a given $\mu = \mu_{max}$. In order to use the recurrence relation, two consecutive values of $P^2_{\mu\nu}(r)$ are required. It can be shown that $C_\mu P_{\mu\nu}(r) \propto (kr/\mu)^\mu$, for $\mu > 2kr/(1 - r^2)$. Thus, if μ_{max} is large,

$$\begin{aligned} P_{\mu_{max}+2,\nu}(r) &= 0 \qquad (7.12) \\ P_{\mu_{max}+1,\nu}(r) &= \alpha \left(\frac{kr}{+1}\right)^{\mu_{max}+1} \qquad (7.13) \end{aligned}$$

for some value of α to be determined. The recurrence relation then gives all the $P_{\mu_{max}+2,\nu}(r)$ up to the normalization α. The value of α is determined by the completeness relation. We found a basis size of$\mu_{max} = 10 + 2k/(1 - r^2)$ to be sufficient for

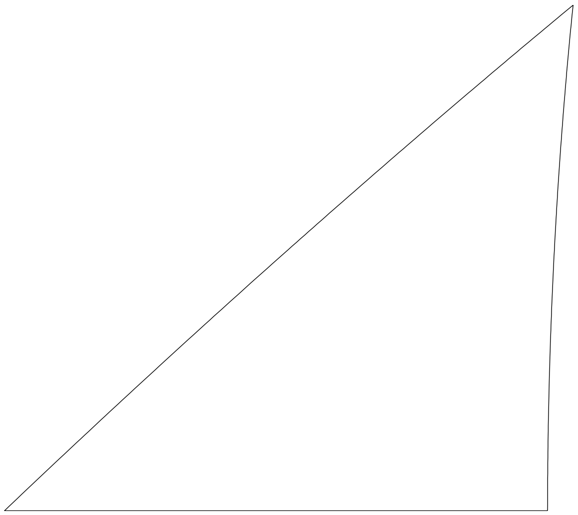

Figure 7.1a geodesic triangle

our purpose. For small r, the recurrence relation diverges, and this method can not be used directly. The straightforward application of this technique works well for the values we used, since we limited ourselves to billiards at inner radii of $\tau_{min} = 0.6$. The minima that we found by Schmit's method are quite sharp and easily distinguishable from the background.

A typical billiard is shown in Figure 7.1a. It consists of a triangle whose sides are geodesics. The first vertex is chosen to be $\tau_1 = 0.6, \phi_1 = 0$. The second vertex is taken to be $\tau_2 = 0.9, \phi_2 = (\tau_2 - \tau_1)/2\tau_1$. The third vertex is taken to be the intersection of the radial line at $\phi = 0$ with the geodesic from τ_2, ϕ_2 to $\tau_2, -\phi_2$. Thus, $\tau_3 = 0.85569$.

The quarter stadium billiard (with a straight side of length $L = 0.3$ and the radius of the endcap $R = 0.3$) was used to compare our values to the flat space equivalent. We looked at approximately 500 eigenstates around $k = 1000$.

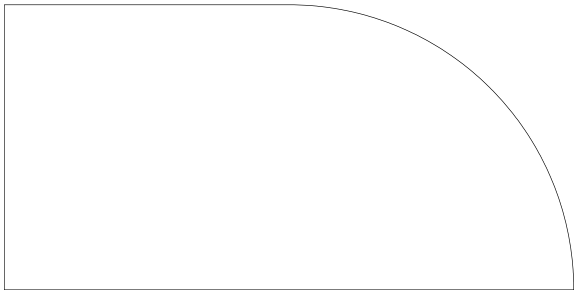

Figure 7.1b stadium billiard

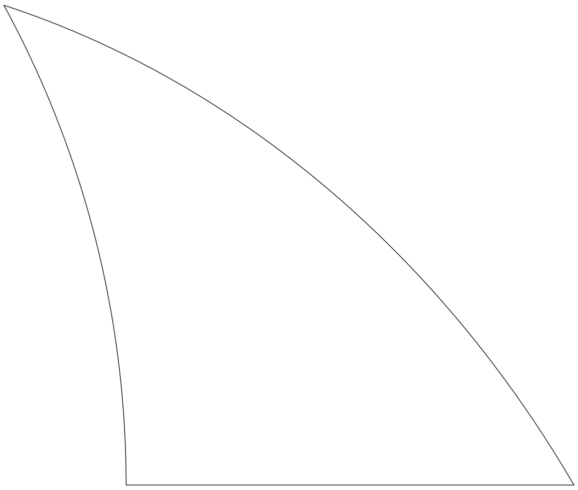

Figure 7.1c non-geodesic triangle

7.4 eigenstates

In Figure 7.2, we show a sample of eigenstates for the geodesic triangles. We notice that the eigenstates of the small geodesic triangle around $k = 500$ look regular. The reason for this is that for large wavelengths, the geodesic triangle is almost a flat-space right triangle with two equal sides. The wavefunction is not sensitive enough to detect the small variations in the wall which make the system chaotic classically. At larger k's, the eigenstates look chaotic, as expected. The large triangle states look fully chaotic.

Furthermore, at the lower values of k, the small geodesic triangle has overdense linear structures that do not fall on short periodic orbit as scars would. These overdensities can again be attributed to the quasi-integrability of the wavefunction at those energies. The wavefunction remembers its integrability. The classical trajectory associated with the overdense structure survives from the integrable version of the triangle in flat space.

7.5 classical dynamics

We found the Lyapunov exponents on each of our billiards to determine the effects of curvature. We expect that the Lyapunov exponent will increase with curvature, because there will be more divergence of nearby trajectories while crossing the larger billiard. This is indeed what happens; the Lyapunov exponent increases from 0.213 to 0253 for the non-geodesic triangle and from 1.857 to 2.961 for the geodesic triangle.

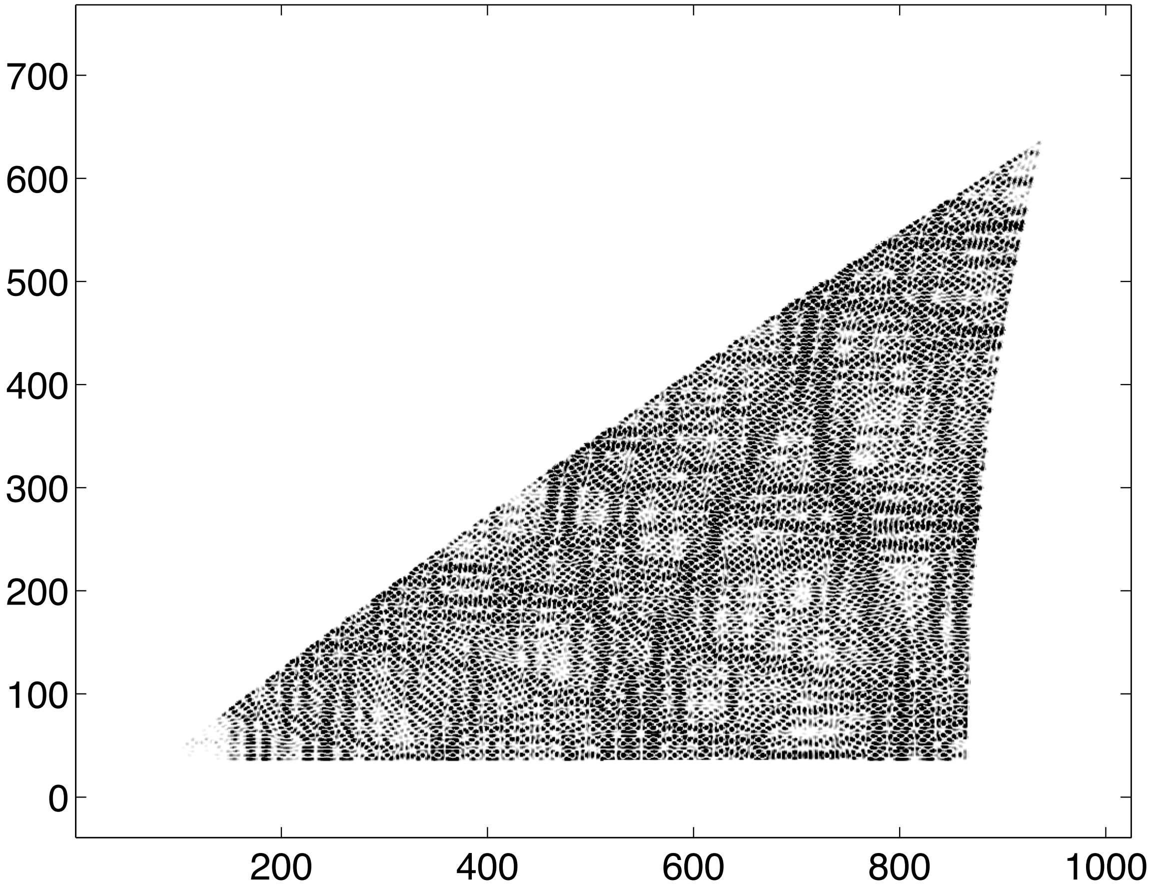

Figure 7.2a small triangle eigenstate at k=2044.77

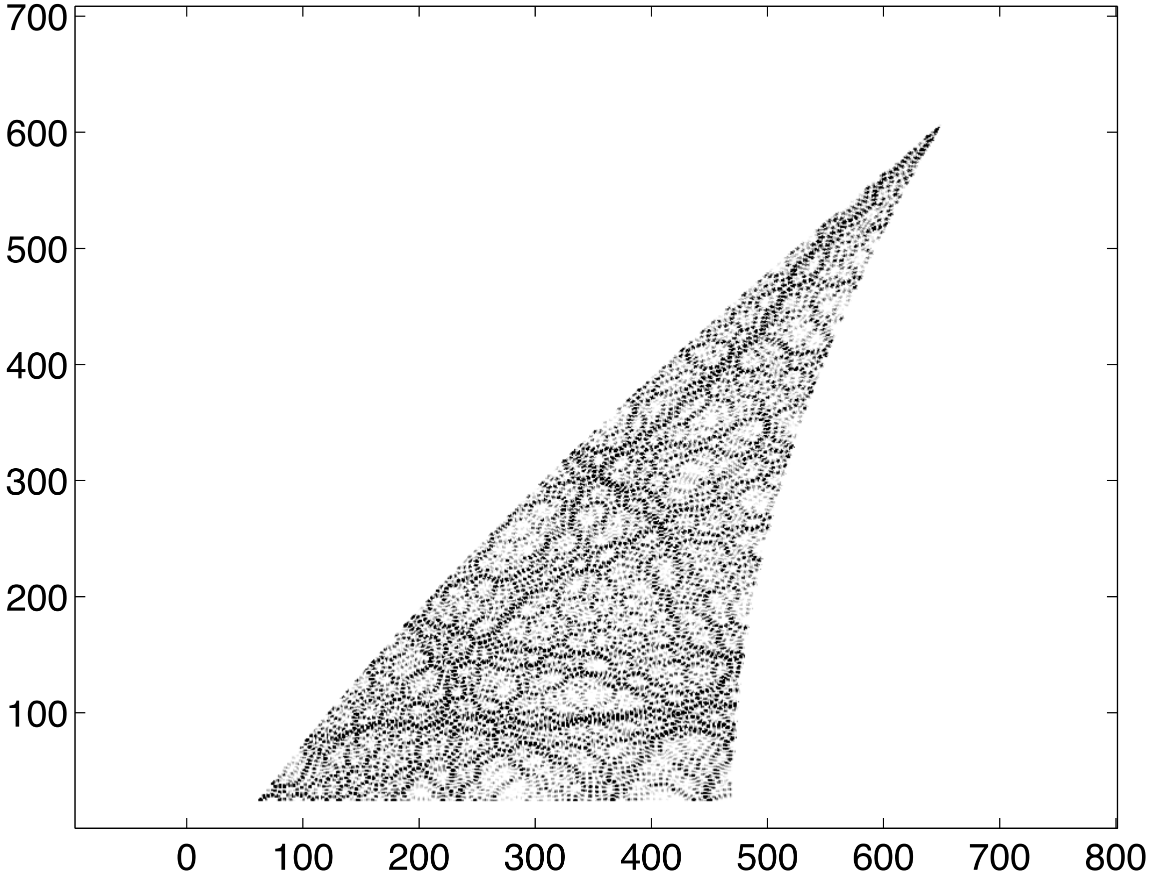

Figure 7.2blarge triangle eigenstate at k=1039.9414

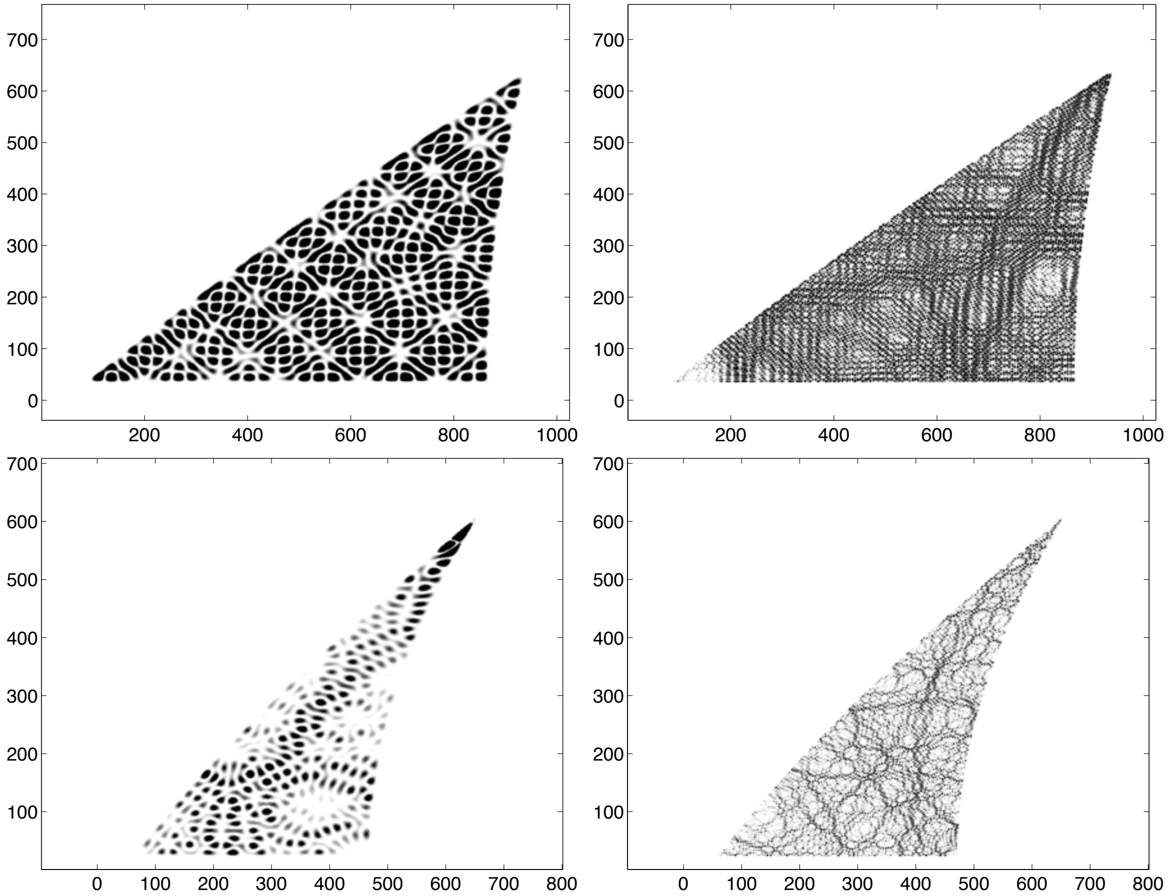

Figure 7.2c eigenstates for: a) small geodesic triangle at $k = 511.6362$ b) small geodesic triangle at $k = 2002.2575$ c) large geodesic triangle at $k = 251.1383$ d) large geodesic triangle at $k = 1000.0533$

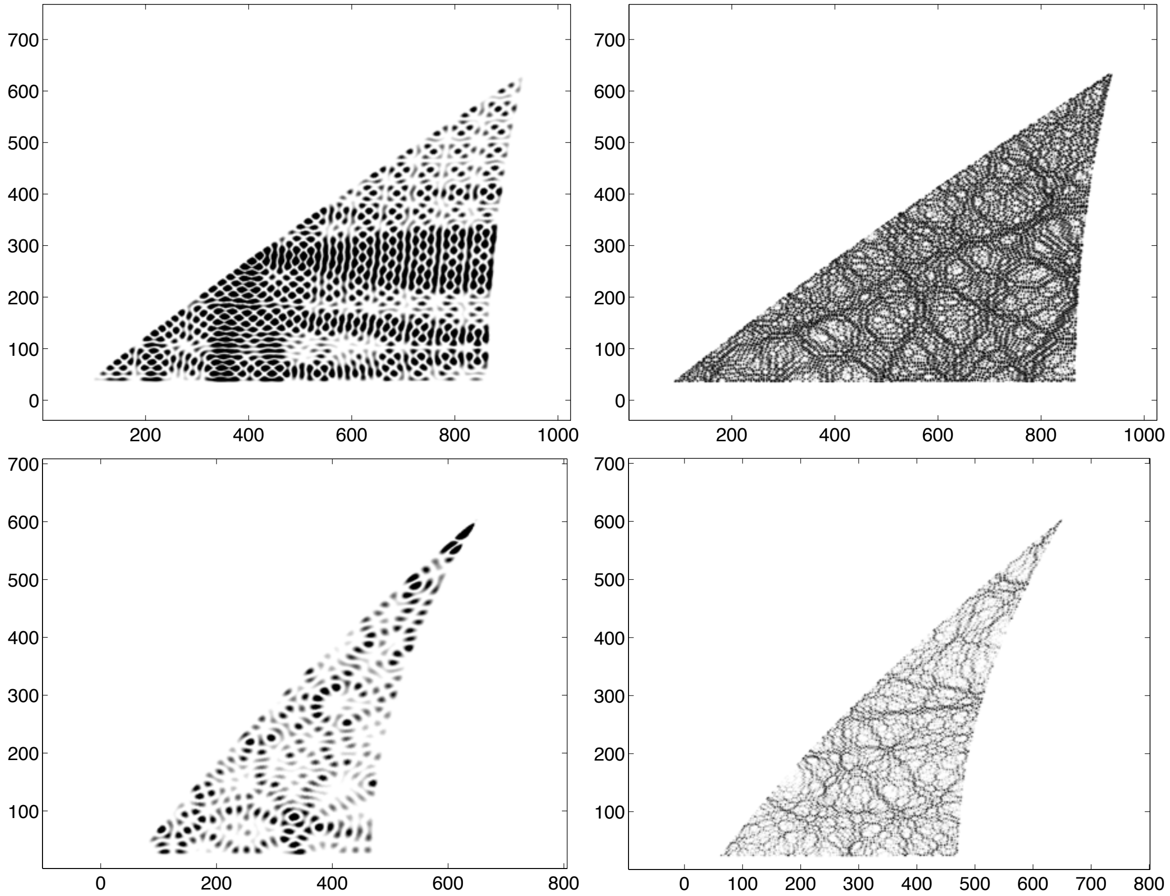

Figure 7.2d eigenstates for: a) small geodesic triangle at $k = 686.7783$ b) small geodesic triangle at $k = 2000.3103$ c) large geodesic triangle at $k = 250.3466$ d) large geodesic triangle at $k = 1006.2305$

7.5.1 curvature induced focusing

Boundary induced focusing should exist for some billiards, since some boundaries must make the dynamics less chaotic, as the example of the annulus shows. We have found a case of a billiard that displays this behavior, in which the focusing increases with the size of the billiard. This is a completely unexpected result, but can be seen as a focusing effect from the non-geodesic sides. In Figure 7.3 we see that a quasi-integrable region comes into existence as the size of the billiard is increased from $\tau_2 = 0.9$ to 1.3. The larger the triangle, the more focusing there is.

The corresponding Poincare sections are given in Figure 7.4. The quasi-integrable behavior results from the curvature of the longer side of the triangle, which on the right side reflects trajectories to the left and on the left side reflects to the right. A geodesic boundary would not have this property. Figure 7.5 shows an eigenstate of this system which clearly shows the effect of the focusing on the eigenstates.

From Figure 7.6, we see that the Lyapunov exponent increases with τ. The large Lyapunov exponent is once again explained by the time spent on the orbit. Nevertheless, the integrable region is large.

For all the geodesic triangles, the surfaces of section is chaotic, as expected. The walls are not focusing at all, since they are merely 'straight lines'.

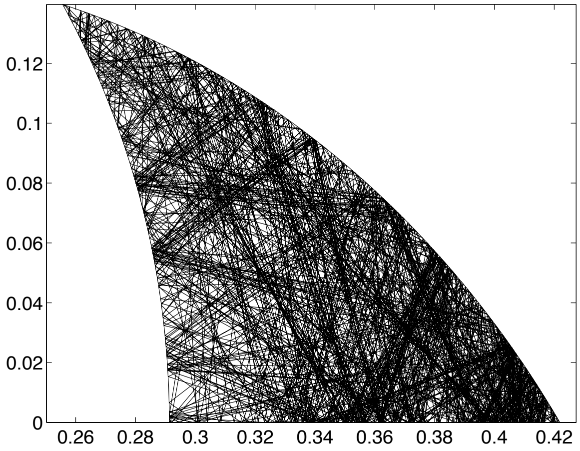

Figure 7.3a trajectory at $p = .1, q = \sinh(\tau_1)\phi_{max} + (\tau_2 - \tau_1)/5$ for the generic triangular shape with $\tau_1 = 0.6$, $\tau_2 = 0.9$ and $\phi_{max} = (\tau_2 - \tau_1)/\tau_1$

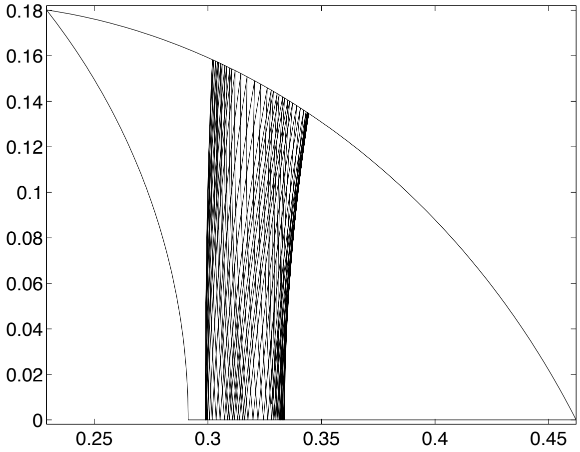

Figure 7.3b Same as Figure 7.3a with $\tau_2 = 1.0$

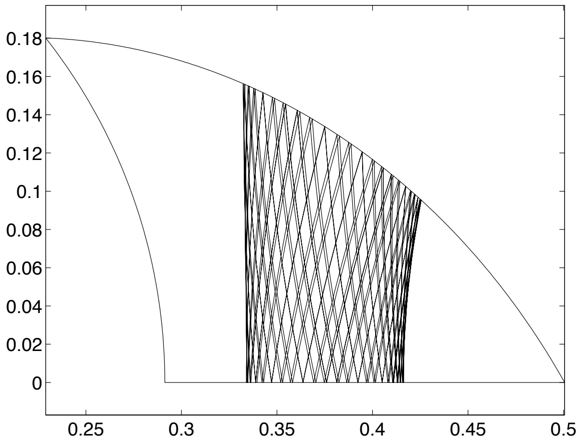

Figure 7.3c Same as Figure 7.3a with $\tau_2 = 1.1$

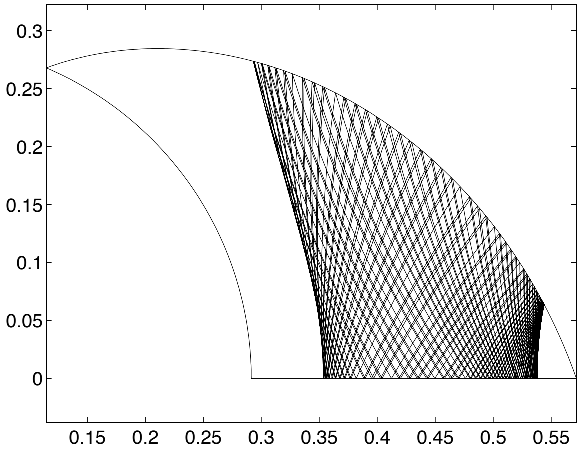

Figure 7.3d Same as Figure 7.3a with $\tau_2 = 1.3$

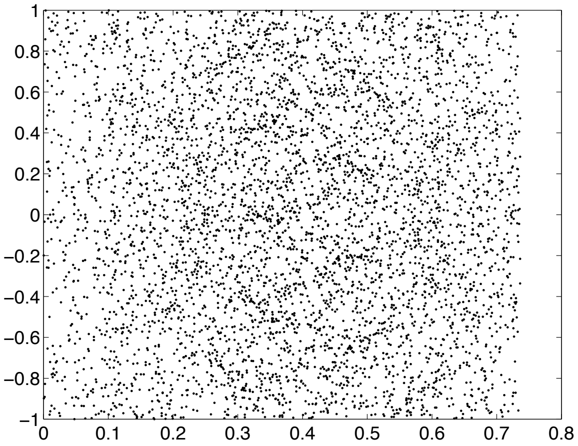

Figure 7.4a Surface of section for the generic triangular shape with $\tau_1 = 0.6$, $\tau_2 = 0.9$ and $\phi_{max} = (\tau_2 - \tau_1)/\tau_1$

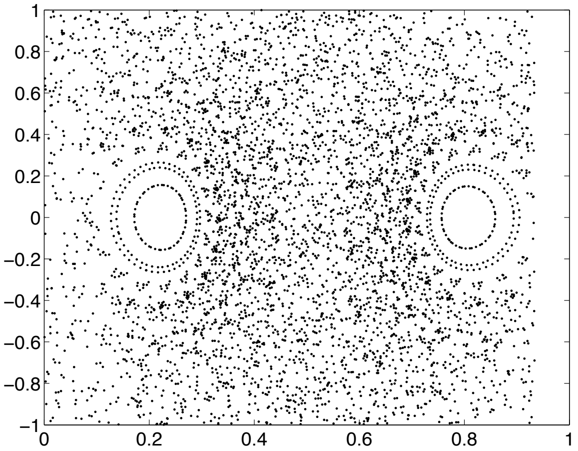

Figure 7.4b Same as Figure 7.4a with $\tau_2 = 1.0$

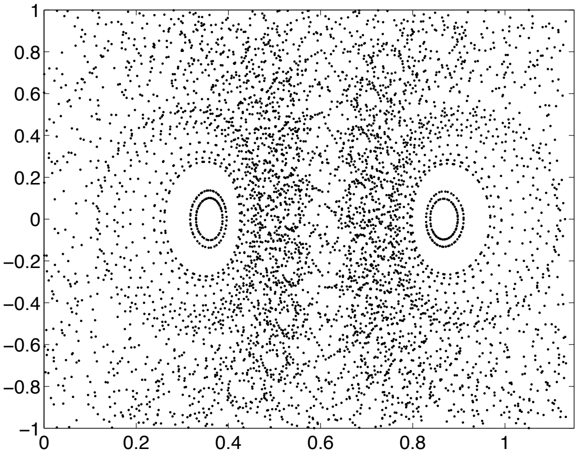

Figure 7.4c Same as Figure 7.4a with $\tau_2 = 1.1$

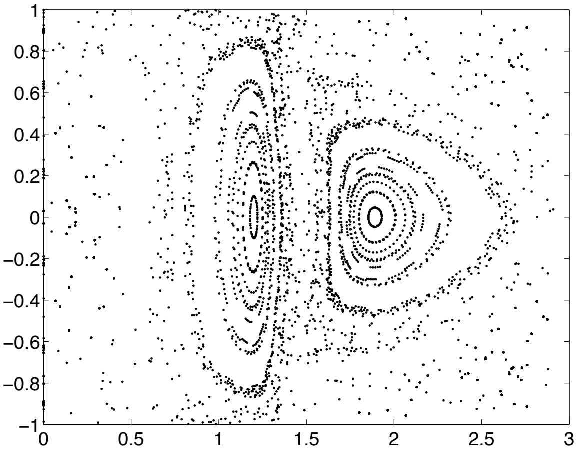

Figure 7.4d Same as Figure 7.4a with $\tau_2 = 1.3$

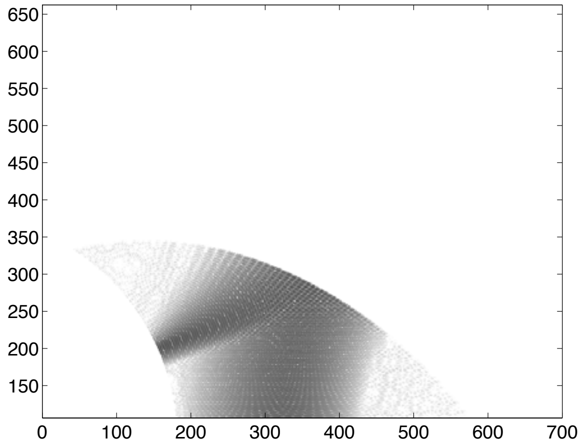

Figure 7.5 Eigenstate at $k = 519.53$ of the non-geodesic triangle with $tau_2 = 1.2$

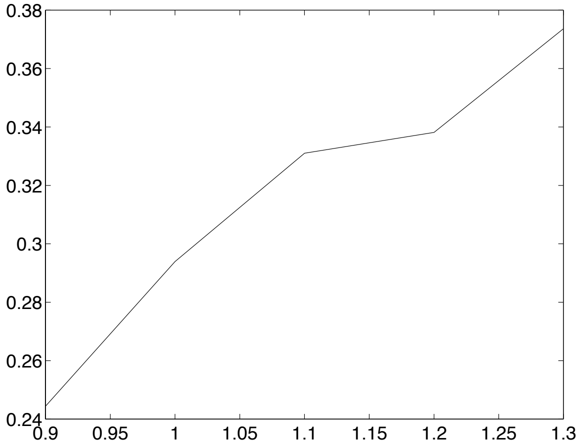

Figure 7.6 Lyapunov exponent as a function of τ_2 for the non-geodesic triangle with $\tau_1 = 0.6$, $\tau_2 = 0.9$ and $\phi_{max} = (\tau_2 - \tau_1)/\tau_1$

7.6 Wavefunction intensity statistics

We compute the wavefunctions intensities in coordinate space as a function of the size of the billiard, to determine the effects of curvature. In Figures 7.7 and 7.8, we plot the probability distribution of the square of the wavefunction. We use an ensemble obtained by taking each eigenfunction in the range considered and evaluating its square on a grid of size equal to the wavelength. As pointed out by Kaplan and Heller, scarred wavefunctions should have more low intensities (antiscars) and high intensities (scars) than predicted by RMT. The RMT probability distribution is given by a Porter-Thomas distribution, while the probability distribution in the presence of scarring is given by a Porter-Thomas distribution modulated by the spectral envelope of the local density of state. As can be seen from Figures 7.7 and 7.8, there are a few more high intensities for the small geodesic triangle. For instance, the probability for finding wavefunction intensities greater than $10^{1.3}$ was 1.27×10^{-5} for the small geodesic triangle, 1.01×10^{-5} for the large geodesic triangle and 0.835×10^{-5} in RMT. For the larger triangle, the enhancement is less than for the smaller triangle. This behavior is expected. The Lyapunov exponent is larger for the larger triangle, and the scarring effect is smaller for larger Lyapunov exponent. The difference between large and small geodesic triangles is small, however. As we will discuss below, the quasi-integrable regions, if present, are too small to significantly affect the wavefunction intensity statistics.

As we see, the presumed scarring effect in the wavefunction intensity statistics is almost too small to be observed. The inner product $|\langle \mathbf{x}, \mathbf{p} | \psi_n \rangle|^2$ of the eigenfunction ψ_n with a coherent state at position $\mathbf{x}$ and momentum $\mathbf{p}$ supplies a much more

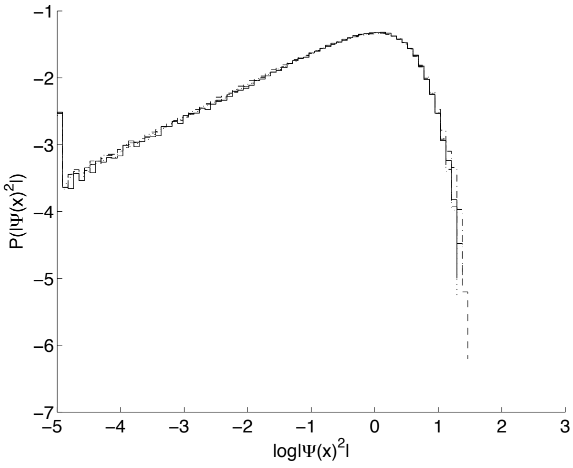

Figure 7.7 Intensity distributions of the eigenstates in coordinate space for the geodesic triangles. The full line is the intensity for RMT, the dashed line that for the stadium billiard, dash-dotted line for the small geodesic triangle and the dotted line for the large geodesic triangle.

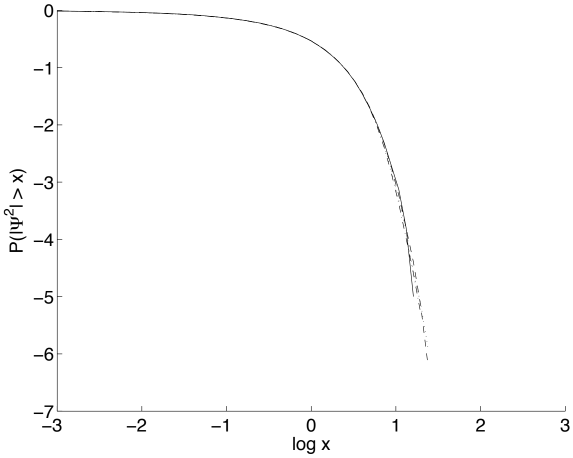

Figure 7.8 Tails of the intensities for the geodesic triangles. The full line is the intensity for RMT, the dashed line that for the stadium billiard, dash-dotted line for the small geodesic triangle and the dotted line for the large geodesic triangle

sensitive measure of the presence of scarring, because scars are localized in phase space. The wavefunction intensity $|\psi_n(\mathbf{x})|^2$ by itself fails to take advantage of the localization in momentum of the scar. In Section 7 below we return to the question of scarring on our billiards using the coherent-state measures.

7.7 The inverse participation ratio (IPR)

The IPR gives an indication of the amount of localization in each state. The IPR is defined by

$$I_n = \frac{(1/J)\sum_{j=1}^{J} |\langle q_j, p_j|n\rangle|^4}{\left[(1/J)\sum_{j=1}^{J} |\langle q_j, p_j|n\rangle|^2\right]^2} \tag{7.14}$$

where n labels the state and j runs over a grid covering phase space. If the intensities $|\langle q_j, p_j|n\rangle|^2$ are uniformly distributed the IPR gives 1; if, in the case of strong localization, one of them dominates the rest, which can be approximated by zero, the IPR becomes J. Thus, an IPR lying between these extremes indicates the amount of localization. The RMT prediction for the IPR is 2 for complex wavefunctions and 3 for real ones. The IPR of eigenstates of the stadium billiard was studied by Bies *el al.* [12], where most of the excess IPR over 2 was attributed to symmetry effects.

We obtain average IPRs of 6.13 and 2.21 for the small geodesic triangle in the range $k = 500-700$ and $k = 2000-2080$, respectively. For the large geodesic triangle, we find 2.77 in the $k = 250 - 350$ range, and 2.24 in for $k = 1000 - 1040$.

The IPRs for the ranges considered are shown in Figure 7.9. The low k IPR are very large compared to RMT, while the larger k's have much smaller IPRs, though they are still larger than the RMT prediction. This indicates that some k dependent source of localization is at work. The magnitude of the increased IPR for the higher IPR states is large enough that it suggests that it is not attributable to scarring (similar enhancements are seen in the flat-space stadium for bouncing ball states).

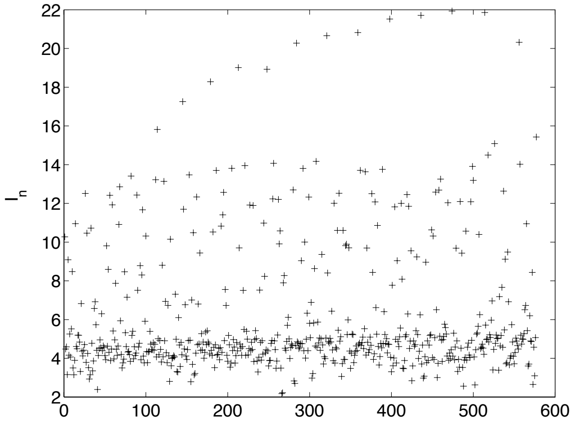

Figure 7.9a IPR for states between $k = 500$ and $k = 700$ of the small geodesic triangle. Here $n$labels the state and n_{500} is the level number at $k = 500$

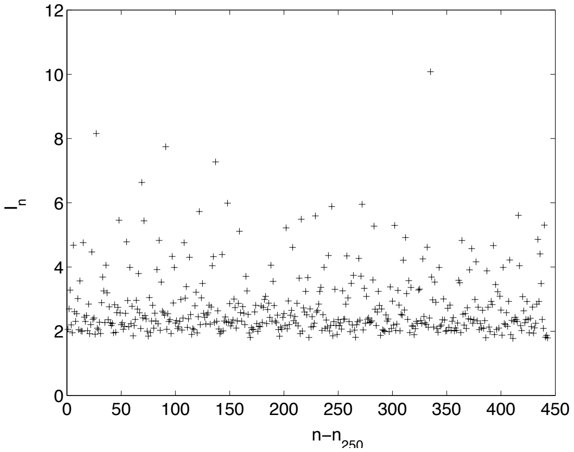

Figure 7.9b Same as Figure 7.9a for $250 < k < 350$ for the large geodesic triangle

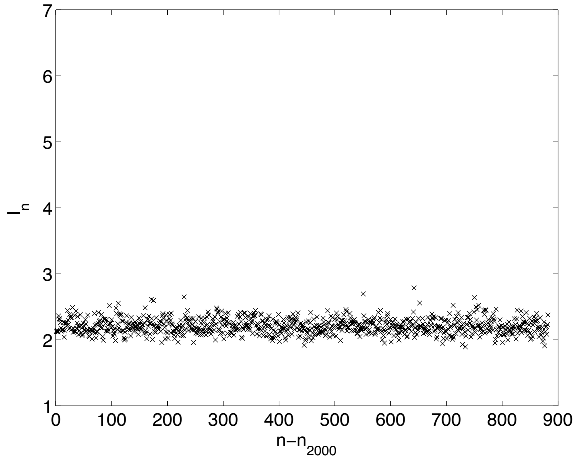

Figure 7.9c IPR for states between $k = 2000$ and $k = 2080$ of the small geodesic triangle. Here $n$labels the state and n_{2000} is the level number at $k = 2000$

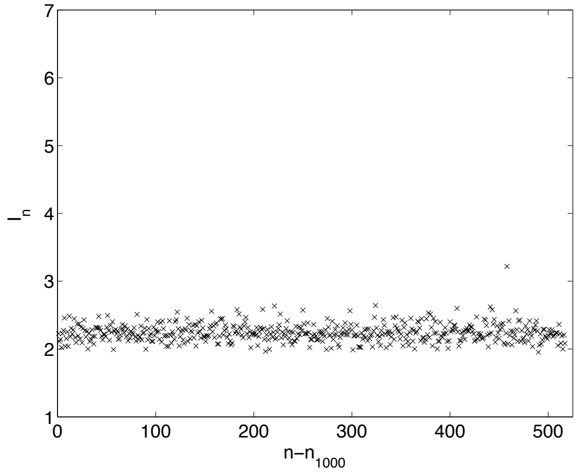

Figure 7.9d Same as Figure 7.9c at $1000 < k < 1040$ for the large geodesic triangle

7.8 The local inverse participation ratio

The IPR gives an indication of the aggregate localization properties of individual states. Since, however, scarring is a statistical effect of many eigenstates, one may ask whether there is another measure involving the whole sequence of eigenstates that is sensitive to the presence of scarring. The local IPR (LIPR) supplies such a measure [12].

The LIPR is defined by

$$L(q,p) = \frac{(1/N)\sum_{n=1}^{N} |\langle q,p|n\rangle|^4}{\left[(1/N)\sum_{n=1}^{N} |\langle q,p|n\rangle|^2\right]^2} \tag{7.15}$$

It shows the localization at a particular point in phase space. Clearly, the spectral envelope due to short-time dynamics in the presence of scarring is an example of localization which occurs at a particular point in phase space, namely, that associated with the coordinates of the periodic orbit. Accordingly, we expect an enhancement of LIPR near short periodic orbits.

7.8.1 Low energies

We have indentified using a root search all the short periodic orbits up to length 10 for the geodesic triangle with $\tau_2 = 0.9$. The bright points in Figure 7.8a, however, do not correspond to these short periodic orbits. Instead, they appear to be related to trajectories that spend time in the corners. The corresponding localization of the quantum eigenstates is $\hbar$ dependent, since the bright points do not persist at higher energies (see next section). Thus, they cannot be due to the short-time classical dynamical effects such as scarring. This statement will be confirmed below with a

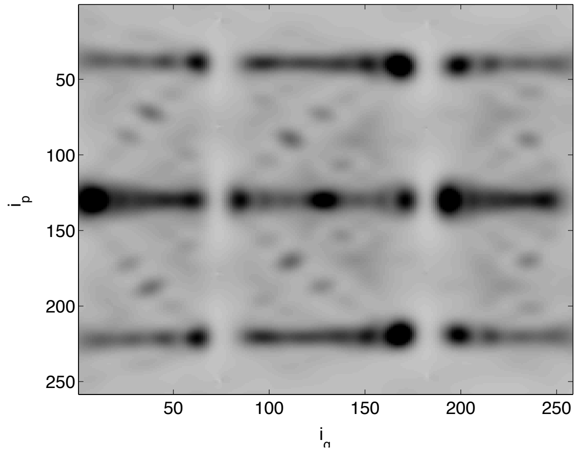

Figure 7.10a LIPR for the small geodesic triangle at $k = 500 - 700$. i_q and i_p label the points on the q and p grids, respectively.

classical simulation in section 7c.

We select states that have large intensities which result in high LIPRs. An example of such a state is shown in Figure 7.11 The density is much higher at the corners. The classical trajectories spend more time in the corner region. Whenever the trajectory returns very close to its starting point after one bounce, the overlap will be large due to the small Lyapunov exponent of the orbit. It is possible that that corresponds to a periodic orbit that has many short steps in the corner region. We have not identified any such orbits in our search so far (up to 12 bounces).

7.8.2 High energies

The LIPR plots are given in in Figure 7.12. The main feature of these LIPR plots is a background of 2 and dark spots of intensity 3 isolated at p = 0. As found by Bies *et al.*, the line at p=0 can be explained by a symmetry effect. The line at $p = 0$ is invariant under time-reversal symmetry, so that the LIPR should display a

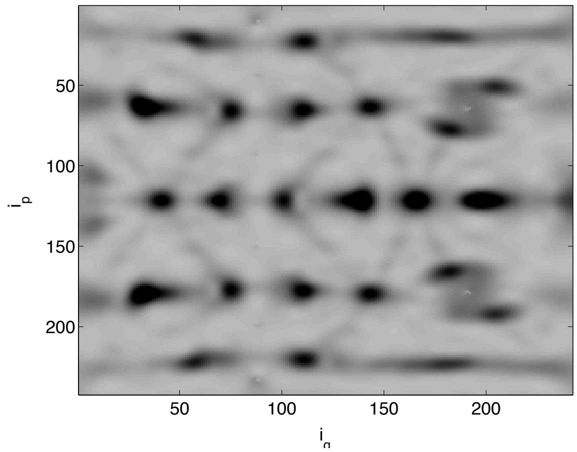

Figure 7.10b LIPR for the large geodesic triangle at $k = 250 - 350$

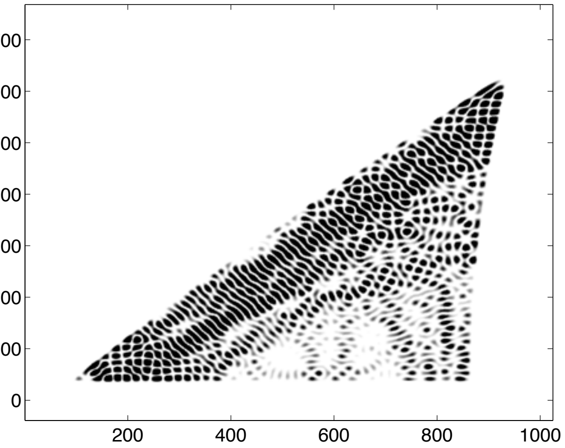

Figure 7.11 Eigenstate of the small geodesic triangle at $k = 684.9212$

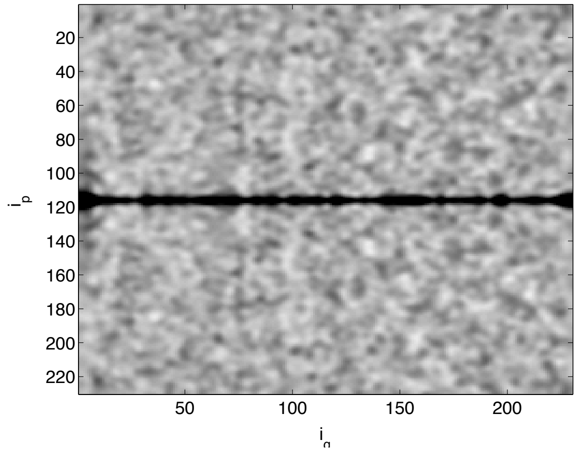

Figure 7.12a LIPR for the small geodesic triangle for $k = 2000 - 2080$. i_q and i_p label the points on the q and p grids, respectively.

symmetry enhancement from 2 to 3. Surprisingly, the enhancement we find is a factor of 2 instead of 3/2. This discrepancy remains unexplained. We also notice vertical lines for the LIPR of the large triangles. These lines remain unexplained, as they are not associated with any corners.

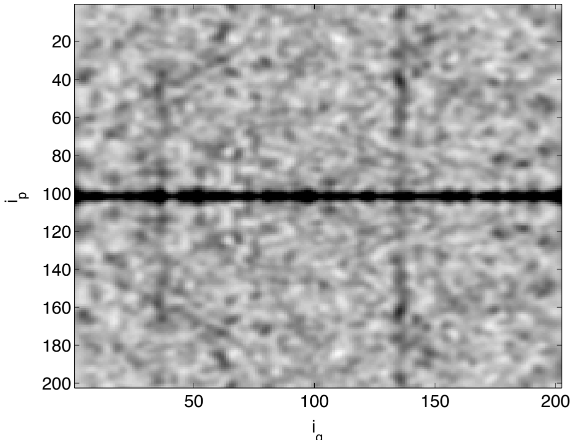

Figure 7.12b Same as Figure 7.12a for the geodesic triangle for $k = 1000 - 1039$

7.9 Coherent-state measures of localization

We compute the overlaps of the wavefunction with two-dimensional Gaussians centered on a grid of points inside the billiard. The grid spacing is taken to be $1/\sqrt{k}$. The spatial width is $\sigma = 1/\sqrt{k}$. The width in momentum of the wavepacket accordingly is $\sqrt{k}$. The momentum $\mathbf{k}$ of the centroid of the wavepacket lies on the circle $|\mathbf{k}| = k$. Its angle θ is uniformly distributed on the circle in increments of $\Delta\theta = 2\pi k/\sqrt{k} = 2\pi\sqrt{k}$ so that the wavepackets are independent but closely spaced.

7.9.1 Intensity statistics

The distribution of intensities for this ensemble of wavepackets is shown in Figure 7.13a for the eigenstates of the small geodesic triangle and in Figure 7.13b for those in the large geodesic triangle. Both Figure 7.13a and b display a large excess of large and small intensities relative to RMT. This must be taken as an indication of a significant dynamically induced localization phenomenon. If this localization is due to scarring, the enhancement should be greater than the statistically expected distribution. For comparison, we computed the intensities for RMT subject to the envelope arising from the decay of the autocorrelation function at very short times $\Delta t = 1/mk^{3/2}$ when the Gaussians separate. We call this the corrected RMT. As expected, the distribution of these intensities in the corrected RMT model should have more large and small distributions than in uncorrected RMT; Figures 7.13a and b confirm this. However, the distribution of intensities for the eigenstates has even more large and small values than does that of the corrected RMT model.

It has not yet been shown that the mechanism producing this excess localization

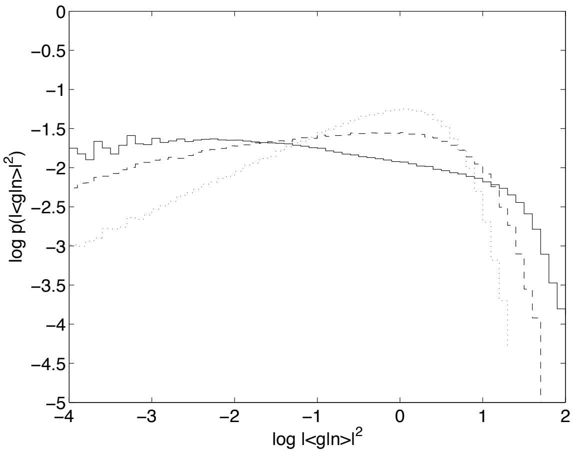

Figure 7.13a Distribution of intensities for the overlap of coherent states with eigenstates of the small geodesic triangle, solid line; RMT, dotted line; and corrected RMT, dashed line.

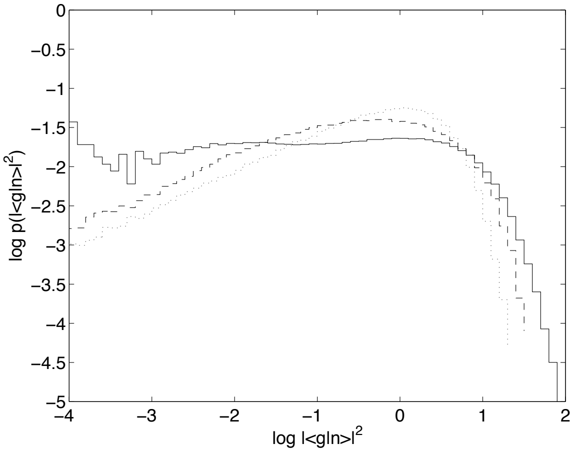

Figure 7.13b Distribution of intensities for the overlap of coherent states with eigenstates of the large geodesic triangle, solid line; with RMT, dotted line; and corrected RMT, dashed line.

is scarring. The curvature dependence of the excess localization is consistent with the hypothesis that it is caused by scarring. The excess localization is substantially greater for the smaller triangle, which has the smaller Lyapunov exponent. Since the scarring effect has a strength that scales as $1/\lambda$, we expect that it would be less important in the larger triangle. Quasi-integrable motion can be ruled out as a cause because the Poincaré sections of both triangles are fully chaotic.

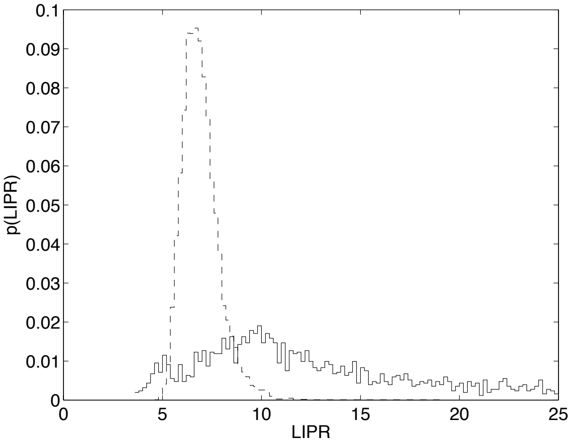

Figure 7.14a Distribution of LIPR of the intensities for the overlap of coherent states with eigenstates of the small geodesic triangle at $k = 500 - 700$, solid line; corrected RMT, dashed line.

7.9.2 LIPR

The hypothesis that scarring is the cause of the excess localization can be further tested using the LIPR. The modulated spectral envelope of scar theory implies an enhanced LIPR relative to RMT. In Figure 7.14, we give the distribution of LIPRs for the small and large geodesic triangles for this ensemble of coherent states. In agreement with the results in the previous subsection, the distribution of both triangles has a noticeable tail at LIPRs larger than 2 (the RMT average). Note that on this scale the distribution of RMT LIPRs is quite narrow. Also, the tail is smaller for the larger geodesic triangle. Thus, we have shown that the localization phenomenon in question exists not only in phase space, but also in the local density of states for typical coherent states.

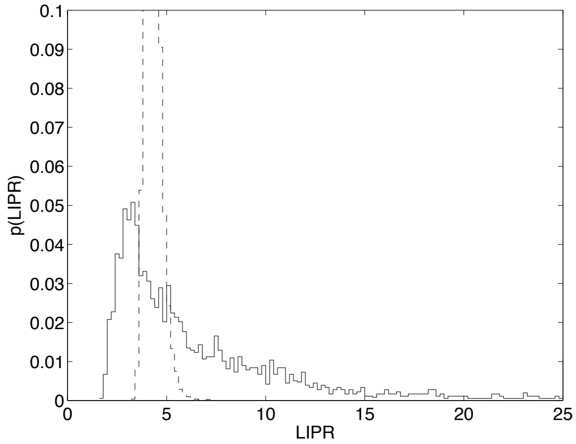

Figure 7.14b Distribution of LIPR of the intensities for the overlap of coherent states with eigenstates of the large geodesic triangle at $k = 250 - 350$, solid line; corrected RMT, dashed line.

7.9.3 Classical overlaps

We ask whether scarring can explain the localization in excess of corrected RMT seen in Figure 7.14. The prevalence of scarring can be estimated by the fraction of phase space covered by the short periodic orbits. Any trajectory within a distance $\sqrt{\hbar} = 1/\sqrt{k}$ of a short periodic orbit will have at least one short-time recurrence at the period of the orbit. Hence, modulation of the local density of states at $k = 500$, the short periodic orbits (including their multiplicities) cover about 18% of the phase space in Birkhoff coordinates. Thus, if scarring is the principle mechanism of localization, we can presume that the largest 18% of the LIPRs in Figure 7.14 are due to scarring. This would mean in Figure 7.14a that all IPRs below 26.8 cannot be accounted for by scarring and in Figure 7.14b that all IPRs below 9.5. Hence, this rough estimate shows that scarring cannot be the only effect producing the localization, especially in the small geodesic triangle.

A more precise estimate can be had from the classical overlaps as follows: in [12], it was found that

$$LIPR = F\ IPR_{short-time}(1 + 2\sum_{t=1}^{\infty}(O_t - 1/N)) \qquad (7.16)$$

where F is 2 or 3 depending on whether the wavepacket sits on the symmetry line and $IPR_{short-time}$ is the enhancement of IPRs in corrected RMT due to the short-time envelope and O_t is the classical overlap of a wavepacket with itself once evolved by a time t (normalized such that $O_0 = 1$). The factor of $1/N$ is the overlap of the initial wavepacket at time 0 with the wavepacket after it has been evolved for a time t greater than the mixing time. Here $IPR_{short-time} = 3.4$ on average for the envelope extending from $k = 500$ to $k = 700$ (the distribution of $IPR_{short-time}$ is shown in

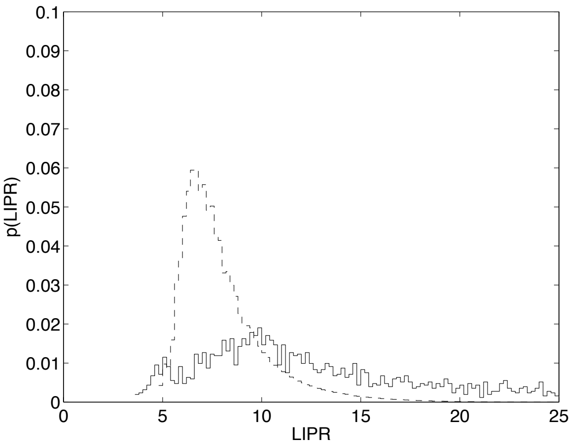

Figure 7.15a Distribution of LIPR for the classical simulation for the small geodesic triangle, dashed line; the intensities for the overlap of coherent states with eigenstates of the small geodesic triangle, solid line.

Figure 7.14a. It can also be shown that $1/N = 1/Lk$, where $L = 0.867$ is the length of the perimeter of the small geodesic triangle. The overlaps were computed for an ensemble of 10000 random initial conditions up to a time $t = 10$. Large recurrences were found for initial conditions starting near one of the short periodic orbits. The distributions of LIPR obtained in this classical simulation is plotted in Figure 7.15. It is evident that the classical overlaps due to short-time dynamics account for some but not all of the localization in Figure 7.15 (the spread of $IPR_{short-time}$ in Figure 7.14a is not sufficient to account for the discrepancy). The high-LIPR tail must be due to purely quantum localization effects such as diffraction at the corners. The high-LIPR tail is more prominent in the small geodesic triangle. Thus, the scarring picture comes closer to explaining all the localization in the large geodesic triangle (Figure 7.15b). This is to be expected since the large geodesic triangle is not near integrable.

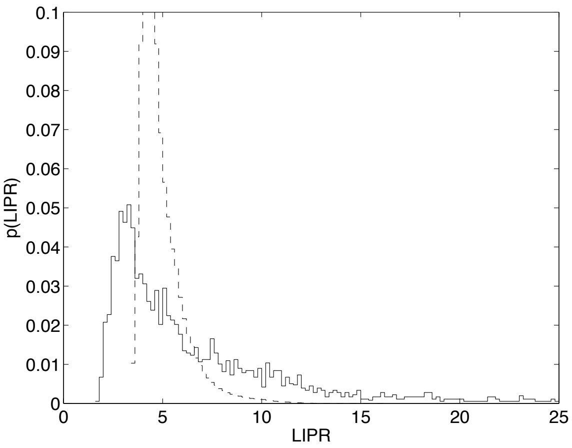

Figure 7.15b Distribution of LIPR for the classical simulation for the large geodesic triangle, dashed line; the intensities for the overlap of coherent states with eigenstates of the large geodesic triangle, solid line.

7.10 Scarring?

We have argued that part of the excess localization is due to scarring. The indication of this would be a periodic modulation of the local density of states for coherent states lying on short periodic orbits. In order to test this, we found a periodic orbit of period 4 in the small geodesic triangle starting at $\tau = 0.8103$ on the lower edge of the triangle, with initial momentum pointing perpendicularly inward. The IPR of its local density of states was 5.75, which is larger than the RMT value of 3. The local density of states plotted in Figure 7.16 does display the periodic modulation expected. The arclength of this orbit is $\Delta s = 0.51$, hence its period is $T = \Delta s/(k/m)$ and the period of the modulations should be $\Delta E = 2\pi/T = (2\pi k/m)/\Delta s$, or $\Delta k = \Delta E/(k/m) = 2\pi/\Delta s = 12.3$. Hence, in the range $k = 500$ to $k = 700$, there should be about 16 oscillations. In Figure 7.17, we display the envelope of the LDOS smoothed over $\sigma = \Delta k/5$. The expected oscillations are clearly present. However, the envelope does not agree well with that predicted by scar theory. The reason for this is that many of the states have quasi-integrable character, and do not follow the envelope predicted by scar theory (although evidently enough states follow the scar envelope for the signal of a periodic modulation to be present at the level we find in Figure 7.17). As a result, the autocorrelation function obtained by Fourier transforming the LDOS has only one short-time recurrence at time T. Apparently non-linear recurrences interfere with the higher-order recurrences. In order to obtain an autocorrelation function in agreement with scar theory (semi-classical limit), we would have to go to much larger k so that $1/\sqrt{k}$ would be small compared to the size of the linearizable region around the short periodic orbit. Nevertheless, the modulations in the smooth LDOS confirm the presence of scarring, understood as a statistical effect, not necessarily as something visible in coordinate space, as we discussed in the introduction. The LDOS for a Gaussian wavepacket at an arbitrary point in the interior does not display these periodic modulations.

The scarring picture can be verified by constructing a corrected model of RMT. Let us call the RMT modulated by the very short-time envelope RMT 1. However, we know that the spectral envelope in the presence of scarring contains further oscillations which for large Lyapunov exponents are approximately $1 + 2e^{-\lambda T}\cos(ET)$. We call the RMT modulated by this envelope RMT 2. Due to the cosine factor, RMT 2 should have more large and small intensities than RMT 1. In fact, according to scar theory, the actual distribution of intensities in the LDOS should agree with RMT 2. In Figure 7.18, we show this distribution for the periodic orbit described in the previous paragraph and compare it with RMT 1 and RMT 2. As we see, the agreement is satisfactory. To distinguish RMT 1 and RMT 2 would require better statistics, i.e. going farther into the semiclassical limit.

7.11 Conclusion

We looked at the curvature contribution to localization on the pseudosphere, and discuss the long standing problem of the presence of scars. We found indeed that eigenstates of billiards on the pseudosphere have dramatic localization properties when measured by coherent states, far in excess of what would be predicted on the basis of RMT or by the scarlet phenomenon. The surface curvature plays the role of a parameter controlling the strength of this localization through the global Lyapunov

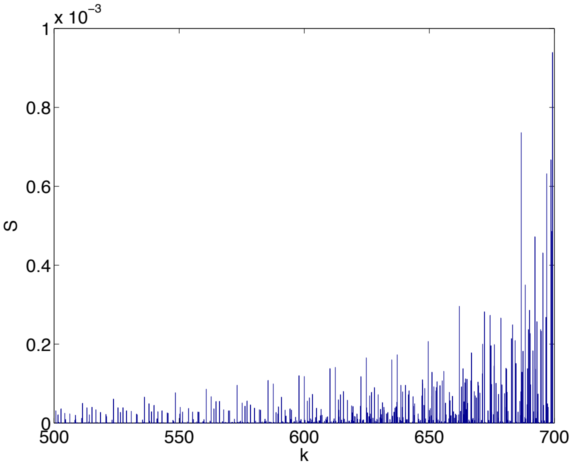

Figure 7.16 Local density of states for a coherent state on the short periodic orbit starting at $\tau = 0.8103$ with initial momentum normal to the boundary of the small geodesic triangle.

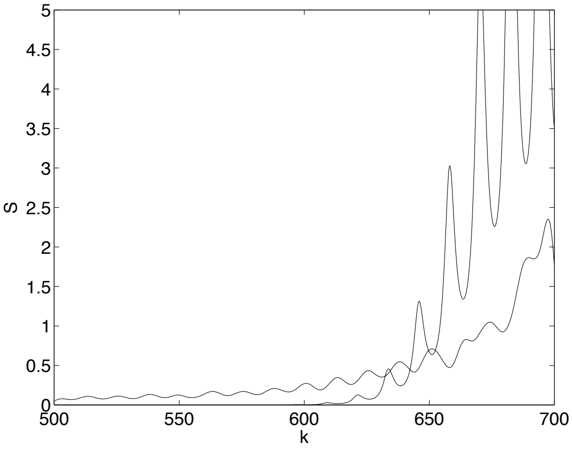

Figure 7.17 Smoothed local density of states for a coherent state on the short periodic orbit starting at $\tau = 0.8103$ with initial momentum normal to the boundary of the small geodesic triangle.

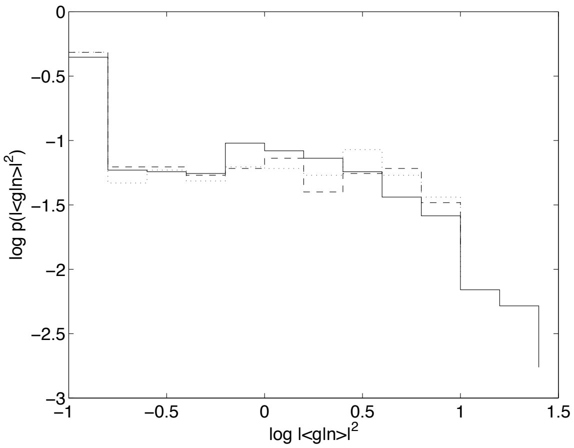

Figure 7.18 Distribution of intensities for the short periodic orbit starting at $\tau = 0.8103$ and its initial momentum normal to the boundary of the small geodesic triangle; numerical results, solid line; RMT 1, dotted line; RMT 2, dashed line.

exponent. The divergence of nearby trajectories due to the negative curvature merely increases the Lyapunov exponent along any periodic orbit. The curvature dependence of this localization suggests that scarring is at its root. The periodic modulation of the LDOS confirms that scarring is present. The Lyapunov exponents of the short periodic orbits in the small geodesic triangle range from 1 to 3 whereas the modulation of the LDOS disappears only when the Lyapunov exponents exceeds 2π. However, we conclude that much of the excess localization is due to hard quantum effects beyond classical short-time dynamics. In addition to this localization effect in fully chaotic billiards, we find that some billiards develop curvature-dependent quasi-integrable motion due to the interaction of curved boundary and surface curvature, a counterintuitive result.

7.12 Appendix A: The pseudosphere equations

In this section, we give a brief review of the pseudosphere equations which are used for this paper. A more detailed review of the properties of surfaces of constant negative curvature can be found in [4]. In Cartesian coordinates, the defining equation of the surface of the pseudosphere is given by

$$X^2 + Y^2 - Z^2 = -R^2. \tag{7.17}$$

We may fix R to be 1 without loss of generality. This equation can be rewritten in 'polar' (Minkowsky) coordinates (τ, ϕ), such that

$$X = \sinh\tau\cos\phi \tag{7.18}$$

$$Y = \sinh\tau\sin\phi \tag{7.19}$$

$$Z = \cosh\tau \tag{7.20}$$

In these coordinates, the metric on the pseudosphere is

$$ds^2 = d\tau^2 + \sinh^2\tau d\phi^2 \tag{7.21}$$

On the sphere, the geodesics are given by $\vec{n_s} \cdot \vec{r} = 0$, where $\vec{n_s}$ is the normal to the plane of the great circle, and $\vec{r}$ a point along it. Similarly, the geodesics on the pseudosphere are given by the intersection of planes through the origin of normal $\vec{n}$ with the surface. Thus, the geodesic equation for a given $\vec{n}$ is of the form:

$$0 = n_x \sinh\tau\cos\phi + n_y \sinh\tau\sin\phi + n_z\cosh\tau \tag{7.22}$$

The Poincare disk forms another convenient representation of surfaces of constant negative curvature. The later is obtained from the Minkovsky coordinates by the transformation

$$r = \tanh(\tau/2) \tag{7.23}$$

In these coordinates, the points at infinity on the pseudosphere are mapped onto points at the boundary of the disk. In this case, the geodesics are lines starting and ending on the boundary of the disk, i.e. from one point at '∞' to another. The metric in these coordinates is readily found to be

$$ds^2 = dr^2 + r d\phi^2. \tag{7.24}$$

Bibliography

[1] R. Aurich and F. Steiner. *Physica D*, **48**:445, 1991.

[2] R. Aurich and F. Steiner. *Physica D*, **64**:185, 1993.

[3] R. Aurich and F. Steiner. *Chaos, Solitions and Fractals*, **64**:185, 1995.

[4] N. L. Balazs and A. Voros. *Phys. Rep.*, **64**, 1986.

[5] A. H. Barnett. *Dissipation in deforming chaotic billiards.* PhD thesis, Harvard University, 2000.

[6] M. V. Berry. In G. Iooss, R. Helleman, and R. Stora, editors, *Chaotic Behavior of Deterministic Systems.* North-Holland, 1983.

[7] M. V. Berry. *J. Phys. A*, **27**:L391, 1994.

[8] M. V. Berry. *J. Phys. A*, **35**:3025, 2002.

[9] M. V. Berry and M. Tabor. *Proc. R. Soc. Lond.*, **356**:L375, 1977.

[10] M. V. Berry and M. Wilkinson. *Proc. R. Soc. Lond.*, **392**:15, 1984.

[11] W. E. Bies and E. J. Heller. *J. Phys. A*, **35**:5673, 2002.

[12] W. E. Bies, L. Kaplan, M. R. Haggerty, and E. J. Heller. *Physica D*, **64**:185, 1993.

[13] P. A. Boasman. *Nonlinearity*, **7**:485, 1994.

[14] M. G. E. da Luz A. Lupu Sax and E. J. Heller. *Phys. Rev. E*, **56**:2496, 1997.

[15] S. Datta. *Electronic Transport in Mesoscopic Systems.* Cambridge University Press, 1997.

[16] Y. Colin de Verdiere. *Commun. Math. Phys.*, **102**:497, 1985.

[17] B. Dietz and U. Smilansky. *Chaos*, **3**:581, 1993.

[18] J. P. Eckmann and C. A. Pillet. *Commum. Math. Phys.*, **170**:283, 1995.

[19] B. Dietz *et al.* *Phys. Rev. E*, **51**:4222, 1995.

[20] B. Gutzkin. preprint `nlin.CD/0301031`.

[21] E. J. Heller. *Phys. Rev. Lett.*, **83**:1515, 1984.

[22] E. J. Heller. In M.-J. Giannoni, A. Voros, and J. Zinn-Justin, editors, *Chaos and Quantum Physics*, page 548. North-Holland, 1991.

[23] E. J. Heller and S. Tomsovic. *Physics Today*, **46**:38, 1993.

[24] S. Horticar and M. Schrednicki. *Phys. Rev. Lett.*, **80**:1646, 1998.

[25] L. Kaplan. *Phys. Rev. Lett.*, **80**:2582, 1998.

[26] L. Kaplan and E. J. Heller. *Ann. Phys.*, **264**:171, 1998.

[27] L. Kaplan and E. J. Heller. *Physica D*, **121**:1, 1998.

[28] N. Lepore, D. Cohen, and E. J. Heller. in preparation.

[29] B. Li and M. Robnik. *J. Phys. A*, **27**:5509, 1994.

[30] B. Li, M. Robnik, and B. Hu. *Phys. Rev. E*, **57**:4095, 1998.

[31] G. A. Luna-Acosta, K. Na, and L. E. Reichl. *Phys. Rev. E*, **53**:3271, 1996.

[32] B. Malgrange. *Ann. Inst. Fourier Grenoble*, **6**:271, 1955.

[33] S. W. McDonald. PhD thesis, University of California at Berkeley, 1983. Report No. 14837.

[34] S. W. McDonald and A. N. Kaufman. *Phys. Rev. Lett.*, **42**:1189, 1979.

[35] S. W. McDonald and A. N. Kaufman. *Phys. Rev. A*, **37**:3067, 1988.

[36] P. O'Connor, J. Gehlen, and E. J. Heller. *Phys. Rev. Lett.*, **58**:1296, 1987.

[37] M. Robnik. *J. Phys. A*, **17**:104, 1983.

[38] D. O. Hogenboom S. Sridhar and B. A. Willemsen. *J. Stat. Phys.*, 68:239, 1992.

[39] A. I. Schnirelman. *Usp. Mat. Nauk.*, 29:181, 1974.

[40] C. Scnmit. In M.-J. Giannoni, A. Voros, and J. Zinn-Justin, editors, *Chaos and Quantum Physics*, page 335. North-Holland, 1991. and private communication.

[41] M. E. Spina and M. Saraceno. *J. Phys. A*, 32:7803, 1999.

[42] M. E. Spina and M. Saraceno. *J. Phys. A*, 34:2549, 2001.

[43] S. Sridhar. *Phys. Rev. Lett.*, 67:785, 1991.

[44] S. Sridhar and E. J. Heller. *Phys. Rev. A*, 46:R1728, 1992.

[45] S. Stein and H. J. Stockmann. *Phys. Rev. Lett.*, 68:2867, 1992.

[46] H. J. Stockmann. *Quantum Chaos: An introduction.* Cambridge University, 1999.

[47] M. Tinkham. *Group Theory and Quantum Mechanics.* Mc-Graw Hill, 1964.

[48] E. Vergini. *Estudio Cuántico y Semiclásico de Billares Clásicamente Caóticos.* PhD thesis, Universidad de Buenos Aires, 1995.

[49] E. Vergini and M. Saraceno. *Phys. Rev. E*, **52**:2204, 1995.

[50] J. Wiersig and G. C. Carlo. preprint `nlin.CD/0212011`.

[51] S. Zelditch. *Duke Math. J.*, **55**:919, 1987.